Reconciling Surface Deflections From Simulations of Global Mantle Convection

Conor Patrick O'Malley[1], Gareth G Roberts[1], James Panton[2], Fred D Richards[1], J. Huw Davies[3], Victoria M Fernandes[4], and Sia Ghelichkhan[5]

[1]Imperial College London
[2]School of Earth and Environmental Sciences, Cardiff University
[3]School of Earth and Ocean Sciences, Cardiff University
[4]GFZ Potsdam
[5]Australian National University

November 8, 2023

Abstract

The modern state of the mantle and its evolution over geological timescales is of widespread importance for the Earth sciences. For instance, it is generally agreed that mantle flow is manifest in topographic and drainage network evolution, glacio-eustasy, volcanism, and in the distribution of sediments. An obvious way to test theoretical understanding of mantle convection is to compare model predictions with independent observations. We take a step towards doing so by exploring sensitivities of theoretical surface deflections generated from a systematic exploration of global mantle convection simulations. Sources of uncertainty, model parameters that are crucial for predicting deflections, and those that are less so, are identified. We start by quantifying similarities and discrepancies between deflections generated using numerical and analytical methods that are ostensibly parameterised to be as-similar-as-possible. Numerical approaches have the advantage of high spatial resolution, and can capture effects of lateral viscosity variations. However, treatment of gravity is often simplified due to computational limitations. Analytic solutions, which leverage propagator matrices, are computationally cheap, easy to replicate, and can employ radial gravitation. However, spherical harmonic expansions used to generate solutions can result in coarser resolution, and the methodology cannot account for lateral viscosity variations. We quantify the impact of these factors for predicting surface deflections. We also examine contributions from radial gravity variations, perturbed gravitational potential, excised upper mantle, and temperature-dependent viscosity, to predicted surface deflections. Finally, we quantify effective contributions from the mantle to surface deflections. The results emphasise the sensitivity of surface deflections to the upper mantle.

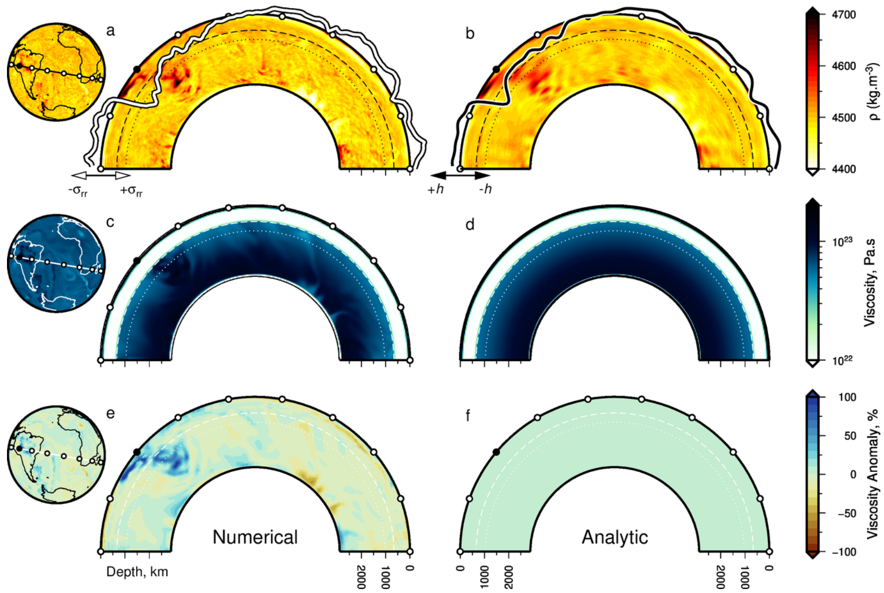
a
b
c
d
e
f
$-\sigma_{rr}$
$+\sigma_{rr}$
$+h$
$-h$
ρ (kg.m^{-3})
4400
4500
4600
4700
Viscosity, Pa.s
10^{22}
10^{23}
Viscosity Anomaly, %
100
50
0
−50
−100
Numerical
Analytic
Depth, km
0
1000
2000

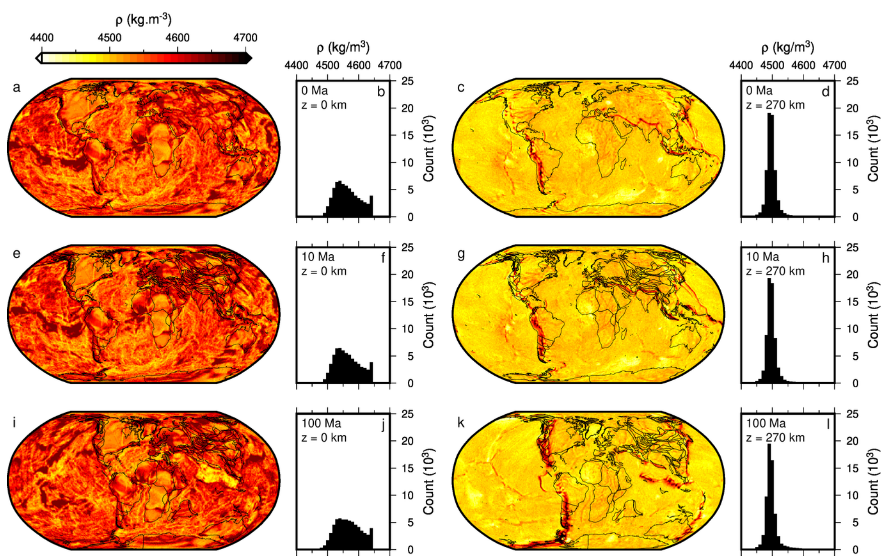
ρ (kg.m^{-3})
4400
4500
4600
4700
ρ (kg/m^3)
a
b
c
d
e
f
g
h
i
j
k
l
0 Ma
z = 0 km
0 Ma
z = 270 km
10 Ma
z = 0 km
10 Ma
z = 270 km
100 Ma
z = 0 km
100 Ma
z = 270 km
Count (10^3)
0
5
10
15
20
25

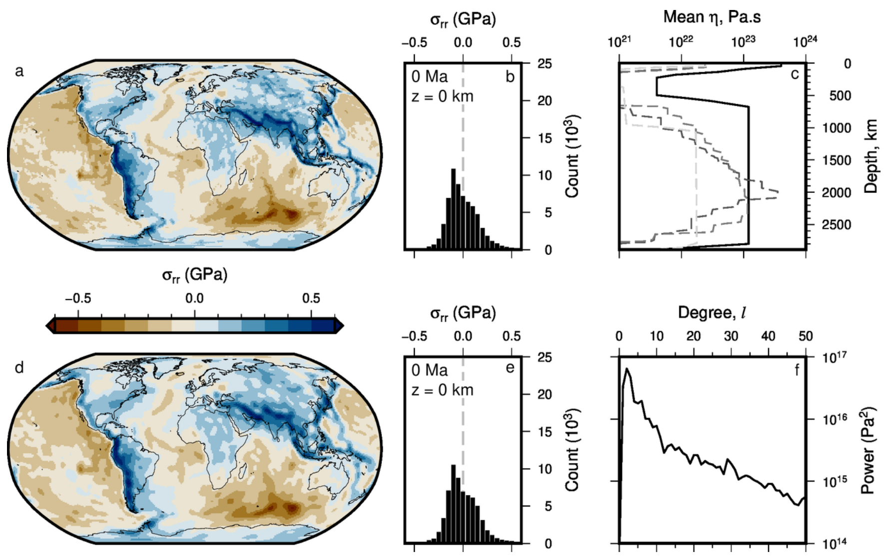
a
b
c
d
e
f
σ_{rr} (GPa)
0 Ma
z = 0 km
Count (10^3)
Mean η, Pa.s
Depth, km
Degree, l
Power (Pa^2)

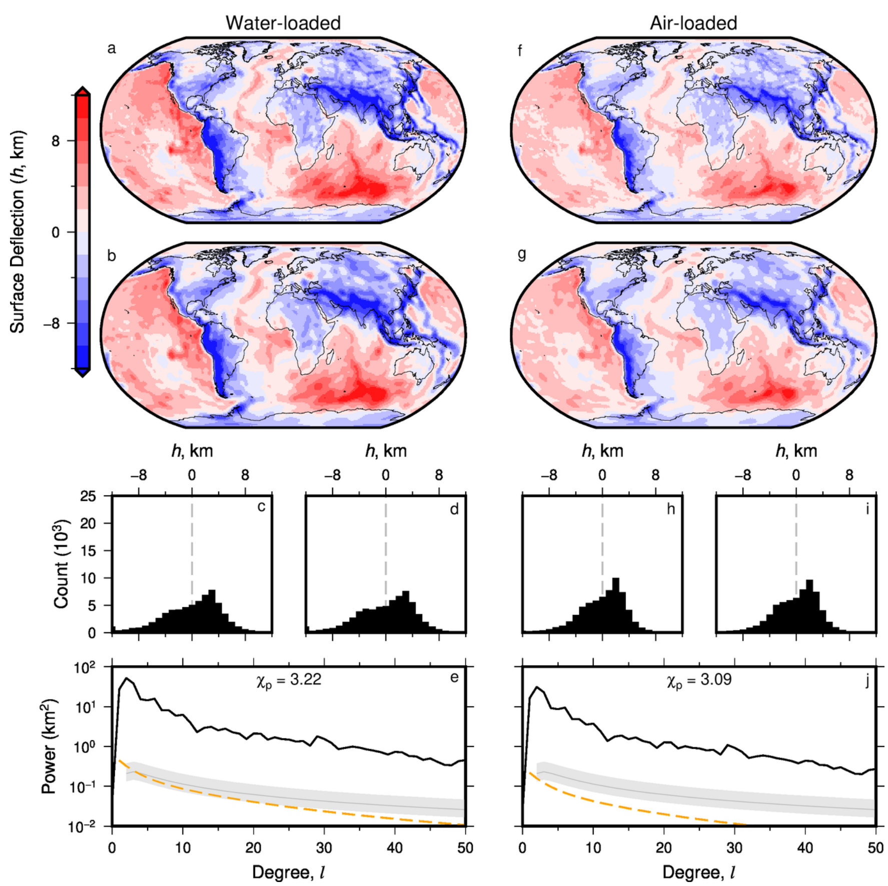
Water-loaded
Air-loaded
Surface Deflection (h, km)
h, km
Count (10^3)
χ_p = 3.22
χ_p = 3.09
Power (km^2)
Degree, l

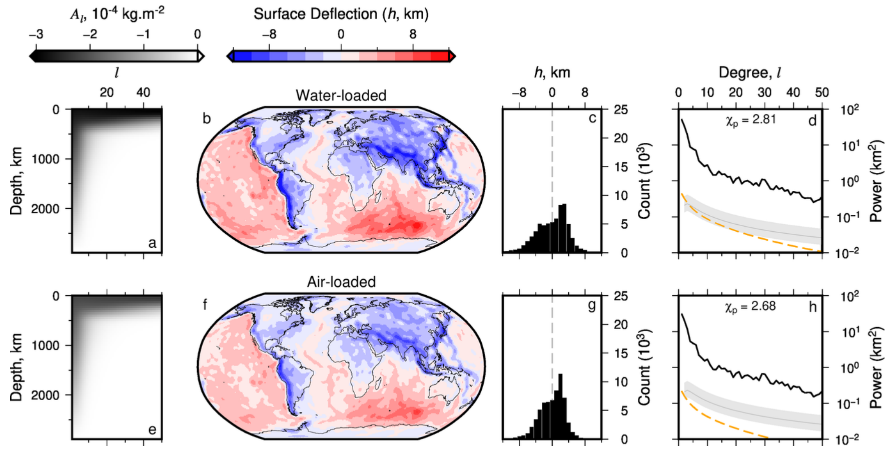

A_l, 10^{-4} kg.m^{-2}
Surface Deflection (h, km)
Water-loaded
Air-loaded
h, km
Degree, l
Depth, km
Count (10^3)
Power (km^2)
χ_p = 2.81
χ_p = 2.68

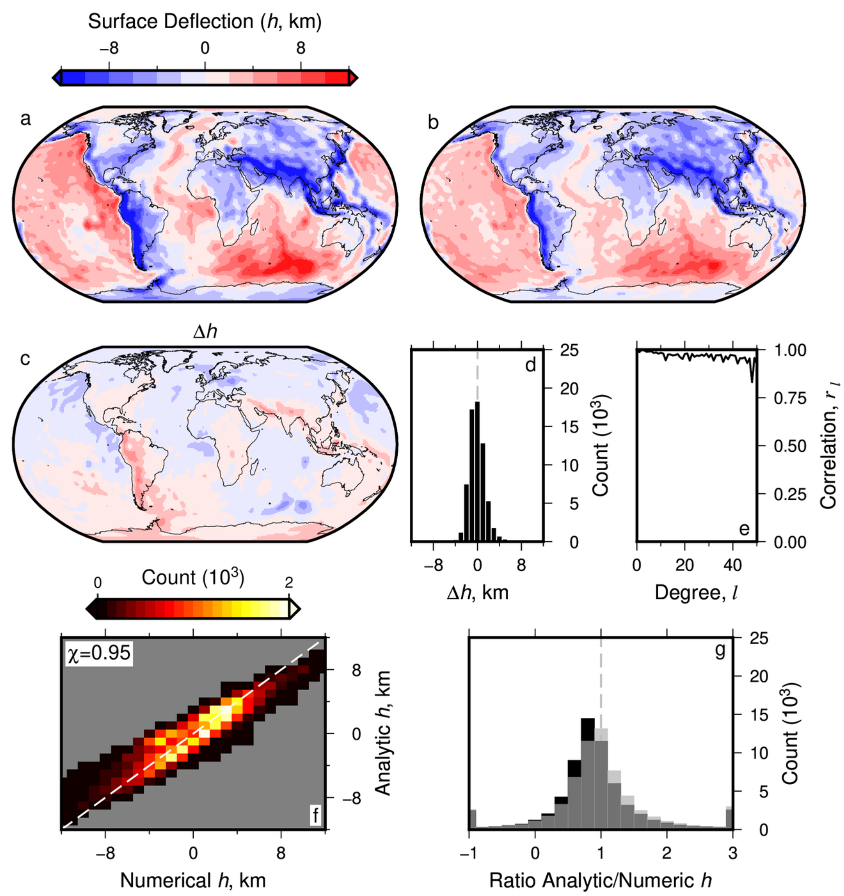

Surface Deflection (h, km)
Δh
Count (10^3)
Correlation, r_l
Δh, km
Degree, l
χ=0.95
Analytic h, km
Numerical h, km
Ratio Analytic/Numeric h

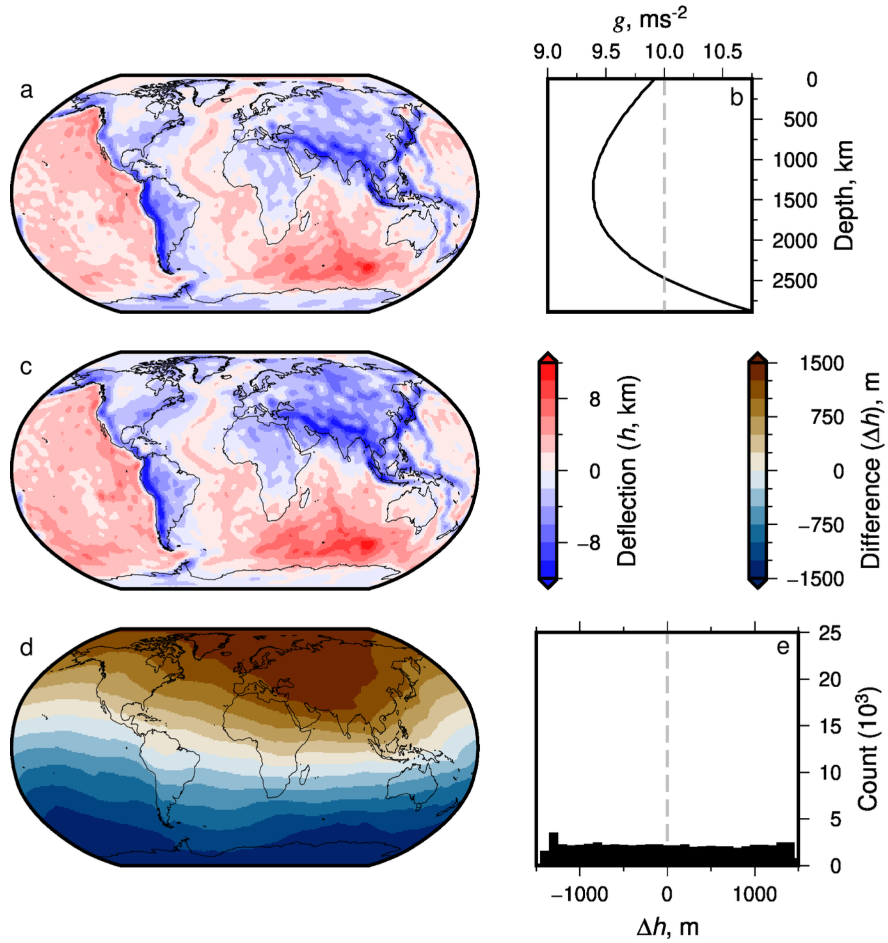
a
b
c
d
e
g, ms^{-2}
9.0 9.5 10.0 10.5
Depth, km
0 500 1000 1500 2000 2500
Deflection (h, km)
8 0 −8
Difference (Δh), m
1500 750 0 −750 −1500
Count (10^3)
25 20 15 10 5 0
−1000 0 1000
Δh, m

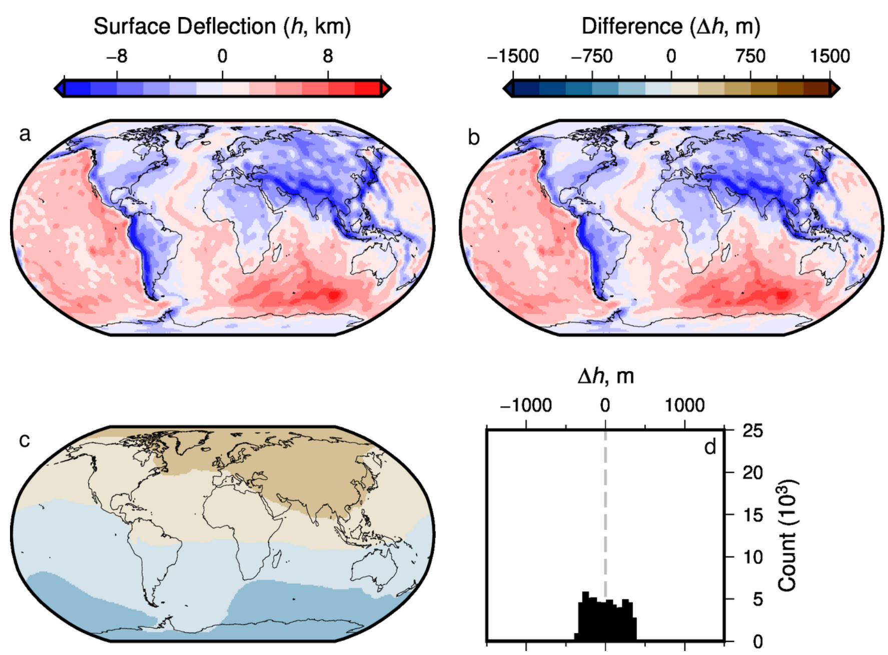
Surface Deflection (h, km)
−8 0 8
Difference (Δh, m)
−1500 −750 0 750 1500
a
b
c
d
Δh, m
−1000 0 1000
Count (10^3)
25 20 15 10 5 0

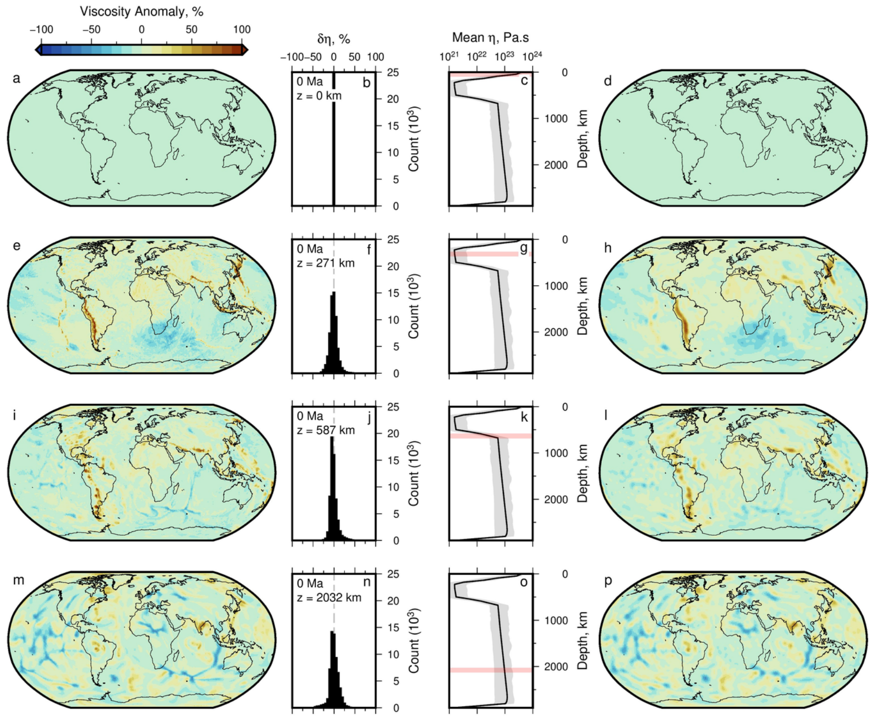
Viscosity Anomaly, %
−100 −50 0 50 100
δη, %
Mean η, Pa.s
Count (10³)
Depth, km
0 Ma
z = 0 km
z = 271 km
z = 587 km
z = 2032 km
a b c d e f g h i j k l m n o p

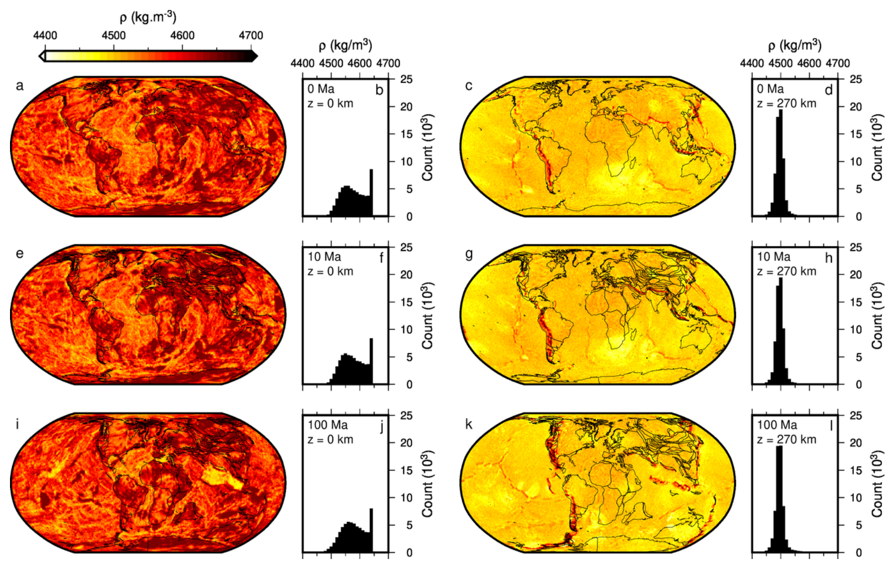
ρ (kg.m⁻³)
4400 4500 4600 4700
ρ (kg/m³)
Count (10³)
0 Ma
10 Ma
100 Ma
z = 0 km
z = 270 km
a b c d e f g h i j k l

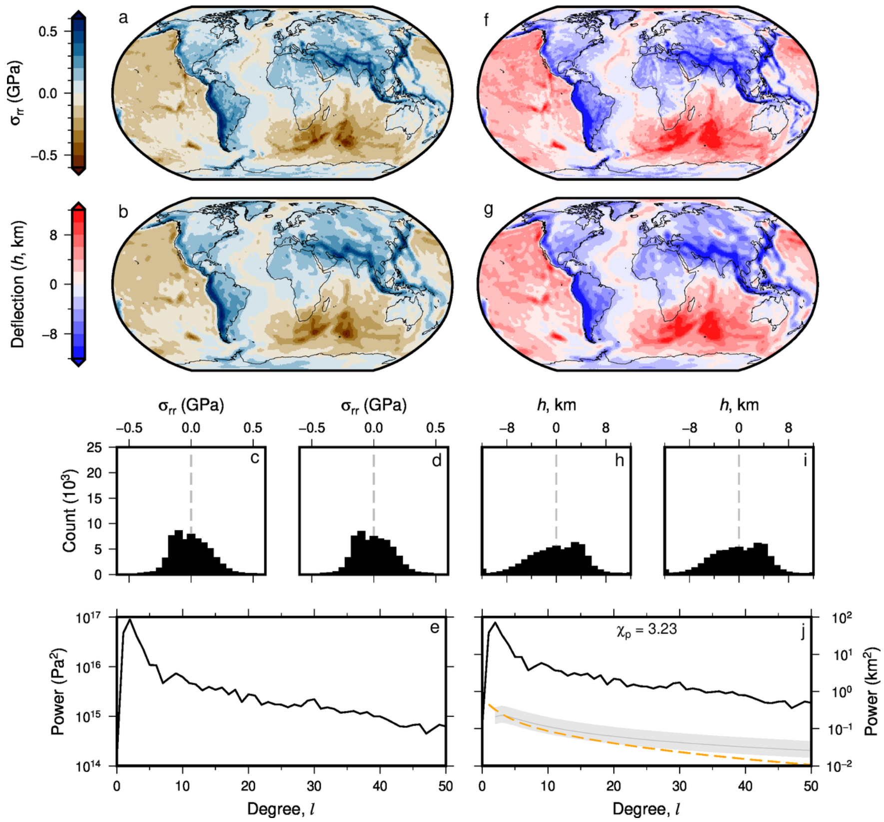
σrr (GPa)
Deflection (h, km)
a
b
f
g
c
d
h
i
e
j
Count (10³)
h, km
Power (Pa²)
Power (km²)
Degree, l
χp = 3.23

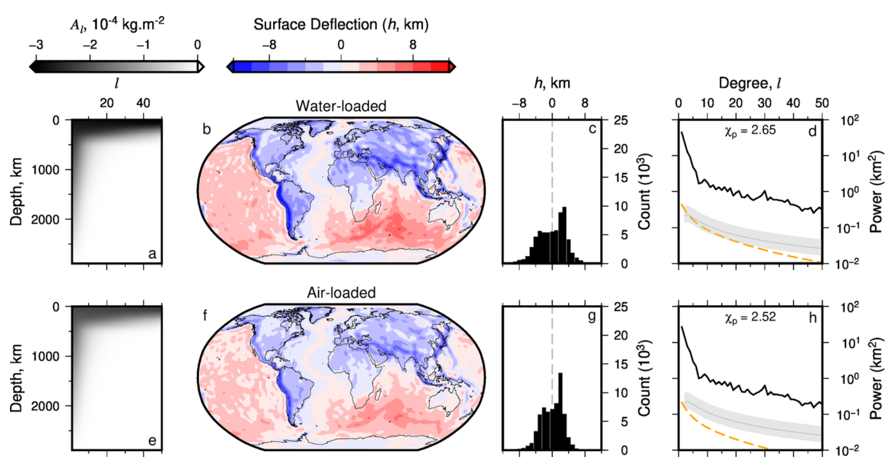
Al, 10⁻⁴ kg.m⁻²
Surface Deflection (h, km)
l
Depth, km
Water-loaded
Air-loaded
h, km
Count (10³)
Degree, l
Power (km²)
χp = 2.65
χp = 2.52
a
b
c
d
e
f
g
h

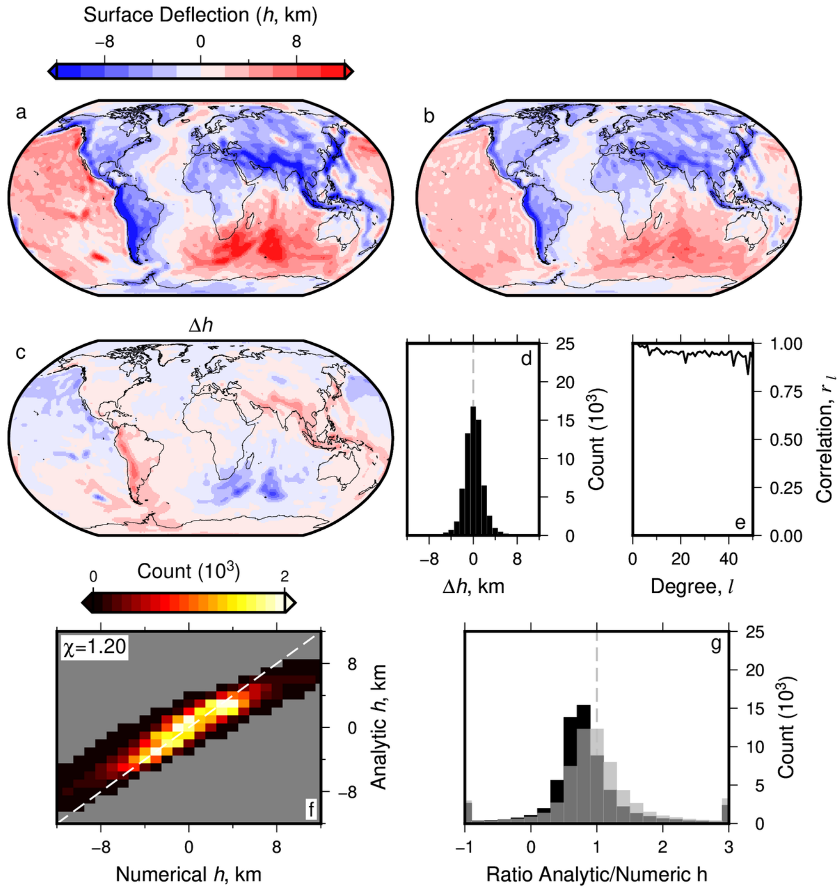

Surface Deflection (h, km)
−8
0
8
a
b
Δh
c
d
e
Count (10³)
Correlation, r_l
Δh, km
Degree, l
Count (10³)
0
2
χ=1.20
f
Analytic h, km
Numerical h, km
g
Ratio Analytic/Numeric h

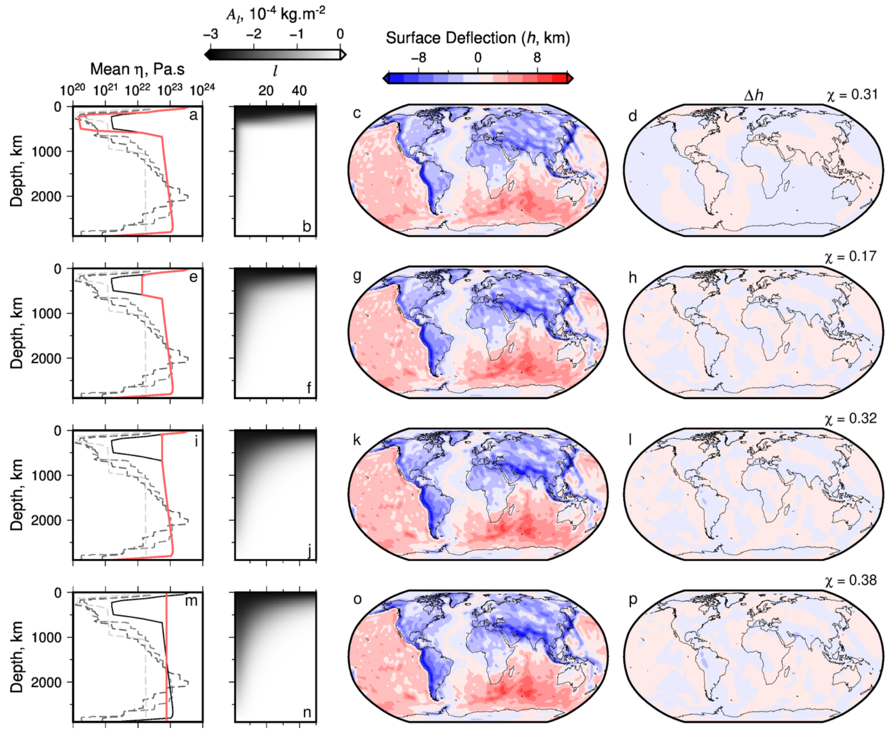

A_l, 10^{-4} kg.m^{-2}
−3 −2 −1 0
l
20 40
Surface Deflection (h, km)
−8 0 8
Mean η, Pa.s
10^{20} 10^{21} 10^{22} 10^{23} 10^{24}
Depth, km
0 1000 2000
Δh
χ = 0.31
χ = 0.17
χ = 0.32
χ = 0.38
a b c d e f g h i j k l m n o p

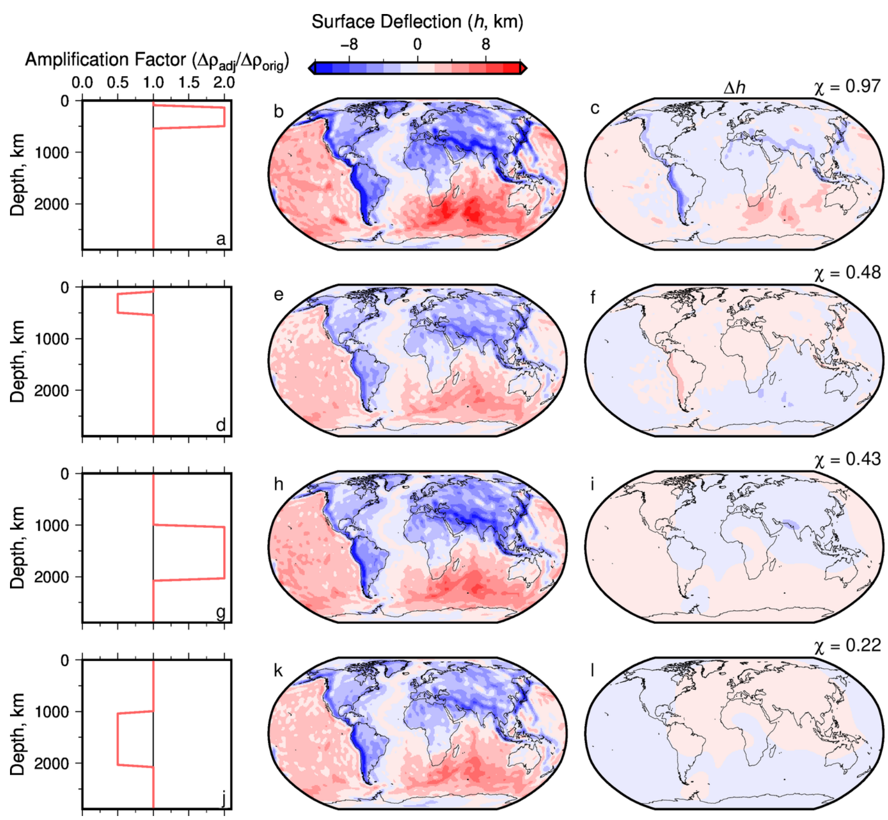

Surface Deflection (h, km)
−8 0 8
Amplification Factor ($\Delta\rho_{adj}/\Delta\rho_{orig}$)
0.0 0.5 1.0 1.5 2.0
Depth, km
0 1000 2000
Δh
χ = 0.97
χ = 0.48
χ = 0.43
χ = 0.22
a b c d e f g h i j k l

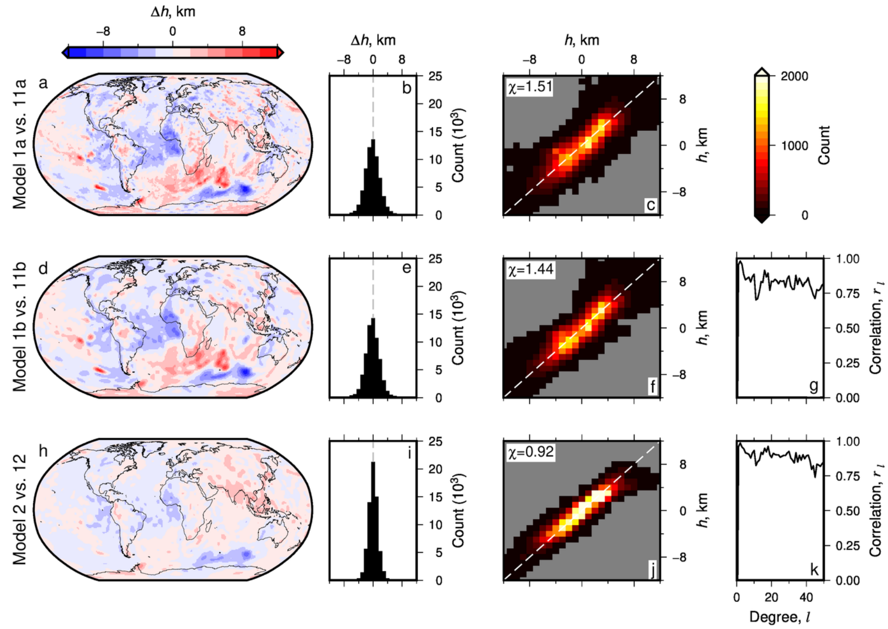
Δh, km
Model 1a vs. 11a
Model 1b vs. 11b
Model 2 vs. 12
Count (10³)
h, km
χ=1.51
χ=1.44
χ=0.92
Count
Correlation, r_l
Degree, l

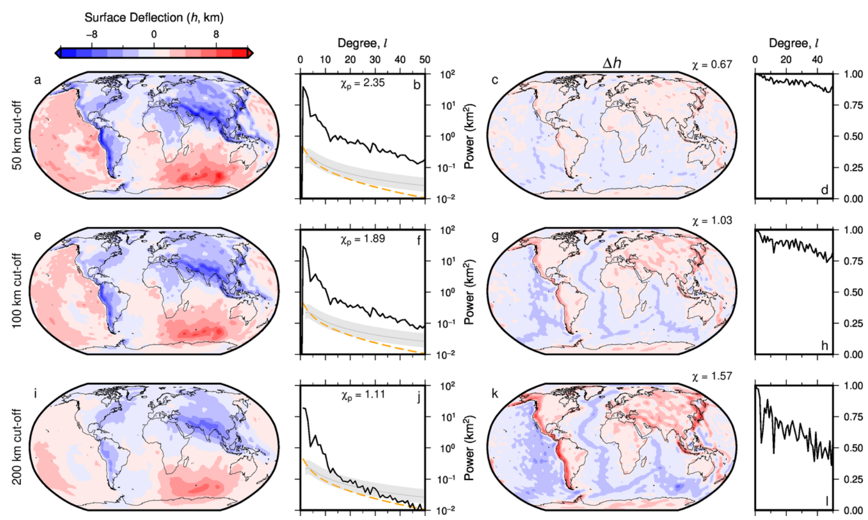
Surface Deflection (h, km)
50 km cut-off
100 km cut-off
200 km cut-off
Degree, l
Power (km²)
χp = 2.35
χp = 1.89
χp = 1.11
Δh
χ = 0.67
χ = 1.03
χ = 1.57
Correlation, r_l

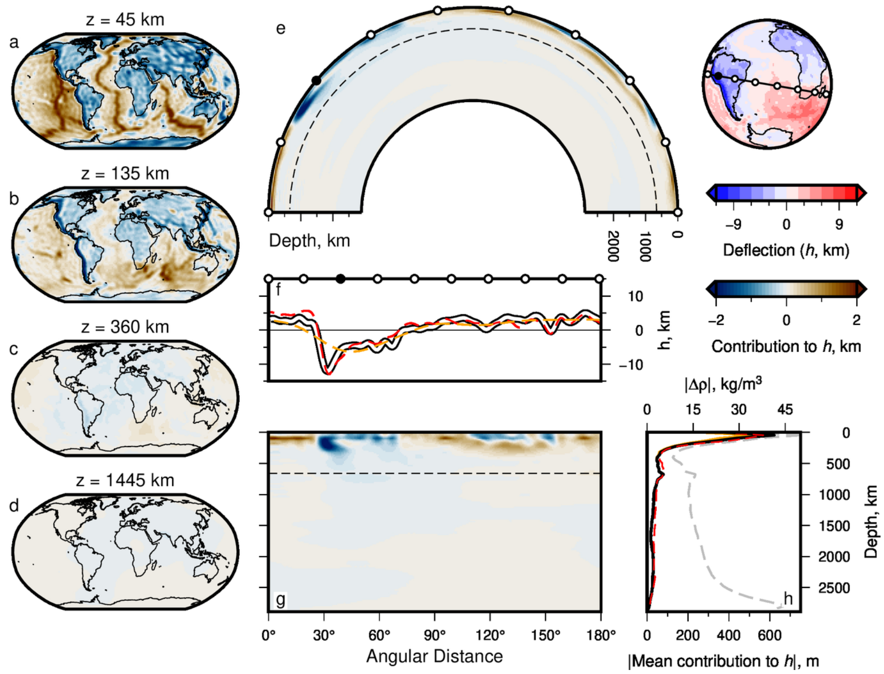
z = 45 km
a
z = 135 km
b
z = 360 km
c
z = 1445 km
d
e
Depth, km
2000
1000
0
–9
0
9
Deflection (h, km)
–2
0
2
Contribution to h, km
f
10
0
–10
h, km
|Δρ|, kg/m3
0
15
30
45
0
500
1000
1500
2000
2500
Depth, km
g
h
0°
30°
60°
90°
120°
150°
180°
Angular Distance
0
200
400
600
|Mean contribution to h|, m

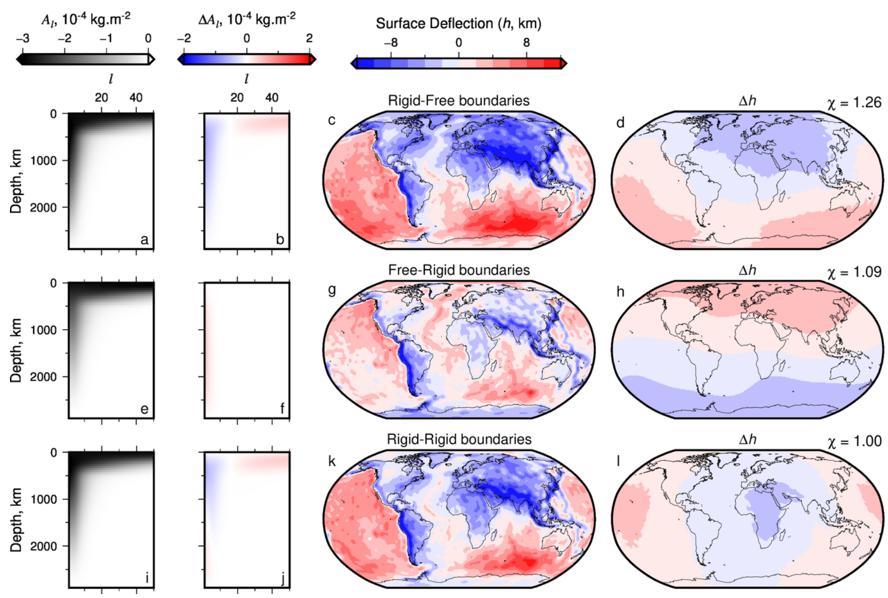
A_l, 10-4 kg.m-2
–3
–2
–1
0
ΔA_l, 10-4 kg.m-2
–2
0
2
Surface Deflection (h, km)
–8
0
8
l
20
40
0
1000
2000
Depth, km
a
b
Rigid-Free boundaries
c
Δh
χ = 1.26
d
e
f
Free-Rigid boundaries
g
Δh
χ = 1.09
h
i
j
Rigid-Rigid boundaries
k
Δh
χ = 1.00
l

Reconciling Surface Deflections From Simulations of Global Mantle Convection

Conor P. B. O'Malley[1], Gareth G. Roberts[1], James Panton[2], Fred D. Richards[1], J. Huw Davies[2], Victoria M. Fernandes[1,3], Sia Ghelichkhan[4]

[1]Department of Earth Science & Engineering, Imperial College London, Royal School of Mines, Prince Consort Road, London SW7 2BP, UK
[2]School of Earth & Environmental Sciences, University of Cardiff, Park Place, Cardiff CF10 3AT, UK
[3]now at Section 4.6 Geomorphology, GFZ Potsdam, Telegrafenberg, 14473 Potsdam, Germany
[4]Research School of Earth Sciences, Australian National University, 142 Mills Road, Acton, ACT 0200, Australia

Key Points:

- Numerical and analytic predictions of surface deflections from mantle convection simulations are compared.
- Impact of gravitation, excising shallow structure, boundary conditions, and different viscosity and density distributions are quantified.
- Calculated effective contributions to surface deflection emphasize dominance of upper mantle structure.

Corresponding author: Conor O'Malley; Gareth Roberts, `c_omalley1@msn.com`; `gareth.roberts@imperial.ac.uk`

Abstract

The modern state of the mantle and its evolution over geological timescales is of widespread importance for the Earth sciences. For instance, it is generally agreed that mantle flow is manifest in topographic and drainage network evolution, glacio-eustasy, volcanism, and in the distribution of sediments. An obvious way to test theoretical understanding of mantle convection is to compare model predictions with independent observations. We take a step towards doing so by exploring sensitivities of theoretical surface deflections generated from a systematic exploration of global mantle convection simulations. Sources of uncertainty, model parameters that are crucial for predicting deflections, and those that are less so, are identified. We start by quantifying similarities and discrepancies between deflections generated using numerical and analytical methods that are ostensibly parameterised to be as-similar-as-possible. Numerical approaches have the advantage of high spatial resolution, and can capture effects of lateral viscosity variations. However, treatment of gravity is often simplified due to computational limitations. Analytic solutions, which leverage propagator matrices, are computationally cheap, easy to replicate, and can employ radial gravitation. However, spherical harmonic expansions used to generate solutions can result in coarser resolution, and the methodology cannot account for lateral viscosity variations. We quantify the impact of these factors for predicting surface deflections. We also examine contributions from radial gravity variations, perturbed gravitational potential, excised upper mantle, and temperature-dependent viscosity, to predicted surface deflections. Finally, we quantify effective contributions from the mantle to surface deflections. The results emphasise the sensitivity of surface deflections to the upper mantle.

Plain Language Summary

Flow of rock within Earth's interior plays a crucial role in evolving the planet. It moves heat and chemicals from deep depths to the surface, for instance. It also moves the lithosphere—the Earth's outer rocky shell—which in turn impacts processes including mountain building, sea-level change, formation of volcanoes, river network evolution, and natural resource distribution. Consequently, we wish to understand the present state, and history, of flowing rock within Earth's interior. Observations exist to address this problem, and mathematics and computing tools can also be used to predict histories of flow and their impact on Earth's surface. We explore how assumptions incorporated into such models affect calculated deflections of Earth's surface. Predictions from different models are compared, with a view to identifying crucial modelling components. Surface sensitivity to deep flow is assessed, demonstrating how surface observations can enlighten flow histories.

1 Introduction

1.1 Background

Mantle convection plays a crucial role in Earth's evolution (e.g., Hager & Clayton, 1989; Parsons & Daly, 1983; Pekeris, 1935). It is well understood, for instance, that flow in the mantle is fundamental in the transfer of heat and chemicals from the deep Earth to the surface, in driving horizontal and vertical lithospheric motions (thus tectonic processes), and in magnetism via interactions with the core (e.g., Biggin et al., 2012; Davies et al., 2023; Foley & Fischer, 2017; Hoggard et al., 2016; Holdt et al., 2022; Pekeris, 1935). In turn, many processes operating at or close to Earth's surface are impacted, including glacio-eustasy, magmatism, climate, sediment routing, natural resource distribution, drainage network evolution, and development of biodiversity (e.g., Ball et al., 2021; Braun, 2010; Hazzard et al., 2022; O'Malley et al., 2021; Salles et al., 2017; Stanley et al., 2021). Clearly, understanding the physical and chemical evolution of the mantle has broad implications. Theoretical approaches to understanding mantle convection, including global simulations of mantle flow, can incorporate complex rheologies and geological histories (e.g., Forte, 2007; Hager & Clayton, 1989; D. P. McKenzie et al., 1974; Ribe, 2007; Ricard, 2007). Such models can include data assimilation, incorporating seismic tomographic (and other data) into flow solutions, iterating to optimize fits to observational constraints (e.g., Bunge et al., 2002, 2003; Glišović & Forte, 2016). A general goal is to identify theoretical models that are most Earth-like and, ultimately, to combine such approaches with observational inventories to provide accurate estimates of the actual history of mantle convection, and its role in governing Earth's surface evolution.

Properties of the convecting mantle, and its role in supporting topography at Earth's surface, have become significantly better known in the last decade or so, thanks principally to two suites of observations. First, there has been notable convergence in seismic tomographic imaging studies of Earth's interior, partly as a result of increased instrumentational coverage (e.g., EarthScope; Lekić & Fischer, 2014). Methodological advances, including full waveform inversion, have also improved understanding of mantle structure in many places (see, e.g., Fichtner et al., 2009, 2013; Fichtner & Villaseñor, 2015; French & Romanowicz, 2015). Mapping lithospheric thicknesses, which are crucial for disentangling origins of surface topography, has benefited from these improvements, as well as their own methodological advances (e.g., Priestley & McKenzie, 2013; F. D. Richards et al., 2021). Second, the inventory of residual oceanic age-depths—oceanic basement depths that cannot be explained by passive plate cooling with age, crustal or sedimentary processes—has become significantly more comprehensive (Davies et al., 2019; Hoggard et al., 2016; Holdt et al., 2022; Menard, 1973). Measured residual depths indicate that the convecting mantle supports oceanic bathymetry with amplitudes up to ~ 1 km, at horizontal scales ranging from those dictated by the elastic strength of the plate, i.e., $O(10^2)$ km, up to $O(10^4)$ km. The spectral power of these deflections approximately matches analytical estimates for mantle flow (e.g., Kaula's rule; Hoggard et al., 2016; Holdt et al., 2022; Kaula, 1963). In contrast, more complex continental rheologies and tectonic histories mean that quantifying modern topographic support of continental lithosphere from the mantle using observations is in its infancy (see, e.g., Davies et al., 2023; Hoggard et al., 2021). However, potential field data (e.g., free-air gravity anomalies and their relationship with topography, the geoid, etc.) and seismological information about plate structure provide useful information to constrain the current state of the convecting mantle beneath continents (and oceans; Audet, 2014; Hager & Clayton, 1989; Steinberger & O'Connell, 1997).

A growing inventory of geological and geomorphological observations from atop passive margins and within continental interiors provides increasingly coherent information about histories of mantle convection during the last ~ 100 Ma (see, e.g., Hoggard et al., 2021, for a recent summary). For instance, pressures and temperatures of melting obtained from the composition of Neogene and younger mafic rocks globally have recently been shown to be broadly consistent with estimates derived from shear wave tomography (Ball et al., 2022). Over-compacted stratigraphy and backstripped subsidence histories along African, American and Australian margins, combined with seismological and gravity data, provide evidence of vertical lithospheric motion due to flow in the mantle (e.g., Al-Hajri et al., 2009; Czarnota et al., 2013; Flament et al., 2015; Morris et al., 2020). Uplifted marine and coastal rock on all continents, especially in regions that have not recently experienced lithospheric shortening, provides information about sub-plate support of topography and mantle viscosity (e.g., Fernandes & Roberts, 2020; Gunnell & Burke, 2008; Lambeck et al., 1998). Lithospheric vertical motions from stratigraphic data (especially uplifted marine rock), from inverse modelling of drainage networks, and from denudation and sedimentary flux histories, provide indirect information about histories of sub-plate support beneath the continents (e.g., Galloway et al., 2011; Fernandes et al., 2019; O'Malley et al., 2021; Stanley et al., 2021). In summary, there now exists a global inventory of geophysical, geological and geomorphological observations, providing information about the current state of the mantle and clues about its spatio-temporal evolution, especially during the last few tens of millions of years.

Despite these advances, observations providing information about the history of mantle convection are sparse in places, especially within continental interiors. Sparsity increases globally back through time (see, e.g., Hoggard et al., 2021). Theoretical or modelling approaches can, in principle, be used to fill in spatio-temporal observational gaps, to quantify the history of mantle convection. A general goal is to combine theoretical insights into mantle convection, e.g., via numerical simulation or analytical advances, with the growing observational inventory. In our view, there are two crucial steps to doing so. First, a quantitative understanding of the implications of modelling choices (e.g., numerical vs. analytical solutions, boundary conditions, rheological assumptions) for predicting quantities that are measurable at Earth's surface (e.g., surface deflections, gravitational potential, heat flow) is required. There now exists a large body of models and theoretical approaches that can be compared. Second, quantification of the discriminatory power of observations at Earth's surface for identifying Earth-like simulations of mantle convection is needed. Our focus in this paper is on addressing the first topic. We then discuss the second topic, with a view to making use of independent observations in future work.

1.2 Approach

A large body of global mantle convection simulators and simulations exist, which can, in principle, be used to fill observational gaps and predict histories of mantle convection (e.g., Baumgardner, 1985; Bunge & Baumgardner, 1995; Davies et al., 2013; Flament et al., 2015; Ghelichkhan et al., 2021; Hager et al., 1985; Moucha & Forte, 2011; Steinberger & Antretter, 2006). This considerable body of existing work provides an opportunity to assess the role different features arising from the natural complexity of mantle convection play in generating surface observables. For instance, mantle convection simulations can incorporate radial and temperature-dependent viscosity, radial gravitation, deflection of gravitational potential fields and their subsequent impact on flow, mineralogical phase changes, compressibility, different surface and core-mantle boundary slip conditions (e.g., rigid/no-slip, free-slip), chemical and thermal buoyancy, and plate motions and/or tomographic constraints on mantle structure (e.g., Baumgardner, 1985; Corrieu et al., 1995; Crameri et al., 2012; Panasyuk et al., 1996; Tackley et al., 1993; Zhong et al., 2008). These assumptions can result in quite different predictions of surface deflections. An obvious question then, which we seek to address, is, can surface observations be used to discriminate between simulations, and, ultimately, to determine the history of mantle convection?

Aside from the fundamental choice of governing equations underpinning simulations, there exist different mathematical and computational approaches to predict the surface impact of mantle convection. These approaches sit within two broad families: numerical simulations (e.g., CitcomS, TERRA, ASPECT; Bangerth et al., 2023; Baumgardner, 1985; Zhong et al., 2000), and propagator matrix based, quasi-analytical techniques, that can be solved in two or three dimensions, and importantly for our purposes, spherically and spectrally (e.g., Parsons & Daly, 1983; Hager & O'Connell, 1979; Colli et al., 2016). Here, we investigate similarities and differences arising between surface deflections predicted by propagator matrix and numerical schemes (see Figure 1). We do so by comparing predictions generated using the numerical code TERRA, and a modified version of Ghelichkhan et al. (2021)'s analytical (propagator matrix) code. We develop a flexible scheme that could be used to compare predictions from other whole-Earth models of mantle convection.

This paper is arranged as follows. First, the conservation equations solved to predict mantle flow and subsequent surface deflections, solution methodologies, and model parameterizations are described. Second, numerical and analytical techniques for estimating surface deflection are summarized. Third, three metrics for comparing predicted surface deflections are described. Fourth, parameterizations and assumptions tested in this paper are described, and resultant modifications to surface deflection predictions are quantified. We start by comparing predictions that arise from as-similar-as-possible parameterizations of numerical and analytical approaches. These tests compare surface deflections calculated using the entirety of the modelling domains, i.e., from the core-mantle boundary (CMB) to the surface; no shallow structure is excised. These reference models are purposefully simple, e.g., incompressible, constant gravitational acceleration (no self-gravitation or radial variation in gravitation), radial viscosity independent of temperature. The convection simulations are driven by plate motions generated using geological observations, which are described below. For clarity, the simulations do not incorporate information about the mantle derived from tomographic models. We then systematically examine the impact of incorporating radial variations in gravitational acceleration, contribution to flow from deflection of the gravitational potential field, removal of shallow density/viscosity structure, choice of surface and CMB slip conditions, inclusion of temperature dependent viscosity, and amplification/reduction of viscosity and density anomalies in the upper and lower mantle. We explore a closed-loop modelling strategy in which predicted surface deflections from these relatively complex models are compared to results from reference models. Finally, a methodology for assessing effective contributions to surface topography from mantle anomalies is presented.

We stress that we purposefully avoid isolating passive or plate-driven surface deflection and sub-plate support from the simulations unless stated explicitly. The central focus of this work is merely on quantifying contrasting predictions of surface topography that arise simply from choices made when simulating mantle convection using numerical and analytical approaches. We compare results to estimates of sub-plate support from oceanic age-depth residuals with a view to quantifying corrections necessary to convert surface deflections predicted by mantle convection simulations into estimates of sub-plate support.

2 Equations Governing Predicted Mantle Convection

Theoretical predictions of surface displacements from mantle convection arise from the application of physical laws that take the form of conservation equations for mass, momentum and energy (see, e.g., Hager & O'Connell, 1981; Parsons & Daly, 1983). Here, we solve those equations across a 3D spherical domain using the finite element code TERRA (Baumgardner, 1985; Bunge & Baumgardner, 1995, etc.). Under this formulation, theoretical convection in an incompressible fluid can be expressed by the following three dimensionless equations (e.g., Baumgardner, 1985; Davies et al., 2013; D. P. McKenzie et al., 1974; Parsons & Daly, 1983). First, the continuity condition for conservation of mass,

$$\nabla \cdot \mathbf{u} = 0, \tag{1}$$

where $\mathbf{u}$ is the fluid velocity vector. Since the Prandtl number is likely to always be extremely large in this system—mantle viscosity is expected to be many orders of magnitude larger than the product of density and thermal diffusivity—inertial terms can be neglected (e.g., Parsons & Daly, 1983). Second, the equation of motion,

$$\nabla \sigma = -\rho' \mathbf{g}, \tag{2}$$

where

$$\rho' = -\alpha \rho_0 (T - T_{\text{ref}}). \tag{3}$$

σ is the 3×3 stress tensor where the (radial) hydrostatic component balancing the reference density structure has been subtracted, ρ' is the density difference due to temperature, α is the coefficient of thermal expansion, T is temperature, T_{ref} is a radially varying reference temperature structure, which has a constant value in the mid-mantle and joins to a cold thermal boundary layer near the surface and a hot one at the CMB, reaching the actual surface, T_s, and core mantle boundary, T_{CMB} temperatures at the respective boundaries, and $\mathbf{g}$ is gravitational acceleration acting radially (see Table 1). This stress tensor σ_{ij} is decomposed into deviatoric and lithostatic components:

$$\sigma_{ij} = \tau_{ij} - p\delta_{ij}, \tag{4}$$

where τ_{ij} is the deviatoric stress tensor, p is dynamic pressure and δ_{ij} is the Kronecker delta function. The deviatoric stress tensor and the strain-rate tensor, $\dot{\epsilon}_{ij}$, are related by:

$$\tau_{ij} = 2\eta\dot{\epsilon}_{ij} = \eta\left(\frac{\partial \mathbf{u}_i}{\partial x_j} + \frac{\partial \mathbf{u}_j}{\partial x_i}\right), \tag{5}$$

where η is viscosity, and $\partial/\partial x_i$ is the spatial partial derivative. By combining equations 2, 4 and 5 we solve the equation of motion:

$$\frac{\partial(\eta\epsilon_{ij})}{\partial x_j} - \frac{\partial p}{\partial x_i} = -\rho' g\delta_{ir}, \tag{6}$$

where g is the scalar value of $\mathbf{g}$ and δ_{ir} is the Kronecker delta selecting the radial direction r.

We first examine predictions from models in which viscosity varies only with depth, i.e., $\eta = \eta_0 \times \eta_r$, where η_0 is reference viscosity (see Table 1), and η_r is a scaling factor dependent only on radius, plotted with model results as appropriate throughout this manuscript. We then include temperature dependence of viscosity, i.e., $\eta = \eta_0 \times \eta_r \times \eta_T$, where

$$\eta_T = \exp(z' - 2T'). \tag{7}$$

Dimensionless depth, $z' = z/d$, where $d = z_{\text{surface}} - z_{\text{CMB}} = 2890$ km, and dimensionless temperature $T' = (T - T_s)/(T_{\text{CMB}} - T_s)$, where $T_{\text{CMB}} - T_s = 2700$ K.

Finally, the heat transport equation is solved to ensure conservation of energy:

$$\frac{\partial T}{\partial t} + \mathbf{u}\cdot\nabla T = \kappa\nabla^2 T + \frac{H}{C_p}, \tag{8}$$

where κ is thermal diffusivity, H is internal heat generation and C_p is specific heat capacity. See Table 1 for parameter values and units. Heat generation within the mantle depends on the distribution of radiogenic isotopes (e.g., Ricard, 2015). Concentrations of such elements can be tracked in TERRA, using particles, varying as a consequence of flow and melting (see, e.g., Panton et al., 2023; van Heck et al., 2016, for full explanation). The bulk composition field, C, which varies between 0 and 1, is also tracked on particles and calculated for each of the finite elements in the model. The end-members represent completely depleted/harzburgitic material ($C = 0$), and fully enriched/basaltic material ($C = 1$). As a result, radiogenic heat production across the whole mantle volume varies, being ≈ 24 TW (5.8×10^{-12} W kg^{-1}) at 1.2 Ga, and ~ 18 TW (4.5×10^{-12}

W kg^{-1}) by 0 Ma. Simulations are initialised such that the average mantle composition is $C = 0.20$ (Panton et al., 2023), and composition obeys the conservation equation:

$$\frac{\partial C}{\partial t} = -\nabla \cdot (C\mathbf{u}). \tag{9}$$

2.1 Numerical Modelling Strategy

The Stokes equations described above are solved by the finite element method on a series of stacked spherical shells composed of nodes based on a subdivision of a regular icosahedron, with an identical geometry for each shell when projected onto the CMB (see, e.g., Figure 1 of Baumgardner, 1985). The radial spacing of consecutive shells is 45 km, which is the same as the mean horizontal spacing of the elements across the entire model domain. The stacking of identically partitioned shells leads to a finer mean horizontal resolution of ≈ 33 km at the CMB, and a coarser resolution of ≈ 60 km at the surface. The surfaces of the uppermost elements in the shallowest shell lie at zero depth. To enable estimates of stress from these models to be directly compared with analytical solutions obtained from Green functions across layer boundaries, the predicted values of deviatoric stress were calculated using the calculated velocities from the nearest shells using the interpolating linear shape functions of the underlying finite elements, while the dynamic pressure is calculated directly at the surface (Section 3.3).

Each numerical model presented in this paper has two computational stages: 'spin-up', which is used to initialize the model, and the geologically more realistic 'main' stage, from which we generate predictions of surface deflections. The spin-up stage includes 2.2 billion years of model run-time. It has the following conditions imposed to avoid sharp velocity and temperature gradients, and sudden reorganization of mantle flow when the main model starts. First, a free-slip condition is imposed at the surface. Second, an initial, random white noise temperature field generated with power across spherical harmonic degrees 1-19, is inserted. Mean mantle temperature is initially 2000 K. Mantle convection arises naturally over the first two billion years of model run-time. A fixed-slip surface velocity condition is then applied to the surface for 200 Ma. These velocities are set to be equal to those at 1 Ga extracted from the reconstructions of Merdith et al. (2021); the vertical component of slip is zero. The resultant mantle structure is used as the initial condition for the main model.

The main model routine predicts flow from 1 Ga to the present-day (0 Ma). It includes an isothermal condition imposed at the surface, $T_s = 300$ K. A fixed-slip condition is imposed such that the vertical component of $\mathbf{u}$ is zero. Horizontal slip is prescribed using the plate reconstructions of Merdith et al. (2021); these are applied in 1 Ma long stages. As such, stirring by plate drift and slab sinking play a role in driving mantle flow in these models. An isothermal condition is also imposed at the core-mantle boundary such that $T_{\text{CMB}} = 3000$ K. A free-slip velocity boundary condition is imposed there, i.e., so the radial component of the mantle flow velocity $(\mathbf{u_r}) = 0$. While this radial velocity boundary condition is of the Dirichlet type, in a free-slip boundary condition no tangential restriction is imposed on the flow velocity but rather on the tangential deviatoric stresses acting on the boundary ($\tau_{r\theta}$, $\tau_{r\phi}$ where r, θ and ϕ are the radial and two tangential directions respectively), which are zero. Horizontal components of slip are allowed to naturally emerge and evolve subject to lowermost mantle flow. Plume behaviour is not artificially suppressed.

To ensure numerical stability and computational accuracy in these simulations, the reference viscosity, η_0, is set to 4×10^{21} Pa s. This value is probably an order of magnitude greater than the viscosity of the actual upper mantle (e.g., Forte, 2007; Ghelichkhan et al., 2021; Mitrovica & Forte, 2004, and references therein). Consequently, flow velocities in the simulations are likely to be significantly slower than in actuality. An obvi-

Table 1. Summary of Model Parameters.

Parameter	Symbol	Value	Units
Surface temperature	T_s	300	K
Core-mantle boundary temperature	T_{CMB}	3000	K
Internal heating rate	H	See text.	W kg^{-1}
Thermal expansivity	α	2.5×10^{-5}	K^{-1}
Thermal conductivity	K	4	W m^{-1}K^{-1}
Thermal diffusivity	κ	8.08×10^{-7}	m^{2}s^{-1}
Specific heat capacity	C_p	1100	J kg^{-1}K^{-1}
Reference viscosity	η_0	4×10^{21}	Pa s
Reference density	ρ_0	4500	kg m^{-3}
Overlying fluid density	ρ_w	1 or 1030	kg m^{-3}

ous cause for concern is that using actual (comparatively fast) plate velocities as surface boundary conditions atop a relatively slowly convecting 'mantle' is likely to induce unrealistic flow. To address this issue, imposed plate velocities are scaled such that the root-mean squared (RMS) values of the actual applied velocities ($\approx$ 5 cm yr^{-1} unscaled) match RMS values of surface velocities ($\approx$ 2.5 cm yr^{-1}) calculated during the spin-up phase (before plate velocities are imposed on the model) when the model mantle is convecting naturally and not being driven by surface velocities. The applied surface plate velocities are therefore scaled by a factor of 0.5 (i.e., 2.5/5) in the simulations examined in this study. To ensure that volumetric fluxes through ridges and subduction zones are realistic, simulation run times are increased by a factor of 2; i.e., the 1 Myr long plate stages are run for twice their elapsed time (2 Myr), but at half the speed. All times stated throughout the rest of this manuscript refer to times re-scaled for real-world comparison; i.e., the actual age of the respective plate stage.

For the reference case (Model 1), these conditions lead to the density distributions shown in Figure 2. Surface layer density anomalies occur only as a result of predicted compositional variation, since the surface temperature, T_s, is constant globally. This model represents the first of two reference numerical models examined in this contribution. It has the radial viscosity structure shown in Figure 3c. Later, we investigate a second numerical model incorporating temperature-dependent viscosity (Equation 7). In the following section, we describe two approaches that use output from these models to calculate instantaneous surface deflections.

3 Numerical and Analytical Calculations of Surface Deflection

We examine two widely used approaches for calculating radial stress, σ_{rr}, and deflections, h, at Earth's surface (Figure 1). First, we investigate numerical solutions obtained using the TERRA software. A methodology for representing this data in the spherical harmonic domain is then described. Secondly, we investigate analytical solutions obtained in the spherical harmonic domain using propagator matrix techniques.

3.1 Numerical Solution

Following Parsons and Daly (1983), surface deformation is estimated from numerical simulations of mantle convection by making use of the requirement that normal stress is continuous across the upper boundary of the solid Earth (see also D. McKenzie, 1977;

Ricard, 2015). In other words, radial stresses generated by the solid Earth are required to be balanced by stresses generated by the overlying (oceanic or atmospheric) fluid. There are three contributions to normal stress at this boundary from the mantle: hydrostatic stress that would exist even in the absence of convection, dynamic stress arising from convection, and viscous stress which opposes fluid motion (see Equations 2–6). To satisfy the continuity condition, these stresses must be balanced by those generated by the water (or air) column atop this boundary. If the pressure from the overlying column is hydrostatic, the resultant condition is

$$\rho_w g_R h = \rho_m g_R h + \sigma_{rr}, \tag{10}$$

where σ_{rr} (defined in Equation 2) incorporates deviatoric viscous stresses generated by mantle convection and dynamic pressure ($\sigma_{rr} = \tau_{rr} - p$), obtained by solving Equation 2. In practice, since values for this term are obtained by subtracting radial lithostatic stress from the total stress, values of σ_{rr} integrate to zero globally. g_R is gravitational acceleration at Earth's surface, ρ_m is the mean density for the surficial layer, and ρ_w is the density of the overlying fluid (see Table 1). Figure 3a-b shows normal stresses, σ_{rr}, calculated at the surface of Model 1, and associated statistics. This model was generated using the viscosity structure shown in Figure 3c. By convention, positive stresses imply compression and hence downward surface deflection, which could be manifest as lithospheric drawdown, i.e., subsidence. Prominent regions of positive stress anomalies in this model include locations atop imposed collision zones, where subduction naturally results, e.g., along the Pacific margin of South America. Negative stresses imply dilation and hence positive lithospheric support (i.e., surface uplift). Figure 3a shows dilatational stresses beneath Southern Africa, for example, and along mid-oceanic ridges in the Indian and Atlantic Oceans. Note that we do not impose additional oceanic plate cooling, e.g., due to hydrothermal circulation at ridges. Cooling and subsequent subsidence, as well as passive return flow at ridges, arise naturally from solution of the governing equations laid out in Section 2.

Surface deflection arising in response to predicted mantle convective flow, h, is approximated by rearranging Equation 10,

$$h \approx -\frac{\sigma_{rr}}{(\rho_m - \rho_w) g_s}, \tag{11}$$

where g_s is gravitational acceleration at the surface, here = 10 m s^{-2}. In this application of TERRA, surface deflections are estimated from radial stresses at times of interest (e.g., the present-day) by re-running one time-step of the model. During that time, a free-slip boundary condition, for which analytical approximations for surface deflection exist, is imposed instead of the plate-slip condition prescribed during the main model run routine (see Section 3.3; Ricard, 2015). We assess the accuracy of modifying boundary conditions in this way by converting calculated deflections into the spherical harmonic domain and comparing them to predictions generated from the analytical propagator matrix (Figure 3d–f). The consistent boundary flux (CBF) method provides an alternative means to accurately calculate normal stresses (Zhong et al., 1993). Previous benchmarking with TERRA has shown mean errors of a few percent or less for surface deflection predictions at low harmonic degrees, $l \leq 16$ (Davies et al., 2013).

3.2 Spherical Harmonic Representation of Surface Deflection

Transforming stress, or surface deflections, calculated using numerical approaches into the frequency domain provides a means of quantifying their spectral power, i.e., the magnitude of contribution to the total signal from different wavelengths. We do so using spherical harmonics, since the models that we investigate are global in scope. Any real, square-integrable function over the surface of the Earth can be described as a function of longitude θ and latitude ϕ by a linear combination of spherical harmonics of degree l and order m,

$$f(\theta, \phi) = \sum_{l=1}^{L} \sum_{m=-l}^{l} f_{lm} Y_{lm}(\theta, \phi). \tag{12}$$

The spherical harmonic functions Y_{lm} are the natural orthogonal set of basis functions on the sphere, and f_{lm} are the spherical harmonic coefficients. As an example, Figure 3d shows spherical harmonic expansion of the surface stress field predicted by Model 1 at 0 Ma (cf. Figure 3a). We call this result Model 1b, and the original, full-resolution numerical result Model 1a. The fidelity of the spherical harmonic expansion is demonstrated by the similarity of the maps and histograms shown in panels a–b and d–e.

$$P_l = \sum_{m=-l}^{l} f_{lm}^2 \tag{13}$$

gives the total power across all spherical harmonics of a given degree l. Average power for each mode m within degree l, $\hat{P}_l = P_l/(2l+1)$, since there are $2l+1$ modes (orders) per degree—we do not explore this definition of power in this contribution, and present only total power per degree (see, e.g., Hoggard et al., 2016; Holdt et al., 2022). Figure 3f shows power as a function of degree under that convention from the expansion shown in panel d. Using the total power per degree convention, Hoggard et al. (2016) (their Supporting Information) derived a rule-of-thumb for estimating the power spectrum of dynamic topography, P_l^{DT}, using Kaula (1963)'s approximation for the long-wavelength gravity field of Earth as a function of l:

$$P_l^{DT} \approx \left(\frac{GM}{ZR^2}\right)^2 \left(\frac{2}{l} - \frac{3}{l^2} + \frac{1}{l^4}\right), \tag{14}$$

where G is the gravitational constant, $M = 5.97 \times 10^{24}$ kg is the mass of the Earth, $R \approx 6370$ km is Earth's radius, and long-wavelength admittance between gravity and topography $Z = 12$ mGal km^{-1}, which we make use of in the remainder of the paper for reference. Although we acknowledge that the appropriate value of low-degree admittance varies as a function of Earth's viscosity profile, and the depth and wavelength of its internal density anomalies (Colli et al., 2016), previous studies have found that assuming an average value of 12 mGal km^{-1} provides a reasonable approximation of observed residual topographic trends (Hoggard et al., 2016).

Finally, it is useful to note that Jeans (1923) related spherical harmonic degree to wavelength λ on Earth's surface via,

$$\lambda \approx \frac{2\pi R}{\sqrt{l(l+1)}}. \tag{15}$$

3.3 Analytical Solutions

The second methodology used to calculate surface deflection in response to mantle convection is the analytical propagator matrix technique (e.g., Craig & McKenzie, 1987; Gantmacher, 1959; Ghelichkhan et al., 2021; Parsons & Daly, 1983; M. A. Richards & Hager, 1984). The approach we take stems from the work of Hager and O'Connell (1981). They used Green's functions to solve the equations of motion in the spherical harmonic domain. Those solutions are used to generate sensitivity kernels that straightforwardly relate, for example, density or temperature anomalies in the mantle to surface deflections.

The kernels are generated in the frequency domain, and constructed such that surface deflection sensitivity to mantle (e.g., density) anomalies is calculated as a function of depth (or radius) and wavenumber. A global spherical harmonic implementation introduced by Hager et al. (1985) has been extended to include compressibility, the effect of warping of the gravitational potential by subsurface density distributions, and radial gravity variations calculated using radial mean density values (Corrieu et al., 1995; Forte & Peltier, 1991; Hager & O'Connell, 1981; M. A. Richards & Hager, 1984; Thoraval et al., 1994).

In this study, following Ghelichkhan et al. (2021), surface deflection for each spherical harmonic coefficient, h_{lm}, is calculated in the spectral domain such that

$$h_{lm} = \frac{1}{(\rho_m - \rho_w)} \int_{R_{\mathrm{CMB}}}^{R} A_l \delta\rho_{lm}(r) \cdot \mathrm{d}r. \tag{16}$$

Products of the sensitivity kernel, A_l, and density anomalies, $\delta\rho_{lm}$, of spherical harmonic degree, l, and order, m, are integrated with respect to radius, r, between the core-mantle boundary and Earth's surface radii, R_{CMB} and R, respectively. The sensitivity kernel is given by

$$A_l = -\left(\frac{\eta_0}{R g_R}\right)\left(u_1 + \frac{\rho_w}{\rho_0} u_3\right), \tag{17}$$

where $u_n(r)$ represents a set of poloidal variables, which are posed for solution of the set of simultaneous equations by matrix manipulation, such that

$$u(r) = \begin{bmatrix} y_1\eta_0 & y_2\eta_0\Lambda & (y_3 + \bar{\rho}(r)y_5)r & y_4 r\Lambda & y_5 r\rho_0\Lambda & y_6 r^2\rho_0 \end{bmatrix}^T, \tag{18}$$

where $\Lambda = \sqrt{l(l+1)}$, and y_1 to y_6 represent the spherical harmonic coefficients of radial velocity v_r, lateral velocity $v_{\theta,\phi}$, radial stress σ_{rr}, lateral stress $\sigma_{r\theta,\phi}$, gravitational potential V, and gravitational potential gradient $\partial V/\partial r$, respectively (Hager & Clayton, 1989; Panasyuk et al., 1996). $\bar{\rho}$ is the layer mean ($l = 0$) density. The kernel A_l comprises both u_1 and u_3, since those are the two terms in the matrix solution to the governing equations which affect surface topography, by directly exerting stress on the surface boundary (u_1), and by changing the gravitational potential at the surface (u_3).

The functional forms of calculated sensitivity kernels depend on chosen radial viscosity profiles and boundary conditions (e.g., free-slip or rigid; Parsons & Daly, 1983). Figure 5a and e show examples of sensitivity kernels generated for water- ($\rho_w = 1030$ kg /m^3), and air-loaded ($\rho_w = 1$ kg /m^3) topography, with free-slip conditions imposed on both surface and lower boundaries. We investigate alternative slip boundary conditions for each surface later in the text. The kernels were generated using the radial viscosity profile shown in Figure 3c. Values of the other parameters used to generate these kernels are stated in Table 1. We limit our investigation to $l \leq 50$, which corresponds to a horizontal wavelength λ of $\approx$ 792 km at Earth's surface. Calculated present-day water- and air-loaded surface deflections, and their statistical properties, are shown in Figure 5b–d and f–h. A comparison of calculated power spectra, expected surface deflection from Kaula's rule (Equation 14), and spectra generated from observed residual ocean age-depth measurements is also included (Kaula, 1963; Hoggard et al., 2016; Holdt et al., 2022). In later sections we explore consequences of choosing different radial viscosity profiles for calculated kernels and thence surface deflections. We call this water-loaded analytical solution for surface deflection 'Model 2' (see Table 2). It represents the closest possible analytical solution for surface deflection predicted numerically by Model 1 explored in this work.

4 Spatial and Spectral Comparison of Model Predictions

We wish to quantify impacts of modelling assumptions and approaches, used to solve the equations of motion, on predicted surface deflections. Thus we compare calculated surface deflections (both numeric and analytical) using the following three metrics.

4.1 Euclidean Comparisons of Amplitudes

First, we calculate root-mean-squared difference, χ, between predicted surface deflections in the spatial domain,

$$\chi = \sqrt{\frac{1}{N}\sum_{n=1}^{N} w_\phi \left(h_n^a - h_n^b\right)^2}, \tag{19}$$

where h_n^a and h_n^b are predicted surface deflections from the two models being compared. N = number of points in the $1{\times}1^\circ$ gridded maps being compared (e.g., Figure 5b; N = 65341). The prefactor w_ϕ is proportional to $\cos\phi$, where ϕ is latitude, and is included to correct biases in cell size with latitude; mean $w_\phi = 1$. This metric is closely associated with the mean vertical distance (L^2-norm distance) between predicted and reference surfaces, i.e., $\Delta\bar{h} = 1/N\sum_{n=1}^{N} w_\phi |h_n^a - h_n^b|$. These metrics are sensitive to differences in amplitudes and locations of surface deflections.

4.2 Spectral Correlation Coefficients

Second, we use `pyshtools v4.10` to compute correlation coefficients, r_l, between predicted surface deflections in the spectral domain (Wieczorek & Meschede, 2018). Correlation coefficients as a function of degree l, adapted from Forte (2007), are calculated such that

$$r_l = \frac{\sum f_1^* f_2}{\sqrt{\sum f_1^* f_1}\sqrt{\sum f_2^* f_2}}, \quad \text{where} \quad \sum = \sum_{m=-l}^{+l}, \tag{20}$$

f_1 and f_2 are the spherical harmonic coefficients of the two fields (i.e., surface deflections) being compared, which vary as a function of m and l; $f = f_l^m$. * indicates complex conjugation (see also Becker & Boschi, 2002; O'Connell, 1971). This metric is a function of degree l, i.e. $r_l = r(l)$, and is sensitive to the difference between predicted and reference surface deflection signals in the frequency domain, but not to their amplitudes. To summarize spectral similarity between models concisely, we later refer to the mean value of r_l over every degree (0–50), as $\bar{r_l}$. We refer to the standard deviation of r_l across degrees as s_r.

4.3 Comparing Calculated Power Spectra

Lastly, to estimate closeness of fit between power spectra of surface deflections predicted in this study and independent estimates, we calculate

$$\chi_p = \sqrt{\frac{1}{L}\sum_{l=1}^{L}\left(\log_{10}P_l - \log_{10}P_l^K\right)^2} + \sqrt{\frac{1}{L}\sum_{l=1}^{L}\left(\log_{10}P_l - \log_{10}P_l^H\right)^2}, \tag{21}$$

where L = number of spherical harmonic degrees being compared ($L = 50$). P_l = power of predicted surface deflections generated in this study at degrees $1 \leq l \leq L$ (Equation 13). P_l^K = power of surface deflections estimated using Kaula's law (assuming Z =

12 mGal km^{-1}; Equation 14). P_l^H = power of residual oceanic age-depth measurements from Holdt et al. (2022).

5 Model Parameterizations and Comparison of Predictions

The models examined in this paper are summarised in Table 2. In terms of assumptions tested there are two families of models, those with viscosity independent of temperature (Models 1–10), and those with temperature-dependent viscosity (Models 11–20). The two approaches used to solve the equations of motion are annotated 'Numerical' and 'Analytical' in Table 2, which refers to solutions from the TERRA and propagator matrix code, respectively. Viscosities and densities calculated using TERRA were used as input for the propagator matrix code and thus used to generate analytical estimates of surface deflection. Since analytical solutions are obtained by spherical harmonic expansion, surface deflections from TERRA were fit using spherical harmonics before predicted deflections were compared (annotated 'Mixed' in Table 2; Section 3.2). We compare predicted deflections that arise from flow across entire model domains, i.e., from the CMB to the surface. We make no lithospheric corrections, unless explicitly stated. Thus, amplitudes of calculated surface deflections are not likely to represent actual residual topography. However, it simplifies like-for-like comparison of models, and comparisons to increasingly complex models. Comparisons of surface deflections predicted by these models are discussed in the following sections, with summary statistics given in Table 3.

5.1 Models 1–10: Viscosity Independent of Temperature

Models 1–10 show results generated when viscosity is independent of temperature. We first compare solutions generated from (reference) numerical and analytical models designed to be as similar as possible (Models 1 and 2). We then generate increasingly complex models—incorporating radial gravitation, gravitational potential energy, removal of shallow structure, and variable surface and CMB slip conditions—and compare predicted surface deflections to the reference models.

Reference Models 1–2

Models 1 and 2 are the simplest models explored in this paper. They were designed to be as similar as possible, with a view to quantifying differences and similarities arising solely from the choice of methodology (numerical or analytical) used to solve equations of motion and to calculate surface deflections. Viscosity is independent of temperature in these models.

Figure 2 shows calculated densities that arise from the numerical solutions (Model 1). This figure shows the plate motion history from Merdith et al. (2021) used to produce this (and subsequent) TERRA output (See Section 2.1). The maps and histograms show evolution (100 to 0 Ma) of calculated densities at the model's surface and within its 'asthenosphere' in response to flow. This model was parameterized with the radial viscosity shown in Figure 3c; radial viscosity used in other geodynamic studies are shown alongside for comparison (Ghelichkhan et al., 2021; Mitrovica & Forte, 2004; Steinberger & Calderwood, 2006). The impact of varying viscosity on numerical solutions is explored later in the paper. Figure 3a shows resultant surface radial stress predicted by this model at full (numerical) resolution. Figure 3d–e show the results from fitting radial stresses generated by Model 1a with a global spherical harmonic interpolation up to maximum degree $l = 50$, i.e., minimum wavelength of ≈ 800 km (Section 3.2). The resultant power spectrum in terms of total power at each degree is shown in Figure 3f. It is approximately

Table 2. Summary of mantle convection simulations. Column labeled 'Method' indicates surface deflections calculated using either '*Numerical*' (i.e., from surface normal stresses calculated using TERRA) or '*Analytical*' (i.e., propagator matrix) approaches; '*Mixed*' indicates spherical harmonic fitting of surface stresses calculated using numerical code, enabling comparison with solutions to propagator matrix code. $\eta(r)$ indicates models with radial viscosity, independent of temperature (Models 1–10). $\eta(r, T)$ indicates models with temperature-dependent (therefore laterally-varying) viscosity (Models 11–20); note that analytical Models 12–20 incorporate radial viscosity calculated using mean radial viscosity from Model 11a. †indicates with respect to Model 12. See Table 2, Section 5 and figures referred to in column 5 for details.

Model	Method	Viscosity	Parameterizations	Figures
1a	Numerical	$\eta(r)$	Full resolution numerical model	2–4
1b	Mixed	$\eta(r)$	Spherical harmonic fit to 1a	2–4, 6
2	Analytical	$\eta(r)$	Propagator matrix solutions	5–6
3	Analytical	$\eta(r)$	Radial gravitation, $g(r)$	7
4	Analytical	$\eta(r)$	Gravitational potential terms	8
5	Analytical	$\eta(r)$	Removing upper 50 km of mantle	9a-d
6	Analytical	$\eta(r)$	Removing upper 100 km of mantle	9e-h
7	Analytical	$\eta(r)$	Removing upper 200 km of mantle	9i-l
8	Analytical	$\eta(r)$	Rigid surface, free CMB	10a-d
9	Analytical	$\eta(r)$	Free surface, rigid CMB	10e-h
10	Analytical	$\eta(r)$	Rigid surface, rigid CMB	10i-l
11a	Numerical	$\eta(r, T)$	Full resolution numerical model	11–13, 16a-c
11b	Mixed	$\eta(r, T)$	Spherical harmonic fit to 11a	11–13, 15, 16d-g
12	Analytical	$\eta(r)$	Mean radial $\eta(r, T)$ from Model 11a	14–16h-k
13	Analytical	$\eta(r)$	Decrease† radial upper mantle η	17a-d
14	Analytical	$\eta(r)$	Increase† radial upper mantle η	17e-h
15	Analytical	$\eta(r)$	Increase† radial upper mantle η	17i-l
16	Analytical	$\eta(r)$	Constant radial η	17m-p
17	Analytical	$\eta(r)$	Upper mantle densities $\times 2^{\dagger}$	18a-c
18	Analytical	$\eta(r)$	Upper mantle densities $\times 1/2^{\dagger}$	18d-f
19	Analytical	$\eta(r)$	Lower mantle densities $\times 2^{\dagger}$	18g-i
20	Analytical	$\eta(r)$	Lower mantle densities $\times 1/2^{\dagger}$	18j-l

characterized by red noise, where (aside from the lack of structure at degree 0), amplitudes of stress variations decrease steadily with increasing spherical harmonic degree (i.e., decreasing wavelength).

Surface deflections calculated by converting stress into dynamic topography using Equation 11, assuming water-loading, are shown in Figure 4a (Model 1a: full numerical resolution). Spherical harmonic interpolation up to $l = 50$ (Model 1b) is shown in panel b, the histograms in panels c and d summarise results. Resultant spectral power is compared to spectra generated using Kaula's rule (Equations 13 and 14) and residuals from ocean age-depth anomalies are shown in panel e (see Section 4; Equation 21). Surface deflections calculated assuming air-loading are shown in Figures 4f-j.

Figure 5a–d shows analytical solutions (Model 2) to the equations of motion generated using the propagator matrix approach parameterised to be as similar as possible to (the numerical) Model 1. The sensitivity kernel generated using the radial viscosity shown in Figure 3c and free-slip surface and CMB boundary conditions is shown in panel a. Similar to many previous studies, the kernel indicates that surface deflections will be especially sensitive (across all degrees incorporated, $l \leq 50$) to density anomalies in the upper mantle (Parsons & Daly, 1983; Hager & Clayton, 1989; Ghelichkhan et al., 2021). Modifications to sensitivity kernels and resultant surface deflections as a consequence of choosing alternative boundary conditions and viscosity profiles are explored later in the manuscript. From this point forward we only present water-loaded surface deflections, since they scale linearly with air-loaded results.

Comparisons of surface deflections predicted by Models 1b and 2 are shown in Figure 6. Predicted deflections are visually similar (cf. panels a and b). Absolute differences in amplitudes are greatest close to subduction zones (e.g., in South America and Asia; panel c). Differences are broadly normally distributed and centred on 0 (panel d). Note the comparisons shown in panel d are weighted by the cosine of latitude to avoid latitudinal biases, as described in Section 4.1. Figure 6e shows that the spherical harmonic correlation between numerical (strictly '*Mixed*', i.e., spherical harmonic fit to numerical solution) and analytical solutions is high (close to 1 for all degrees; cf. Forte, 2007). Panel f shows ratios between predictions, which indicates that analytical solutions tend to be damped compared to numerical solutions. This result is emphasised by the histogram shown in panel g, which summarises the ratios between predictions. Adjusting surface deflections from the propagator matrix solutions by a factor of 1.1 brings them in-line with the numerical solutions. In other words, the propagator matrix approach dampens solutions by $\approx 10\%$. We note that power spectral slopes between Model 1b and 2 are similar, however (cf. Figures 4e and 5d). This smoothness of analytic solutions, and subsequent damping of topographic amplitudes, is perhaps surprising, given the fact that they are being compared with numerical models expanded into the spherical harmonic domain to the same maximum degree, $l = 50$. However, the surface stresses used to generate Model 1a have full horizontal resolution (≈ 45 km) across depths, and *only* the surface layer is smoothed by spherical harmonic fitting, to generate Model 1b. Therefore, Model 1b inherently contains some contribution from degrees ≥ 50, in the sense that finer-resolution density structure at depth could affect longer-wavelength flow nearer the surface. In contrast, to generate the analytic solution (Model 2), the density structure of each layer of the model is smoothed by expansion to maximum $l = 50$, *before* integration of their contributions to surface deflection. The analytical solution would provide a better match to stress estimates from numerical models if such estimates were calculated using density structure smoothed to the same maximum l across all depths.

We now have reference models with which we can quantify the consequences of incorporating alternative assumptions for calculated surface deflections. We start by incorporating more complex parameterization of gravitation.

Model 3: Radial Gravitation

Figure 7a shows solutions for the analytical Model 3, which was parameterized in the same way as Model 2 with the addition of radial gravitation (following Hager & Clayton, 1989; Panasyuk et al., 1996, see Equation 17). The solid curve in panel b shows the radial gravity function used to calculate surface deflections. It was generated using the density distribution produced by (the numerical) Model 1a (see Figure 2), using

$$g(r) = \frac{4\pi G}{r^2}\left[\int_{R_{\mathrm{CMB}}}^{r} \bar{\rho}(r')\, r'^2\, \mathrm{d}r'\right] + F_{core} \tag{22}$$

where $\bar{\rho}(r)$ is layer mean density and F is a factor chosen to account for core mass, and such that $g = 9.8$ m s^{-2} at the surface. This formulation is derived from Gauss's law assuming spherically symmetric density, combined with Newton's law of universal gravitation (Turcotte & Schubert, 2002).

The differences between Model 2 (Figure 7c), which assumes constant $g = 10$ m s^{-2} across all radii, and this model (Model 3) are shown in Figure 7d–e. We interpret the broadly hemispherical, uniformly distributed, differences in calculated deflections as a consequence of deviations in g between the two models being greatest in the mid-mantle ($\sim 500 - 2000$ km depth; see panel b). Note that the sensitivity kernel calculated for the viscosity structure used in these models indicates that changing g in this way is likely to impact surface deflections at low degrees $l \lesssim 10$ most, i.e., where the amplitudes of the sensitivity kernel in the mid-mantle are highest (see Figures 3c & 5a). Note that the amplitudes of deviations in predicted surface topography due to radial variations in g are relatively low, at most of the order $\sim 10\%$ of maximum surface deflection amplitudes, for the instantaneous analytical solution (see Table 3). Differences in predicted surface deflection are likely to be larger between Model 2 and a numerical model which was run using $g(r)$ calculated at each time-step, since in that case radially-varying gravitation would affect the mantle flow field across the entire model run time and differences would compound. Without additional numerical tests it is somewhat unclear whether the differences between that model and Model 2 would match the results for Model 3 (as a function of degree). However, the results are consistent with the rule of thumb outlined in Section 7.02.2.5.2 of Ricard (2015), whereby magnitudes of differences incurred by inclusion of full self-gravitation, i.e., $g(\theta, \phi, r)$, decay as a function of spherical harmonic degree, proportionately to $3/(2l + 1)$.

Model 4: Gravitational Potential Field Deflection

Figure 8 compares analytical solutions for the reference Model 2, and a model that incorporates stress perturbations induced by deflections of the gravitational potential field, Model 4. Both of these models assume $g = 10$ m s^{-2} everywhere, even within the deflected surface layer, as was the case for Models 1–2. Following Hager and Clayton (1989) and Panasyuk et al. (1996), when solving for surface deflection using propagator matrices, the effect on flow of perturbation of gravitational potential is included via the u_3 term in Equation 18 (see also Ribe, 2007; Ricard, 2015). TERRA simulations do not include this component in flow calculations (see Section 2–2.1). As expected, differences in surface displacement predictions are much lower than when radial gravitation is incorporated (cf. Figures 7d and 8c); they are of the same order of magnitude as the geoid height anomalies predicted by these models. The mean Euclidean distance between the two predicted surfaces is only $\sim$110 m, and the spherical harmonic correlation is very high across all degrees (see Table 3). Similar to the result for Model 3, the differences are concentrated at low spherical harmonic degree l. Again, this test investigates the effect of the u_3 term on instantaneous solution for surface deflection. It cannot be ruled out from this test that inclusion of the effect of gravitational potential field perturbation would result in greater differences across the entire model run time, although that is unlikely (Zhong et al., 2008).

Models 5–7: Removal of Shallow Structure

Disentangling contributions to Earth's surface topography from asthenospheric convection and the lithosphere is not trivial (see, e.g., Fernandes & Roberts, 2020; Hoggard et al., 2021; Steinberger, 2016; Stephenson et al., 2021). Previous studies that simulate mantle convection have addressed this issue by discarding density anomalies in radial shells shallower than specified depths, before calculating surface stresses (e.g., Spasojevic & Gurnis, 2012; Flament et al., 2013; Molnar et al., 2015). Similarly, analytical approaches have isolated contributions from the convecting mantle by only incorporating information from deep shells (e.g., Colli et al., 2018). This method has the advantage of effectively removing the effect of lithospheric cooling through time from surface deflection estimates. It also avoids the need to incorporate, say, realistic crustal or depleted lithospheric layers within the viscous flow parameterization. However, uncertain oceanic and continental lithospheric thicknesses mean that choosing appropriate cut-off depths is not trivial. Moreover, doing so creates two obvious challenges.

First, if the chosen depth is shallower than the lithosphere-asthenosphere boundary in places, plate and sub-plate contributions to topography will be entangled. Second, discarding deeper layers to ensure that all plate contribution is definitely avoided means that some contributions from asthenospheric flow will be missed. Calculated sensitivity kernels indicate that shallow asthenospheric density anomalies make significant contributions to surface topography (Figure 5). Thus, such a step is unlikely to be desirable if mantle flow models are to be used to understand, say, lithospheric vertical motions, or vice versa (see e.g., Figure 5a, e; Davies et al., 2019; Hoggard et al., 2016). Given the calculated sensitivity kernels, excising layers in the upper few 100 km is likely to result in predictions of surface deflections that are especially fraught at short wavelengths, i.e., high spherical harmonic degree. An alternative approach, which avoids some of these issues, is removal of structure based on appropriately calibrated plate models, or globally-averaged age-dependent density trends (e.g., F. D. Richards et al., 2020, 2023).

To quantify the impact of discarding shallow structure, we examine differences in calculated surface deflection in the spatial and spherical harmonic domains. We present three tests, resulting in Models 5, 6 and 7, where progressively deeper structure is removed from Model 2. Figure 9 shows the results of removing contributions to surface deflection from density anomalies at depths shallower than 50, 100 and 200 km. As expected from examination of surface topographic sensitivity kernels (e.g., Figure 5a, e), removal of these layers results in significantly reduced surface topographic amplitudes. Doing so results in power spectra that more closely align with independent estimates (Figure 9b, f, j). The reduction in differences between amplitudes of calculated and observed spectral power is largely due to the fact that the reference model (i.e., Model 2) overestimates dynamic topographic power across all degrees. We note that power spectral slopes for predicted surface deflection from Model 2 are close to those generated from Kaula's rule, and observed oceanic residual depths (Figure 4 and 5). However, removing shallow structure steepens spectral slopes (i.e., reduces power at high degrees) beyond those expected from theoretical considerations (i.e., Kaula's rule) or observed (i.e., from oceanic residual depths), akin to results from other work that excised shallow structure (e.g., Flament et al., 2013; Moucha et al., 2008; Steinberger, 2007). This result is emphasized by the slope of calculated spectral coherence, r_l, between deflections with and without shallow structure removed (Figure 9d, h, l). While degree 1 and 2 structure remains coherent, coherence across degrees $\gtrsim$ 20 decreases from $\sim$ 0.9 to as low as 0.5, which are the largest discrepancies between any models examined in this study.

Models 8–10: Adjusted Slip Boundary Conditions

Up to now, we have only considered instantaneous analytical and numerical solutions for surface deflection where both the surface and CMB have free-slip conditions imposed (i.e., vertical component of flow velocity $\mathbf{u_r} = 0$, horizontal components are allowed to freely vary). No gradient/Neumann constraint (e.g., on $\partial \mathbf{u}/\partial z$) is imposed. This condition is generally deemed appropriate for the surface of the convecting mantle, and CMB, since at both boundaries, cohesion within convecting mantle is thought to be much stronger than adhesion to the boundary. Analytical solutions for sensitivity kernels for propagator matrices also exist for rigid boundaries, i.e., no-slip Dirichlet conditions, where horizontal components of $\mathbf{u} = 0$, which may be more appropriate when the Earth's lithosphere is implicitly included in mantle convection models, as is the case here (Parsons & Daly, 1983; Thoraval & Richards, 1997). Therefore, we test the effect on predicted surface deflections of changing the surface boundary condition to no-slip. Although there is little reason to believe the adhesion of the CMB would be strong, we also test a rigid CMB for completeness. The numerical models themselves are driven by a quasi-rigid condition, whereby flow is driven by estimates of real plate velocities from (Merdith et al., 2021), and so the surface layers behave as a series of rigid, laterally mobile plates rather than a single rigid shell. This approach may be appropriate for driving near-surface (lithospheric) flow throughout the main model run time, but it less clear whether no- or free-slip boundary conditions are most appropriate for calculating instantaneous dynamic topography (see, e.g., Forte & Peltier, 1994; Thoraval & Richards, 1997).

Figure 10a, e and i show predicted sensitivity kernels as a function of depth and degree (l), for no-slip/free-slip, free-slip/no-slip and no-slip/no-slip boundaries respectively, where the first condition is the surface slip condition, and the second the CMB slip condition. Differences to the original sensitivity kernel for Model 2 (Figure 5a) are shown in panels c, g and k. Those panels demonstrate that when the surface boundary condition is rigid, there is decreased sensitivity to short wavelength shallow structure, and increased sensitivity to long-wavelength (low degree) structure across all depths. Figure 10d, h and l reveal that induced misfit in the spatial domain is impacted to a greater degree than in tests of gravitation (Models 3 & 4), but not necessarily more severely than for removal of, say the upper 200 km of density structure from surface deflection calculations. Spectral correlation is most severely impacted when both surface and CMB boundaries are rigid (Model 7; see Table 3).

5.2 Reference Models 11–12: Temperature-Dependent Viscosity

In this section, we investigate the impact of including the temperature dependence of viscosity, $\eta(r, T)$, on predicted global mantle flow in numerical models, and on subsequent estimates of surface deflection. We do so by first presenting results for the numerical Model 11, which is identical to Model 1 in terms of all boundary conditions, initialization, and physical parameters, except for the fact that viscosity depends on temperature in the manner described by Equation 7. The analytical propagator matrix approaches used in this study require that viscosity varies only as a function of radius. In other words, they cannot incorporate temperature-dependent viscosity directly. So, instead we insert layer mean viscosity from the present-day 3D temperature-dependent viscosity structure predicted by numerical models (Figure 11), and use it to generate the analytical Model 12. The role of upper and lower mantle viscosity and density anomalies in determining surface deflections are then examined. For tests resulting in Models 3–10, analytical instantaneous solutions for surface deflection with adjusted parameters and boundary conditions were simply compared with Model 2, and no new numerical models were generated using TERRA. In contrast, this section corresponds to a new model generated using TERRA, where temperature dependence of viscosity affected global mantle flow across the entire run time (Model 11).

Figure 11 shows maps of calculated viscosity in the upper and lower mantle for Model 11. Results, at full horizontal resolution, from the numerical Model 11a are shown in panels a, e, i, m. A slice through this three-dimensional viscosity structure is shown in Figure 1c. Spherical harmonic interpolation of these results, up to maximum degree l = 50, are shown in panels d, h, l and p (Model 11b). Viscosity variation shown in these maps is expressed as percentage deviation from layer mean. Histograms summarising the distribution of viscosity in Model 11a are also shown, alongside radial mean values and extrema. Figure 12 shows the spatio-temporal (100 to 0 Ma) evolution of calculated densities in Model 11a at the surface of the model and within its 'asthenosphere', alongside summary statistics. Density anomalies are more localised ('sharper') than in Model 1, which is unsurprising since temperature-dependent viscosity provides stronger mechanical constrasts between cooler subducting regions and surrounding asthenosphere, when compared to models that do not include temperature-dependent viscosity (cf. Figure 2 Zhong et al., 2000).

Figure 13a-b shows calculated radial normal stresses from Model 11a and their spherical harmonic representation (Model 11b). Summary statistics and calculated power spectra are shown in panels c-d. Panels f-g show calculated water-loaded surface deflections for the full resolution numerical model and for the 'Mixed' spherical harmonic representation (Equation 11). Panels h-j show summary statistics and power spectra as a function of degree, alongside Kaula's rule and an independent estimate of sub-plate support from residual oceanic age-depth measurements (see Section 4). Figure 14 shows surface deflections calculated analytically (Model 12) using layer-mean (radial) viscosity shown in Figure 11c, which was extracted from the numerical Model 11a. Panels a-d show the resultant sensitivity kernel, water-loaded deflections and summary statistics (cf. Figure 5a-d). Air-loaded predictions are shown for Model 12 for reference, in Figure 14e–h, but not included in any summary statistics or future figures, for consistency with previous sections.

Figure 15 compares predictions from the numerical (Model 11b) and analytical (Model 12) schemes incorporating temperature-dependent viscosity, as discussed in the preceding sections. Similar to the results obtained for models without temperature-dependent viscosity (Figure 6), surface deflections calculated using the analytical approach are damped relative to numerical solutions (in their spherical harmonic form; see Figure 15f). The best fit amplification factor to align propagator matrix and numerical solutions is 1.24 (24%), larger than the adjustment required to align reference Models 1b and 2 (1.1; 10%). Similar to our interpretation of those previous results, we attribute this discrepancy to smoothing inherent to the propagator matrix methodology. The effect is amplified compared with comparison between Models 1b and 2 because of increased short wavelength structure in Model 11 (as discussed above, see Section 5.1; Zhong et al., 2000). Nonetheless, spherical harmonic correlation, r_l, is > 0.75 for all degrees examined ($l \leq 50$), and > 0.85 for most degrees. Cell-to-cell differences in surface deflections are broadly normally distributed and centred on zero (Figure 15d).

Figure 16 shows comparisons between surface deflections predicted by models with and without temperature-dependent viscosity. Panels a-c compare the full resolution numerical solutions (Models 1a and 11a), including summary statistics. Panels d-g compare spherical harmonic interpolations of the numerical solutions (Models 1b and 11b). Finally, panels h-k compare propagator matrix solutions for Models 2 and 12, where Model 12 incorporates radial (layer-mean) viscosity extracted from solutions to the numerical Model 11a (incorporating temperature-dependent viscosity; Figure 11c). Unsurprisingly, discrepancy is greatest between the full resolution models. However, discrepancies in cell-to-cell deflections are again, broadly normally distributed and centred on zero, clustering along the 1:1 relationship with χ = 1.51 (panels b-c; see Table 3). Similar results are obtained for both comparisons of spherical harmonically fitted results, and analytical results, albeit with less discrepancy, which is emphasised by tighter normal distributions and lower χ values. Correlation coefficients are > 0.75 for nearly all degrees for both comparisons.

5.3 Upper and Lower Mantle Viscosity and Density Anomalies

Models 13–16: Adjusted Sub-Plate Viscosity

The radial distribution of viscosity, but not its absolute value, plays a crucial role in determining sensitivity of instantaneous solutions for surface deflections to density (and thermal) anomalies in the mantle (e.g., Parsons & Daly, 1983; Hager, 1984). Consequently, we performed a suite of analytical tests in which distributions of upper and lower mantle (radial) temperature-dependent viscosity was varied within propagator matrix solutions. The resulting impact on calculated surface deflections was quantified by comparison with results generated using reference Model 12 (Figure 14). The radial component of viscosity, $\eta(r)$, in each test was modified from that used to generate Model 12 (see solid black curve in Figure 17). Figure 17a-d show results generated by decreasing upper mantle viscosity by an order of magnitude. Panels e–n show the results of decreasing upper mantle viscosity by an order of magnitude. Panels j–p show the impact of using increasingly simple radial viscosity. Calculated sensitivity kernels for the adjusted viscosity profiles demonstrate that decreasing upper mantle viscosity (relative to the reference case) further reduces sensitivity of surface deflections to long-wavelength density structure, especially in the lower mantle (Figure 17b, f, j, n). However, in general, results are similar to the reference model even when $\eta(r)$ is drastically varied, with average χ misfit incurred of only 0.17–0.38 km, and $r_l > 0.97$ across all degrees for all tests. This result emphasizes the fact that viscosity only exerts a relatively minor control on sensitivity of surface deflection to mantle density structure, in terms of instantaneous flow (Table 3, see, e.g., Ghosh et al., 2010; Moucha et al., 2007; Lu et al., 2020).

Models 17–20: Adjusted Density Anomalies

Figure 18 shows results from tests in which the amplitudes of density anomalies in the upper and lower mantle were systematically increased or decreased. Similar to the tests shown in Figure 17, densities are amplified relative to Model 12. Radial viscosity is constant for each of these tests (black curve in Figure 18a; i.e., same as that used to generate Model 12). The reference sensitivity kernel for Model 12 is shown in Figure 14a. Figure 18a-d and g-i show results generated by amplifying respective upper and lower mantle densities by a factor of 2. Panels d-f and j-l show results when amplitudes of density anomalies are decreased by 1/2. Table 3 summarizes the differences incurred to Model 12; although spherical harmonic correlation between models is approximately as good as for the radial viscosity tests (Models 13–16), that is to be expected since we do not vary locations of density anomalies here, only their amplitudes, and r_l is insensitive to amplitudes of the two results being compared. Significant is the fact that mean vertical differences between Models 17–20 and 12 (i.e., χ and $\Delta\bar{h}$) are higher than those calculated for Models 13–16. These results emphasize the relative sensitivity of surface deflections to upper mantle density anomalies, and that even quite large uncertainties in lower mantle density anomalies have relatively little impact on surface deflections. Our conclusion is that accurately constraining and accounting for upper-mantle density structure is of primary concern when estimating surface deflection, and dynamic topography, from mantle convection simulations.

Table 3. Inter-model comparison of predicted surface deflections. Models being compared are summarised in Table 2. Metrics: root-mean-squared difference (χ, km), mean Euclidean (L^2-norm) difference in predicted deflection ($\Delta\bar{h}$, km), and mean spherical harmonic correlation between models ($\bar{r}_l$). Standard deviation of r_l distribution across degrees (s_r) is also stated: note that $r_l \leq 1$. All spherical harmonic representations of output from numerical code and generated by the propagator matrix code are expanded up to maximum degree, $l = 50$. See body text, figures referred to in column 6, and Table 2 for details.

Models	χ	$\Delta\bar{h}$	$\bar{r}_l$	s_r	Figures
1b & 2	0.95	0.69	0.97	0.02	5–6
2 & 3	0.57	0.47	0.99	4×10^{-4}	7
2 & 4	0.13	0.11	0.99	2×10^{-5}	8
2 & 5	0.67	0.48	0.93	0.04	9a-d
2 & 6	1.03	0.74	0.87	0.06	9e-h
2 & 7	1.57	1.12	0.63	0.15	9i-l
2 & 8	1.26	1.04	0.99	1×10^{-3}	10a-d
2 & 9	1.09	0.97	0.99	0.04	10e-h
2 & 10	1.00	0.74	0.96	0.28	10i-l
1a & 11a	1.51	1.04	—	—	11–13, 16a-c
1b & 11b	1.44	0.98	0.79	0.26	11–13, 16d-g
11b & 12	1.20	0.80	0.95	0.02	15
2 & 12	0.92	0.64	0.85	0.27	14, 16h-k
12 & 13	0.31	0.20	0.99	9×10^{-3}	17a-d
12 & 14	0.17	0.10	0.99	3×10^{-3}	17e-h
12 & 15	0.32	0.20	0.98	0.01	17i-l
12 & 16	0.38	0.23	0.98	0.01	17m-p
12 & 17	0.97	0.64	0.98	7×10^{-3}	18a-c
12 & 18	0.48	0.32	0.98	6×10^{-3}	18d-f
12 & 19	0.43	0.29	0.99	3×10^{-3}	18g-i
12 & 20	0.22	0.14	0.99	1×10^{-3}	18j-l

6 Discussion

An important goal is to understand how geological and geomorphological observations at (or close to) Earth's surface can be used to determine the history of mantle convection during, say, the last 100 million years. Various observations now exist that can be used to constrain mantle convection (e.g., Hoggard et al., 2021; Holdt et al., 2022; Davies et al., 2023, see Section 1.1). An obvious approach is to use them to test existing simulations of mantle convection. We start by comparing numerical and analytical predictions of instantaneous surface deflections generated by mantle convection simulations.

Numerical approaches to solving the equations of motion are very flexible, and can incorporate a variety of assumptions and parameterizations that are not amenable to analytical attack (e.g., temperature-dependent viscosity; Section 2.1). However, ensuring accuracy and stability means that the computational burden is often considerable and hence systematic exploration of parameter space remains challenging. In contrast, analytical approaches can yield calculated surface deflections that are (mathematically) accurate for relatively little computational cost, and may include features such as radial gravitation with much less computational cost (Section 3.3). Consequently, it is straightforward to explore parameter space, examine benchmarks, reproduce results, and investigate sensitivity of solutions to different parameterizations. There are, however, important limitations to consider. First, analytical solutions are only known to exist in the spherical domain for fluid bodies with radial viscosity (i.e., no lateral variability in viscosity). Second, generating solutions in the spherical harmonic domain places practical limits on spatial resolution of solutions. Consider that the number of spherical harmonic coefficients per degree $= 2l + 1$, where l is degree, so for a given maximum degree L, there are $(L+1)^2$ coefficients derived in total. For our results, where $L = 50$, there are therefore $2,601$ coefficients altogether, for each model. Consider also that spatial resolution increases approximately with the reciprocal of l (see Section 3.2). Incorporating full resolution (60 km at the surface) output from the numerical models used in this study would therefore require $L \approx 880$, with $776,161$ coefficients. Clearly, computational constraints limit our investigation to $l \lesssim 50$. Furthermore, observational constraints on mantle-related surface deflection are unlikely to be finer than the flexural wavelength of the overlying lithosphere, $l \approx 50$ (e.g., Holdt et al., 2022). With these limitations in mind, we compared surface deflections predicted using different approaches at the same resolution (up to $l = 50$; Sections 2.1 and 3.3). We then quantified the impact of incorporating increasingly complex physics into models used to predict surface deflections (Section 5; Tables 2–3).

First, we simply compared predictions from numerical and analytical approaches parameterised to be as similar as possible. In this test, the models were purposefully simple: viscosity is radial, models are incompressible, and do not include self-gravitation, or radial variation in g. Numerical solutions were transformed into the frequency (spherical harmonic) domain so that they could be compared with analytical solutions, and so that power spectra could be directly compared at appropriate scales. The results show that, for as-similar-as-possible parameterizations, amplitudes of analytical solutions are $\approx 10\%$ lower than numerical solutions (Figure 6). If the numerical model incorporates temperature-dependent viscosity, this discrepancy increases to 25% (Figure 15). We interpret these results in two ways. First, once armed with viscosity and density fields, numerical and analytical approaches broadly yield similar estimates of surface deflections. Second, the relatively damped analytical solutions are a consequence of smoothing steps in the propagator matrix approach.

The similarity of results indicates that the relatively low-cost propagator matrix approach can be used to explore consequences of including additional model complexity. A systematic sweep of parameters, including radial gravitation (Figure 7) and gravitational potential field effects (Figure 8) indicates that their effects on surface deflection are relatively modest. A useful rule of thumb is that self-gravitation perturbs instantaneous surface deflections by $O(1\text{–}10)\%$ when compared to models with constant gravitational acceleration, and even less difference is observed at high degree (e.g., Ricard, 2015, their Section 7.02.2.5.2). Full 3-D self-gravitation may affect the flow field over time, but modelling such effects numerically is currently challenging. Incorporating the effect of deflections of gravitational potential field on flow has a modest impact on amplitudes of surface deflections at degrees 1–2, but overall it contributes even less than radial variation in g to surface deflections across the scales of interest (Figure 7). In contrast, removing shallow structure has a very large impact on predictions. It modifies amplitudes of surface deflections, locations of uplift and subsidence, and degrees over which they are resolved, and hence it modifies power spectral scalings (Table 3, Figure 9). In contrast, viscosity variations do not have much impact on surface deflections compared to other effects, even if they are decreased or increased by an order of magnitude (Figure 17). The distribution of density anomalies, especially in the upper mantle, does however play a very significant role in deflecting the surface (Figure 18). Calculated summary statistics suggest that systematically increasing or decreasing mantle densities significantly impacts amplitudes of surface deflections. Conversely, spherical harmonic correlation coefficients between models with and without density anomalies were largely unaffected, as locations of anomalies were not varied.

These results emphasise the importance of considering sensitivities of surface deflections to the location and scale of flow in the mantle. Taking inspiration from Hager and O'Connell (1981) and Parsons and Daly (1983), we calculate the net contributions from density anomaly structure to surface deflections, as a function of radius, latitude and longitude across all spherical harmonic degrees considered (i.e., $l = 1$ to 50). Contributions to surface deflections from densities at particular radii r, across all spherical harmonic degrees and orders, for each latitude and longitude, $h_e(\theta, \phi)$, are calculated such that

$$h_e(\theta, \phi, r) = \sum_{l=1}^{L} \sum_{m=-l}^{m=l} \left[Y_{lm}(\theta, \phi) \cdot \delta\rho_{lm}(r) \cdot A_l(r) \cdot \Delta r \right], \tag{23}$$

where Δr is the layer spacing $\approx$ 45 km, Y_{lm}, $\delta\rho_{lm}$ and A_l are spherical harmonic coefficients, density anomalies and sensitivities as defined in Section 3.3. Contributions from specific locations and depths to surface deflections as a function of latitude and longitude are shown in Figure 19 for Model 12, for all degrees $1 \leq l \leq 50$. Results for lower maximum l are shown in Supporting Information. Panels a-d show slices through effective density in the upper (at 45, 135, 360 km) and lower mantle (1445 km). A 180° cross-section showing effective densities from the core-mantle-boundary to the surface beneath the Pacific to the Indian Ocean encompassing South America and southern Africa (the same transect as shown in Figure 1) is shown in panel e. Calculated total net surface deflections along the transect from Model 12, which incorporates temperature-dependent viscosity, and Model 2, which does not, are both shown in panel f. A Cartesian version of the cross-section with the same horizontal scale is shown in panel g. The adjacent panel h shows mean density anomaly amplitudes as a function of radius for Model 12 (dashed grey curve), alongside mean effective densities for the two models, and for the case where Model 12 was only expanded to maximum $l = 10$. These panels again emphasize the contribution of density anomalies in the upper mantle to surface displacements, and the risks associated with discarding shallow structure when predicting dynamic topography. In other words, instantaneous surface deflections are most sensitive to the distribution of density anomalies in the upper mantle.

Encouragingly, surface deflections are sensitive to simulated mantle convection patterns and resulting density distributions, and appear to be relatively insensitive to the methodologies used to calculate deflections when parameterizations (assumptions) are consistent. The next step is to make use of independent geological observations to identify optimal simulations and associated parameterizations. In this study, we compared power spectra (strictly, spherical harmonic coefficients) from calculated surface deflections and oceanic age-depth residuals (e.g., Figure 4; Holdt et al., 2022). The simulations examined have spectral slopes consistent with observations if the entire modelling domain (core-mantle boundary to surface) is incorporated, however amplitudes are overpredicted by 1–2 orders of magnitude. The uppermost 100–450 km of the mantle is often excised in geodynamic studies prior to estimating surface deflections. We demonstrate that removing the upper 200 km can generate surface deflections with amplitudes that more closely match observations, especially at spherical harmonic degrees > 10. However, the spectral slopes of predicted deflections are redder than for the oceanic residuals, which implies that a different approach to removing the contribution of upper mantle/lithospheric structure is required. An obvious avenue for future work is to incorporate information about lithospheric structure into these predictions.

The body of geologic and geomorphologic observations that could be used to test the predicted history of surface deflections from mantle convection simulations has grown substantially in the last decade (e.g., uplift and subsidence histories; Section 1.1; see, e.g., Hoggard et al., 2021). A suite of other geological and geophysical observables are also predicted by, or can be derived from, such simulations (e.g., mantle temperatures, heat flux, geoid, seismic velocities, true polar wander). Using them alongside histories of surface deflections to identify optimal simulations is an obvious avenue for future work (e.g., Ball et al., 2021; Lau et al., 2017; Panton et al., 2023; F. D. Richards et al., 2023). Using such data and the methodologies explored in this paper may be a fruitful way of identifying optimal simulations from the considerable inventory that already exists.

7 Conclusions

This study is concerned with quantifying sensitivities and uncertainties of Earth's surface deflections that arise in simulations of mantle convection. Calculated sensitivities of instantaneous deflection of Earth's surface to mantle density structure emphasise the importance of accurate mapping of the upper mantle. Surface deflections are somewhat sensitive to the distribution of viscosity throughout the mantle, but especially to the locations and scales of density anomalies in the upper mantle. The largest discrepancies between predicted deflections seen in this study are generated when upper mantle structure is excised or altered. Doing so changes both the amplitude and distribution of calculated deflections, modifying their power spectral slopes. These results emphasise the importance of incorporating accurate models of lithospheric structure into calculation of sub-plate support of topography, and also the need to accurately determine plate contributions to topography. In contrast, the choice of methodology to estimate surface deflections—analytical or numerical—or boundary conditions are relatively small sources of uncertainty. Similarly, assumed gravitational profiles and temperature dependence of viscosity are relatively minor contributors to uncertainty given reasonable, Earth-like, parameterizations. Nonetheless, these parameterizations may impact surface deflections through their role in determining how upper mantle flow evolves through geologic time. A fruitful next step could be to use the approaches developed in this paper, in combination with careful isolation of plate cooling signatures from surface deflection predictions, to test mantle convection simulations using the existing and growing body of geologic, geomorphologic and geophysical observations.

Open Research Section

TERRA models are archived [here]. The propagator matrix code is archived [here]. Parameterization files are archived [here]. [TO ED: this section will be completed upon final submission, when confirmation of the precise models published is obtained after review.]

Acknowledgments

We thank A. Biggin, H. Brown, C. Davies, A. Ferreira, M. Holdt, P. Japsen, P. Koelemeijer, F. McNab, R. Myhill and J. Ward for helpful discussion. C.O., J.P. and V.M.F. were supported by NERC Grant NE/T01684/1.

References

Al-Hajri, Y., White, N., & Fishwick, S. (2009). Scales of transient convective support beneath Africa. *Geology*, *37*(10), 883–886. doi: 10.1130/G25703A.1

Audet, P. (2014). Toward mapping the effective elastic thickness of planetary lithospheres from a spherical wavelet analysis of gravity and topography. *Physics of the Earth and Planetary Interiors*, *226*, 48–82. Retrieved from `http://dx.doi.org/10.1016/j.pepi.2013.09.011` doi: 10.1016/j.pepi.2013.09.011

Ball, P. W., Duvernay, T., & Davies, D. R. (2022). A coupled geochemical-geodynamic approach for predicting mantle melting in space and time. *Geochemistry, Geophysics, Geosystems*, *23*, 1–31. doi: 10.1029/2022gc010421

Ball, P. W., White, N. J., Maclennan, J., & Stephenson, S. N. (2021). Global Influence of Mantle Temperature and Plate Thickness on Intraplate Volcanism. *Nature Communications*, *12*(2045), 1–13. Retrieved from `http://dx.doi.org/10.1038/s41467-021-22323-9` doi: 10.1038/s41467-021-22323-9

Bangerth, W., Dannberg, J., Fraters, M., Gassmoeller, R., Glerum, A., Heister, T., … Naliboff, J. (2023). ASPECT v2.5.0 [Computer software manual]. Retrieved 2023-08-04, from `https://zenodo.org/record/3924604` doi: 10.5281/zenodo.8200213

Baumgardner, J. R. (1985). Three-dimensional treatment of convective flow in the earth's mantle. *Journal of Statistical Physics*, *39*(5-6), 501–511. doi: 10.1007/BF01008348

Becker, T. W., & Boschi, L. (2002). A comparison of tomographic and geodynamic mantle models. *Geochemistry, Geophysics, Geosystems*, *3*(1), 1–48. doi: 10.1029/2001GC000168

Biggin, A. J., Steinberger, B., Aubert, J., Suttie, N., Holme, R., Torsvik, T. H., … Van Hinsbergen, D. J. (2012). Possible links between long-term geomagnetic variations and whole-mantle convection processes. *Nature Geoscience*, *5*(8), 526–533. doi: 10.1038/ngeo1521

Braun, J. (2010). The many surface expressions of mantle dynamics. *Nature Geoscience*, *3*(12), 825–833. doi: 10.1038/ngeo1020

Bunge, H.-P., & Baumgardner, J. R. (1995). Mantle convection modeling on parallel virtual machines. *Computers in Physics*, *9*(2), 207–215. doi: 10.1063/1.168525

Bunge, H.-P., Hagelberg, C. R., & Travis, B. J. (2003). Mantle circulation models with variational data assimilation: inferring past mantle flow and structure from plate motion histories and seismic tomography. *Geophysical Journal International*, *152*, 280–301. doi: 10.1046/j.1365-246X.2003.01823

Bunge, H.-P., Richards, M. A., & Baumgardner, J. R. (2002). Mantle-circulation models with sequential data assimilation: Inferring present-day mantle structure from plate-motion histories. *Philosophical Transactions of the Royal Society A: Mathematical, Physical and Engineering Sciences*, *360*(1800), 2545–2567. doi: 10.1098/rsta.2002.1080

Colli, L., Ghelichkhan, S., & Bunge, H.-P. (2016). On the ratio of dynamic topography and gravity anomalies in a dynamic Earth. *Geophysical Research Letters*, *43*, 2510–2516. doi: 10.1002/2016GL067929

Colli, L., Ghelichkhan, S., Bunge, H.-P., & Oeser, J. (2018). Retrodictions of Mid Paleogene mantle flow and dynamic topography in the Atlantic region from compressible high resolution adjoint mantle convection models: Sensitivity to deep mantle viscosity and tomographic input model. *Gondwana Research*, *53*, 252–272. doi: 10.1016/j.gr.2017.04.027

Corrieu, V., Thoraval, C., & Ricard, Y. (1995). Mantle dynamics and geoid Green functions. *Geophysical Journal International*, *120*(2), 516–523. doi: 10.1111/j.1365-246X.1995.tb01835.x

Craig, C. H., & McKenzie, D. (1987). Surface deformation, gravity and the geoid from a three-dimensional convection model at low Rayleigh numbers. *Earth and Planetary Science Letters*, *83*, 123–136. doi: 10.1016/0012-821X(87)90056-2

Crameri, F., Schmeling, H., Golabek, G. J., Duretz, T., Orendt, R., Buiter, S. J., … Tackley, P. J. (2012). A comparison of numerical surface topography calculations in geodynamic modelling: An evaluation of the 'sticky air' method. *Geophysical Journal International*, *189*(1), 38–54. doi: 10.1111/j.1365-246X.2012.05388.x

Czarnota, K., Hoggard, M. J., White, N., & Winterbourne, J. (2013). Spatial and temporal patterns of Cenozoic dynamic topography around Australia. *Geochemistry, Geophysics, Geosystems*, *14*(3), 634–658. doi: 10.1029/2012GC004392

Davies, D. R., Davies, J. H., Bollada, P. C., Hassan, O., Morgan, K., & Nithiarasu, P. (2013). A hierarchical mesh refinement technique for global 3-D spherical mantle convection modelling. *Geoscientific Model Development*, *6*(4), 1095–1107. doi: 10.5194/gmd-6-1095-2013

Davies, D. R., Ghelichkhan, S., Hoggard, M. J., Valentine, A. P., & Richards, F. D. (2023). Observations and Models of Dynamic Topography: Current Status and Future Directions. In J. Duarte (Ed.), *Dynamics of plate tectonics and mantle convection* (pp. 223–269). Elsevier. doi: 10.1016/B978-0-323-85733-8.00017-2

Davies, D. R., Valentine, A. P., Kramer, S. C., Rawlinson, N., Hoggard, M. J., Eakin, C. M., & Wilson, C. R. (2019). Earth's multi-scale topographic response to global mantle flow. *Nature Geoscience*, *12*, 845–850. Retrieved from `http://dx.doi.org/10.1038/s41561-019-0441-4` doi: 10.1038/s41561-019-0441-4

Fernandes, V. M., & Roberts, G. G. (2020). Cretaceous to Recent net continental uplift from paleobiological data: Insights into sub-plate support. *GSA Bulletin*, *133*, 1–20. doi: 10.1130/b35739.1

Fernandes, V. M., Roberts, G. G., White, N., & Whittaker, A. C. (2019). Continental-Scale Landscape Evolution: A History of North American Topography. *Journal of Geophysical Research: Earth Surface*, *124*, 1–34. doi: 10.1029/2018jf004979

Fichtner, A., Kennett, B. L. N., Igel, H., & Bunge, H.-P. (2009). Full seismic waveform tomography for upper-mantle structure in the Australasian region using adjoint methods. *Geophysical Journal International*, *179*(3), 1703–1725. doi: 10.1111/j.1365-246X.2009.04368.x

Fichtner, A., Trampert, J., Cupillard, P., Saygin, E., Taymaz, T., Capdeville, Y., & Villaseñor, A. (2013). Multiscale full waveform inversion. *Geophysical Journal International*, *194*, 534–556. doi: 10.1093/gji/ggt118

Fichtner, A., & Villaseñor, A. (2015). Crust and upper mantle of the western Mediterranean - Constraints from full-waveform inversion. *Earth and Planetary Science Letters*, *428*, 52–62. Retrieved from `http://dx.doi.org/10.1016/j.epsl.2015.07.038` doi: 10.1016/j.epsl.2015.07.038

Flament, N., Gurnis, M., & Muller, R. D. (2013). A review of observations and models of dynamic topography. *Lithosphere*, *5*(2), 189–210. Retrieved from `https://pubs.geoscienceworld.org/lithosphere/article/5/2/189-210/`

145653 doi: 10.1130/L245.1
Flament, N., Gurnis, M., Müller, R. D., Bower, D. J., & Husson, L. (2015). Influence of subduction history on South American topography. *Earth and Planetary Science Letters*, *430*, 9–18. doi: 10.1016/j.epsl.2015.08.006
Foley, S. F., & Fischer, T. P. (2017). An essential role for continental rifts and lithosphere in the deep carbon cycle. *Nature Geoscience*, *10*(12), 897–902. Retrieved from http://dx.doi.org/10.1038/s41561-017-0002-7 doi: 10.1038/s41561-017-0002-7
Forte, A. M. (2007). Constraints on Seismic Models from Other Disciplines - Implications for Mantle Dynamics and Composition. In B. Romanowicz & A. Dziewonski (Eds.), *Seismology and the structure of the earth* (pp. 805–858). Elsevier B.V. doi: 10.1016/B978-044452748-6.00027-4
Forte, A. M., & Peltier, R. (1991). Viscous Flow Models of Global Geophysical Observables 1. Forward Problems. *Journal of Geophysical Research*, *96*(B12), 20131–20159. doi: 10.1029/91JB01709
Forte, A. M., & Peltier, W. R. (1994). The Kinematics and Dynamics of Poloidal-Toroidal Coupling in Mantle Flow: The Importance of Surface Plates and Lateral Viscosity Variations. *Advances in Geophysics*, *36*, 1–119. doi: 10.1016/S0065-2687(08)60537-3
French, S. W., & Romanowicz, B. (2015). Broad plumes rooted at the base of the Earth's mantle beneath major hotspots. *Nature*, *525*(7567), 95–99. doi: 10.1038/nature14876
Galloway, W. E., Whiteaker, T. L., & Ganey-Curry, P. (2011, jul). History of Cenozoic North American drainage basin evolution, sediment yield, and accumulation in the Gulf of Mexico basin. *Geosphere*, *7*(4), 938–973. Retrieved from http://geosphere.gsapubs.org/cgi/doi/10.1130/GES00647.1 doi: 10.1130/GES00647.1
Gantmacher, F. R. (1959). *The Theory of Matrices.* New York: Chelsea Publishing Company.
Ghelichkhan, S., Bunge, H.-P., & Oeser, J. (2021). Global mantle flow retrodictions for the early Cenozoic using an adjoint method: Evolving dynamic topographies, deep mantle structures, flow trajectories and sublithospheric stresses. *Geophysical Journal International*, *226*(2), 1432–1460. doi: 10.1093/gji/ggab108
Ghosh, A., Becker, T. W., & Zhong, S. J. (2010). Effects of lateral viscosity variations on the geoid. *Geophysical Research Letters*, *37*(1), 2–7. doi: 10.1029/2009GL040426
Glišović, P., & Forte, A. M. (2016). A new back-and-forth iterative method for time-reversed convection modeling: Implications for the Cenozoic evolution of 3-D structure and dynamics of the mantle. *Journal of Geophysical Research: Solid Earth*, *121*(6), 4067–4084. doi: 10.1002/2016JB012841
Gunnell, Y., & Burke, K. (2008). The African Erosion Surface: A Continental-Scale Synthesis of Geomorphology, Tectonics, and Environmental Change over the Past 180 Million Years. *Memoir of the Geological Society of America*, *201*, 1–66. doi: 10.1130/2008.1201
Hager, B. H. (1984). Subducted Slabs and the Geoid: Constraints on Mantle Rheology and Flow. *Journal of Geophysical Research*, *89*(B7), 6003–6015.
Hager, B. H., & Clayton, R. W. (1989). Constraints on the Structure of Mantle Convection Using Seismic Observations, Flow Models, and the Geoid. In W. R. Peltier (Ed.), *Mantle convection: Plate tectonics and global dynamics* (pp. 657–763). New York: Gordon and Breach Science Publishers.
Hager, B. H., Clayton, R. W., Richards, M. A., Comer, R. P., & Dziewonski, A. M. (1985). Lower mantle heterogeneity, dynamic topography and the geoid. *Nature*, *313*, 541–545. doi: 10.1038/314752a0
Hager, B. H., & O'Connell, R. J. (1979). Kinematic Models of Large-Scale Flow in

the Earth's Mantle. *Journal of Geophysical Research*, *84*(B3), 1031–1048.

Hager, B. H., & O'Connell, R. J. (1981). A Simple Global Model of Plate Dynamics and Mantle Convection. *Journal of Geophysical Research*, *86*(B6), 4843–4867. doi: 10.1029/JB086iB06p04843

Hazzard, J. A. N., Richards, F. D., Goes, S. D. B., & Roberts, G. G. (2022). Probabilistic Assessment of Antarctic Thermomechanical Structure: Impacts on Ice Sheet Stability. *EarthArXiv*. doi: 10.31223/X5C35R

Hoggard, M. J., Austermann, J., Randel, C., & Stephenson, S. (2021). Observational Estimates of Dynamic Topography Through Space and Time. In *Mantle convection and surface expressions* (pp. 371–411). AGU. doi: 10.1002/9781119528609.ch15

Hoggard, M. J., White, N., & Al-Attar, D. (2016). Global dynamic topography observations reveal limited influence of large-scale mantle flow. *Nature Geoscience*, *9*(May), 1–8. doi: 10.1038/ngeo2709

Holdt, M. C., White, N. J., Stephenson, S. N., & Conway-Jones, B. W. (2022). Densely Sampled Global Dynamic Topographic Observations and Their Significance. *Journal of Geophysical Research: Solid Earth*, *127*, 1–32.

Jeans, J. H. (1923). The Propagation of Earthquake Waves. *Proceedings of the Royal Society of London A*, *102*(718), 554–574.

Kaula, W. M. (1963). Determination of the Earth's Gravitational Field. *Reviews of Geophysics*, *1*(4), 507–551.

Lambeck, K., Smither, C., & Johnston, P. (1998). Sea-level change, glacial rebound and mantle viscosity for northern Europe. *Geophysical Journal International*, *134*, 102–144. doi: 10.1046/j.1365-246X.1998.00541.x

Lau, H. C. P., Mitrovica, J. X., Davis, J. L., Tromp, J., Yang, H.-Y., & Al-Attar, D. (2017). Tidal tomography constrains Earth's deep-mantle buoyancy. *Nature*, *551*(7680), 321–326. doi: 10.1038/nature24452

Lekić, V., & Fischer, K. M. (2014). Contrasting lithospheric signatures across the western United States revealed by Sp receiver functions. *Earth and Planetary Science Letters*, *402*, 90–98. doi: 10.1016/j.epsl.2013.11.026

Lu, C., Forte, A. M., Simmons, N. A., Grand, S. P., Kajan, M. N., Lai, H., & Garnero, E. J. (2020). The Sensitivity of Joint Inversions of Seismic and Geodynamic Data to Mantle Viscosity. *Geochemistry, Geophysics, Geosystems*, *21*(4), 1–29. doi: 10.1029/2019gc008648

McKenzie, D. (1977). Surface deformation, gravity anomalies and convection. *Geophysical Journal of the Royal Astronomical Society*, *48*, 211–238. doi: 10.1111/j.1365-246X.1977.tb01297.x

McKenzie, D. P., Roberts, J. M., & Weiss, N. O. (1974). Convection in the earth's mantle: Towards a numerical simulation. *Journal of Fluid Mechanics*, *62*(3), 465–538. doi: 10.1017/S0022112074000784

Menard, H. W. (1973). Depth anomalies and the bobbing motion of drifting islands. *Journal of Geophysical Research*, *78*(23), 5128–5137. doi: 10.1029/jb078i023p05128

Merdith, A. S., Williams, S. E., Collins, A. S., Tetley, M. G., Mulder, J. A., Blades, M. L., ... Müller, R. D. (2021). Extending full-plate tectonic models into deep time: Linking the Neoproterozoic and the Phanerozoic. *Earth-Science Reviews*, *214*(103477), 1–44. doi: 10.1016/j.earscirev.2020.103477

Mitrovica, J. X., & Forte, A. M. (2004). A new inference of mantle viscosity based upon joint inversion of convection and glacial isostatic adjustment data. *Earth and Planetary Science Letters*, *225*(1-2), 177–189. doi: 10.1016/j.epsl.2004.06.005

Molnar, P., England, P. C., & Jones, C. H. (2015, mar). Mantle dynamics, isostasy, and the support of high terrain. *Journal of Geophysical Research: Solid Earth*, *120*(3), 1932–1957. Retrieved from `http://doi.wiley.com/10.1002/2014JB011724` doi: 10.1002/2014JB011724

Morris, M., Fernandes, V. M., & Roberts, G. G. (2020). Extricating dynamic topography from subsidence patterns: Examples from Eastern North America's passive margin. *Earth and Planetary Science Letters*, *530*(115840), 1–13. Retrieved from https://doi.org/10.1016/j.epsl.2019.115840 doi: 10.1016/j.epsl.2019.115840

Moucha, R., & Forte, A. M. (2011). Changes in African topography driven by mantle convection: supplementary information. *Nature Geoscience*, *4*(10), 707–712. doi: 10.1038/ngeo1235

Moucha, R., Forte, A. M., Mitrovica, J. X., & Daradich, A. (2007). Lateral variations in mantle rheology: Implications for convection related surface observables and inferred viscosity models. *Geophysical Journal International*, *169*(1), 113–135. doi: 10.1111/j.1365-246X.2006.03225.x

Moucha, R., Forte, A. M., Mitrovica, J. X., Rowley, D. B., Quéré, S., Simmons, N. A., & Grand, S. P. (2008). Dynamic topography and long-term sea-level variations: There is no such thing as a stable continental platform. *Earth and Planetary Science Letters*, *271*(1-4), 101–108. doi: 10.1016/j.epsl.2008.03.056

O'Connell, R. J. (1971). Pleistocene Glaciation and the Viscosity of the Lower Mantle. *Geophysical Journal of the Royal Astronomical Society*, *23*(3), 299–327. doi: 10.1111/j.1365-246X.1971.tb01823.x

O'Malley, C. P. B., White, N. J., Stephenson, S. N., & Roberts, G. G. (2021). Large-Scale Tectonic Forcing of the African Landscape. *Journal of Geophysical Research: Earth Surface*, *126*, 1–37. doi: 10.1029/2021jf006345

Panasyuk, S. V., Hager, B. H., & Forte, A. M. (1996). Understanding the effects of mantle compressibility on geoid kernels. *Geophysical Journal International*, *124*(1), 121–133. doi: 10.1111/j.1365-246X.1996.tb06357.x

Panton, J., Davies, J. H., & Myhill, R. (2023). The Stability of Dense Oceanic Crust Near the Core-Mantle Boundary. *Journal of Geophysical Research: Solid Earth*, *128*, 1–21. doi: 10.1029/2022JB025610

Parsons, B., & Daly, S. (1983). The relationship between surface topography, gravity anomalies and temperature structure of convection. *Journal of Geophysical Research*, *88*(B2), 1129–1144. doi: 10.1029/JB088iB02p01129

Pekeris, C. L. (1935). Thermal Convection in the Interior of the Earth. *Geophysical Supplements to the Monthly Notices of the Royal Astronomical Society*, *3*(8), 343–367.

Priestley, K., & McKenzie, D. (2013). The relationship between shear wave velocity, temperature, attenuation and viscosity in the shallow part of the mantle. *Earth and Planetary Science Letters*, *381*, 78–91. Retrieved from http://dx.doi.org/10.1016/j.epsl.2013.08.022 doi: 10.1016/j.epsl.2013.08.022

Ribe, N. M. (2007). Analytical Approaches to Mantle Dynamics. *Treatise on Geophysics*, *7*, 167–226. doi: 10.1016/B978-044452748-6.00117-6

Ricard, Y. (2007). Physics of Mantle Convection. *Treatise on Geophysics*, *7*, 31–88.

Ricard, Y. (2015). Physics of Mantle Convection. In G. Schubert (Ed.), *Treatise on geophysics* (pp. 23–71). doi: 10.1016/B978-044452748-6.00115-2

Richards, F. D., Hoggard, M. J., Ghelichkhan, S., Koelemeijer, P., & Lau, H. C. P. (2021). Geodynamic, geodetic, and seismic constraints favour deflated and dense-cored LLVPs. *EarthArXiv*, 1–20. doi: 10.31223/X55601

Richards, F. D., Hoggard, M. J., Ghelichkhan, S., Koelemeijer, P., & Lau, H. C. P. (2023). Geodynamic, geodetic, and seismic constraints favour deflated and dense-cored LLVPs. *Earth and Planetary Science Letters*, *602*(117964), 1–13. Retrieved from https://doi.org/10.1016/j.epsl.2022.117964 doi: 10.1016/j.epsl.2022.117964

Richards, F. D., Hoggard, M. J., White, N., & Ghelichkhan, S. (2020). Quantifying the relationship between short-wavelength dynamic topography and thermomechanical structure of the upper mantle using calibrated parameterization of anelasticity. *Journal of Geophysical Research: Solid Earth*, *125*, 1–36. doi:

10.1029/2019JB019062

Richards, M. A., & Hager, B. H. (1984). Geoid Anomalies in a Dynamic Earth. *Journal of Geophysical Research*, *89*(B7), 5987–6002. doi: 10.1029/JB089iB07p05987

Salles, T., Flament, N., & Müller, D. (2017, jan). Influence of mantle flow on the drainage of eastern Australia since the Jurassic Period. *Geochemistry, Geophysics, Geosystems*, *18*(1), 280–305. doi: 10.1002/2016GC006617

Spasojevic, S., & Gurnis, M. (2012). Sea level and vertical motion of continents from dynamic earth models since the Late Cretaceous. *AAPG Bulletin*, *96*(11), 2037–2064. doi: 10.1306/03261211121

Stanley, J. R., Braun, J., Baby, G., Guillocheau, F., Robin, C., Flowers, R. M., … Beucher, R. (2021). Constraining Plateau Uplift in Southern Africa by Combining Thermochronology, Sediment Flux, Topography, and Landscape Evolution Modeling. *Journal of Geophysical Research: Solid Earth*, *126*, 1–34. doi: 10.1029/2020JB021243

Steinberger, B. (2007). Effects of latent heat release at phase boundaries on flow in the Earth's mantle, phase boundary topography and dynamic topography at the Earth's surface. *Physics of the Earth and Planetary Interiors*, *164*(1-2), 2–20. doi: 10.1016/j.pepi.2007.04.021

Steinberger, B. (2016). Topography caused by mantle density variations: Observation-based estimates and models derived from tomography and lithosphere thickness. *Geophysical Journal International*, *205*(1), 604–621. doi: 10.1093/gji/ggw040

Steinberger, B., & Antretter, M. (2006). Conduit diameter and buoyant rising speed of mantle plumes: Implications for the motion of hot spots and shape of plume conduits. *Geochemistry, Geophysics, Geosystems*, *7*(11), 1–25. doi: 10.1029/2006GC001409

Steinberger, B., & Calderwood, A. R. (2006). Models of large-scale viscous flow in the Earth's mantle with constraints from mineral physics and surface observations. *Geophysical Journal International*, *167*(3), 1461–1481. doi: 10.1111/j.1365-246X.2006.03131.x

Steinberger, B., & O'Connell, R. J. (1997). Changes of the Earth's rotation axis owing to advection of mantle density heterogeneities. *Nature*, *387*, 169–173. doi: 10.1038/387169a0

Stephenson, S. N., White, N. J., Carter, A., Seward, D., Ball, P. W., & Klöcking, M. (2021). Cenozoic Dynamic Topography of Madagascar. *Geochemistry, Geophysics, Geosystems*, *22*, 1–38. doi: 10.1029/2020gc009624

Tackley, P. J., Stevenson, D. J., Glatzmaier, G. A., & Schubert, G. (1993). Effects of an endothermic phase transition at 670 km depth on spherical mantle convection. *Nature*, *361*, 699–704. doi: 10.1038/361699a0

Thoraval, C., Machete, P., & Cazenave, A. (1994). Influence of mantle compressibility and ocean warping on dynamical models of the geoid. *Geophysical Journal International*, *117*, 566–573. doi: 10.1111/j.1365-246X.1994.tb03954.x

Thoraval, C., & Richards, M. A. (1997). The geoid constraint in global geodynamics: Viscosity structure, mantle heterogeneity models and boundary conditions. *Geophysical Journal International*, *131*, 1–8. doi: 10.1111/j.1365-246X.1997.tb00591.x

Turcotte, D. L., & Schubert, G. (2002). *Geodynamics* (Second Edi ed.). Cambridge University Press.

van Heck, H. J., Davies, J. H., Elliott, T., & Porcelli, D. (2016). Global-scale modelling of melting and isotopic evolution of Earth's mantle: Melting modules for TERRA. *Geoscientific Model Development*, *9*, 1399–1411. doi: 10.5194/gmd-9-1399-2016

Wieczorek, M. A., & Meschede, M. (2018). SHTools: Tools for Working with Spherical Harmonics. *Geochemistry, Geophysics, Geosystems*, *19*, 1–19.

Retrieved from http://doi.wiley.com/10.1029/2018GC007529 doi: 10.1029/2018GC007529

Zhong, S., Gurnis, M., & Hulbert, G. (1993). Accurate determination of surface normal stress in viscous flow from a consistent boundary flux method. *Physics of the Earth and Planetary Interiors*, *78*, 1–8. doi: 10.1016/0031-9201(93)90078-N

Zhong, S., McNamara, A., Tan, E., Moresi, L., & Gurnis, M. (2008). A benchmark study on mantle convection in a 3-D spherical shell using CitcomS. *Geochemistry, Geophysics, Geosystems*, *9*(10), 1–32. doi: 10.1029/2008GC002048

Zhong, S., Zuber, M. T., Moresi, L., & Gurnis, M. (2000). Role of temperature-dependent viscosity and surface plates in spherical shell models of mantle convection. *Journal of Geophysical Research*, *105*(B5), 11063–11082.

Figure 1. Examples of mantle densities and viscosity used to calculate stresses and dynamic topography numerically and analytically. (a) Great-circle slice (180°) through full-resolution, present-day, density ρ, predicted by TERRA model with temperature dependent viscosity (Model 11a; see Table 2 and body text); see globe to left for location. White circles = 20° intervals; filled black circle indicates orientation of cross section; dashed line = 660 km depth contour; dotted line = 1038 km depth contour, at which depth ρ is plotted on globe; white-black curve = numerical prediction of surface normal stress σ_{rr} from Model 11a. (b) As (a) but slice is through spherical harmonic expansion of density structure, to maximum degree $l = 50$ ($\lambda \approx 792$ km; Model 11b); black-white curve = surface deflection h, calculated using (analytic) propagator matrix approach (Model 12). (c) As (a) but for slice through full-resolution viscosity structure of numerical model. (d) As (c) but for mean (radial) viscosity structure, used along with the density structure shown in (b) to generate analytical solution for surface deflection shown by black-white curve atop (b). (e–f) As (c–d) but viscosity is expressed as a percentage anomaly with respect to the layer (radial) mean.

Figure 2. Model 1: Densities predicted from numerical simulation of mantle convection. (a) Predicted present-day density ρ, at surface (z=0), from TERRA model with viscosity independent of temperature (Table 2: Model 1a), plotted at grid resolution of 1 degree. (b) Histogram of values shown in (a), weighted by latitude to correct to equal-area. (c–d) As (a–b) but for densities at a depth of 270 km. (e–h) As (a–d) but for time slice at 10 Ma; paleocoastlines generated from Phanerozoic plate rotation history of Merdith et al. (2021). (i–l) As (a–d) but for time slice at 100 Ma.

Figure 3. Model 1: Surface stresses from numerical simulation of mantle convection and spherical harmonic expansion up to degree 50. (a) Predicted present-day surface radial stress, σ_{rr} from numerical TERRA model (Model 1a), plotted at grid resolution of 1 degree. (b) Histogram of values shown in (a), weighted by latitude to correct to equal-area. (c) Black line = radial viscosity structure used to drive Model 1a and thus produce grid shown in panel (a). Gray dashed lines = alternative viscosity profiles of (from darkest to lightest), Mitrovica and Forte (2004), Steinberger and Calderwood (2006), and μ_1, μ_2 from Ghelichkhan et al. (2021). (d) Model 1b: Global interpolation of spherical harmonic expansion of Model 1a (panel a), up to maximum degree $l = 50$ (i.e., minimum wavelength $\lambda \approx 792$ km; Model 1b), calculated using inversion approach of Hoggard et al. (2016). (e) Histogram of values shown in (d), weighted by latitude to correct to equal-area. (f) Power spectrum, in terms of total power per degree, of stress field shown in (d), as a function of spherical harmonic degree l.

Figure 4. Model 1: Predicted water- and air-loaded dynamic topography. (a) Water-loaded, present day, surface deflection predicted by Model 1a. Figure 3a shows normal stress, σ, used with Equation 11 to calculate dynamic topography, h; $\rho_w = 1030$ kg m^{-3}. (b) Spherical harmonic fit (Model 1b) up to degree $l = 50$ of grid shown in (a), calculated using the approach of Hoggard et al. (2016). (c–d) Histogram of values shown in (a) and (b) respectively, weighted by latitude to correct to equal-area. (e) Black line = power spectrum in terms of total power per degree, from spherical harmonic expansion shown in (b); gray line and band = expected dynamic topography from Kaula's rule using admittance $Z = 12 \pm 3$ mGal km^{-1} (Kaula, 1963). Orange dashed line = expected power spectrum for water-loaded residual topography from Holdt et al. (2022), via analytical solution of special case of Equation 16. χ_p = total root-mean-squared difference between distribution of modeled and theoretical surface deflection power (see Equation 21. (f–j) As (a–e) but for air-loaded surface deflection; $\rho_w = 1$ kg m^{-3}.

Figure 5. Model 2: Propagator matrix solution for surface deflection with associated sensitivity kernels. (a) Surface deflection sensitivity kernel A_l, as a function of spherical harmonic degree, l, and depth, calculated for the radial viscosity structure (and other parameters) which were used to generate Model 1; see Equation 17. (b) Present-day predicted water-loaded surface deflection, calculated using propagator matrix method, from spherical harmonic expansion (to maximum degree $l = 50$) of density structure (e.g., Figure 2a, c) and radial viscosity structure (e.g., Figure 3c; Corrieu et al., 1995; Hager et al., 1985; Parsons & Daly, 1983). Note that for comparison with numeric calculations shown in Figure 4, no terms related to flow-related perturbation of gravitational potential terms are included (see Equations 17 and 18), and gravitational acceleration $g = 10$ m s^{-2} everywhere. (c) Histogram of values shown in (b), weighted by latitude to correct to equal-area. (d) Black line = power spectrum in terms of total power per degree, from surface deflection prediction shown in (a); gray line and band = expected dynamic topography from Kaula's rule using admittance $Z = 12 \pm 3$ mGal km^{-1} (Kaula, 1963). Orange dashed line = power spectrum of water-loaded residual topography from Holdt et al. (2022), via analytical solution of special case of Equation 16. χ_p = total root-mean-squared difference between distribution of modeled and theoretical surface deflection power (see Equation 21. (e–h) As (a–d) but for air-loaded surface deflection; $\rho_w = 1$ kg m^{-3}.

Figure 6. Comparison of numeric and analytic estimation of dynamic topography (Models 1b & 2). (a) Model 1b: Spherical harmonic expansion of predicted present-day water-loaded surface deflection converted from stress output from TERRA (Model 1a), to maximum degree $l = 50$, as in Figure 4f. (b) Model 2: As (a) but for prediction made using propagator matrix method, as in Figure 5b. (c) Difference, Δh, between Models 1b and 2 (panels a and b). (d) Histogram of difference values shown in (c), weighted by latitude to correct to equal-area. (e) Spectral correlation coefficient, r_l, between predictions shown in (a) and (b); Equation 20. (f) Numeric (Model 1b) versus analytic (Model 2) predictions of surface deflection; χ = root-mean-squared difference between predictions, Equation 19; gray dashed line = 1:1 ratio. (g) Black bars = histogram of ratios between analytic:numeric solutions for surface deflection as in (f), weighted by latitude. Gray dashed line = 1 (i.e., identical values). Gray bars = as black bars, but for propagator matrix solution amplitudes scaled up by optimal factor to fit numerical solution (10%).

Figure 7. Model 3: Predicted surface deflection from mantle convection in presence of radial gravitation. (a) Predicted present-day water-loaded surface deflection calculated using propagator matrix method, incorporating radial gravitation i.e., $g(r)$, black curve in (b). (b) Black curve = profile of gravitational acceleration as a function of radius, given density distribution predicted by Model 1a; gray dashed line = constant value of $g = 10$ m s^{-2} used within TERRA model runs and in previous figures. (c) As (a) but calculated using $g = 10$ m s^{-2} everywhere, i.e., same as Figure 5a (dashed line in panel b). (d) Difference between surface deflections predicted by Models 3 and 2 (panels a and c). (e) Histogram of values in (d), weighted by latitude to correct to equal-area.

Figure 8. Model 4: Comparing predicted surface deflections with and without stress perturbations induced by gravitational potential of deflected surface. (a) Predicted present-day water-loaded surface deflection calculated using propagator matrix method, with $g = 10$ m s^{-2} everywhere, including terms describing stress perturbation due to change in gravitational potential (i.e., u_3 term in Equation 17). (b) As (a) but calculated excluding u_3 term, i.e., same as Figure 5a. (c) Difference between Models 4 and 2 (panels a and b). Note same colour scales are used as in Figure 7. (d) Histogram of values in (d), weighted by latitude to correct to equal-area.

Figure 9. Models 5–7: Effect of removing shallow structure from analytic surface deflection calculations. (a) Model 5: Predicted water-loaded surface deflection from propagator matrix solution for Model 2, i.e., as Figure 5b, but with effect of upper 50 km of density anomaly structure ignored in calculation. (b) Black line = power spectrum of surface deflection shown in (a); gray line and band = expected dynamic topography from Kaula's rule using admittance $Z = 12 \pm 3$ mGal km^{-1} (Kaula, 1963). Orange dashed line = expected power spectrum for water-loaded residual topography from Holdt et al. (2022), via analytical solution of special case of Equation 16. χ_p = total root-mean-squared difference between distribution of modeled and theoretical surface deflection power (see Equation 21). (c) Difference between Models 5 and 2, i.e., between panel (a) and original propagator matrix solution, Model 2, shown in Figure 5b. (d) Spectral correlation coefficient, r_l, between Model 5 and 2; Equation 20. (e–h) and (i–l) as (a–d) but for depth cut-offs of 100 (Model 6) and 200 km (Model 7), respectively.

Figure 10. Models 8–10: Testing free-slip vs. no-slip ("rigid") surface and CMB boundary conditions. (a) Water-loaded surface deflection sensitivity kernel A_l, for Model 8, which has a no-slip surface boundary condition, but otherwise is parameterised the same as Model 2. (b) Sensitivity kernel of Model 8 minus sensitivity kernel of Model 2 (see Figure 5a). Note, positive difference implies reduced sensitivity compared to Model 2, and vice versa, since A_l is negative. (c) Predicted water-loaded surface deflection for Model 8. (d) Difference between surface deflection predictions for Model 8 and Model 2 (see Figure 5b). (e–h) as (a–d) but for Model 9: free-slip surface boundary, no-slip CMB. (i–l) as (a–d) but for Model 10: no-slip surface and CMB boundaries.

Figure 11. Model 11: Numerical simulation of mantle convection with temperature dependent viscosity, η, and spherical harmonic representation. (a) Present-day viscosity at surface from Model 11a, expressed as percentage deviation from layer mean, $\delta\eta$, plotted at grid resolution of 1 degree. (b) Histogram of values shown in (a), weighted by latitude to correct to equal-area. (c) Black line and gray band = global mean and extreme viscosity values as a function of depth; pink band = depth slice shown in (a). (d) Model 11b: Spherical harmonic fit up to degree $l = 50$ of grid shown in (a), using inverse approach of Hoggard et al. (2016). (e–h) As (a–d) but for depth slice at 271 km below surface. (i–l) and (m–p) 587 km and 2032 km depth slices.

Figure 12. Model 11: Densities predicted by numerical simulation with temperature-dependent viscosity. (a) Predicted present-day density ρ, at surface (z=0), from TERRA model. (b) Histogram of values shown in (a), weighted by latitude. (c–d) As panels (a–b) but for densities at 270 km depth. (e–h) and (i–l) As panels (a–d) for time slices at 10 and 100 Ma (see caption of Figure 2 for expanded description; Figure 11 for viscosity structure; Equation 7).

Figure 13. Model 11: Predictions of surface stresses and deflections from simulations with temperature dependent viscosity. (a) Predicted present-day surface radial stress, σ_{rr} from numerical TERRA model (Model 11a), plotted at grid resolution of 1 degree. (b) Model 11b: Spherical harmonic representation of Model 11a up to degree $l = 50$. (c) Histogram of values shown in (a), weighted by latitude to correct to equal-area. (d) Histogram of values shown in panel (b). (e) Power spectrum of surface stresses. (f–i) Calculated water-loaded surface deflections and associated histograms for full resolution numerical solutions (f, h) and spherical harmonic representation (g, i). (j) Power spectrum (black) of water-loaded surface deflection (panel g), Kaula's rule (grey curve and band), and water-loaded residual topography (orange); see Figure 4 for expanded description.

Figure 14. Model 12: Analytical (propagator matrix) predictions of surface deflections from simulations with temperature dependent viscosity. Radial viscosity is calculated using mean (radial) values from numerical model with temperature-dependent viscosity (i.e., Model 11a; Figure 13). (a–d) Present-day, water-loaded, surface deflection calculated analytically using propagator matrix solution; see Figure 5 for expanded description of panels. (e–h) Air-loaded deflection and associated metrics.

Figure 15. Models 11b & 12: Comparison of surface deflections calculated numerically and analytically using results from simulation with temperature dependent viscosity. (a) Model 11b: Spherical harmonic expansion of predicted present-day water-loaded surface deflection converted from stress output from TERRA (Model 11a), to maximum degree $l = 50$. (b) Model 12: As (a) but for prediction made using propagator matrix method. (c) Difference, Δh, between Models 11b and 12 (panels a and b). (d) Histogram of difference values shown in (c), weighted by latitude to correct to equal-area. (e) Spectral correlation coefficient, r_l, between predictions shown in (a) and (b); Equation 20. (f) Numeric (Model 11b) versus analytic (Model 12) predictions of surface deflection; χ = root-mean-squared difference between predictions, Equation 19; gray dashed line = 1:1 ratio. (g) Histogram of ratios between analytic:numeric solutions for surface deflection as in (f), weighted by latitude. Gray dashed line = 1 (i.e., identical values). Gray bars = as black bars, but for propagator matrix solution amplitudes scaled up by optimal factor to fit numerical solution (24%).

Figure 16. Comparing surface deflections calculated using normal stresses from numeric simulations (Models 1 and 11) and analytic estimates (Models 2 and 12) with and without temperature dependent viscosity. (a) Difference in predicted surface deflection, Δh, between numerical simulations with (Model 11a) and without (Model 1a) temperature-dependent viscosity. Full-resolution surface radial stresses are converted into surface deflections, h, using Equation 11. (b) Histogram of values shown in (a). (c) Pixel-wise comparison of predicted surface deflection between the two models; χ = root-mean-squared difference between predictions, see Equation 19; gray dashed line = 1:1 ratio. (d–f) as (a–c) but for surface deflection calculated using spherical harmonic expansion of surface radial stresses (Model 1b vs. 11b). (g) Spectral correlation coefficient, r_l, between model predictions (with and without temperature dependent viscosity; see Equation 20). (h–k) as (d–g) but for surface deflections calculated for each model using the propagator matrix approach (Model 2 vs. 12).

Figure 17. Models 13–16: Sensitivity of calculated analytic surface deflection to adjusted radial viscosity. (a) Model 13: Black curve = prediction of present-day radial mean viscosity from Model 11; red line = adjusted radial profile with viscosity decreased by a factor of 10 between depths of $\sim$ 300–500 km; gray dashed lines = viscosity profiles used in other studies (see Figure 3). (b) Sensitivity kernel generated using adjusted viscosity shown in (a). (c) Surface deflection calculated using propagator matrix approach parameterised using adjusted viscosity profile (red curve in panel a), and resulting sensitivity kernel shown in panel (b). (d) Difference between propagator matrix solutions generated using adjusted and un-adjusted viscosity profiles, i.e., panel (c) minus Figure 15b (Model 13 vs. 12). Value of root-mean-squared difference, χ, (between calculated surface deflections for un-adjusted and adjusted viscosity) is stated (see Equation 19). (e–h) Model 14: As (a–d) but applying an increase in viscosity of a factor of 10 between $\sim$ 300–500 km. (i–l) Model 15: As (a–d) but applying an increase in viscosity of a factor of 100 between $\sim$ 300–500 km. (m–p) Model 16: As (a–d) but applying an constant viscosity of $\approx 7.5 \times 10^{22}$ Pa s (i.e., the mean value of the reference profile) across all depths.

Figure 18. Models 17–20: Sensitivity of calculated analytic surface deflection to adjusted density anomalies. Annotation is as for Figure 17 but for adjusted density anomalies (red lines in left panels), by directly scaling spherical harmonic coefficients ($l > 0$) up or down by a factor of 2 (Models 17 & 19, panels a–c & g–i, respectively) or $\frac{1}{2}$ (Models 18 & 20: d–f & j–l). Viscosity structure applied in each case is same as that used to generate Figure 15b. Sensitivity kernels for surface deflection are not shown since they are invariant with respect to density anomalies, $\Delta\rho$, depending only on viscosity structure.

Figure 19. Effective density. Contributions from density anomalies to surface deflection. (a–d) Maps of net contribution to present-day water-loaded surface deflection calculated using propagator matrix approach (Model 12; see body text for details). Depth slices at 45, 135, 360 and 1445 km depth incorporating all spherical harmonic degrees l and orders m, up to $l = 50$. (e) Great-circle slice (180°) showing contributions to surface deflection; globe to right shows transect location and calculated surface deflection (same as Figure 14b). White circles = 20° intervals; note filled black circle for orientation; dashed line = 660 km depth contour. (f) White-black curve = total surface deflection along transect shown atop globe in panel (e); abscissa aligned with panel g; orange dashed line = same but for maximum l = 10 (see Supporting Information Figure S4); red dashed curve = surface deflection from Model 2. (g) Cartesian version of panel (e); ordinate aligned with panel (h). (h) Grey dashed curve = mean absolute value of density anomalies in Model 12—see top axis for values. Black curve = global mean amplitude (modulus) of contribution from density structure in Model 12 to total surface deflection h, across all l and m; orange line = same but for maximum $l = 10$; red dashed line = results for Model 2.

Figure 1.

a
b
c
d
e
f
-σrr
+σrr
+h
-h
4700
4600
4500
4400
ρ (kg.m-3)
10^23
10^22
Viscosity, Pa.s
100
50
0
−50
−100
Viscosity Anomaly, %
Numerical
Analytic
Depth, km
2000
1000
0

Figure 2.

ρ (kg.m-3)
4400
4500
4600
4700
ρ (kg/m3)
4400 4500 4600 4700
a
0 Ma
z = 0 km
b
c
0 Ma
z = 270 km
d
Count (103)
0 5 10 15 20 25
e
10 Ma
z = 0 km
f
g
10 Ma
z = 270 km
h
i
100 Ma
z = 0 km
j
k
100 Ma
z = 270 km
l

Figure 3.

a
b
c
d
e
f
σrr (GPa)
−0.5 0.0 0.5
0 Ma
z = 0 km
Count (10³)
Mean η, Pa.s
10²¹ 10²² 10²³ 10²⁴
Depth, km
0 500 1000 1500 2000 2500
Degree, l
0 10 20 30 40 50
Power (Pa²)
10¹⁴ 10¹⁵ 10¹⁶ 10¹⁷

Figure 4.

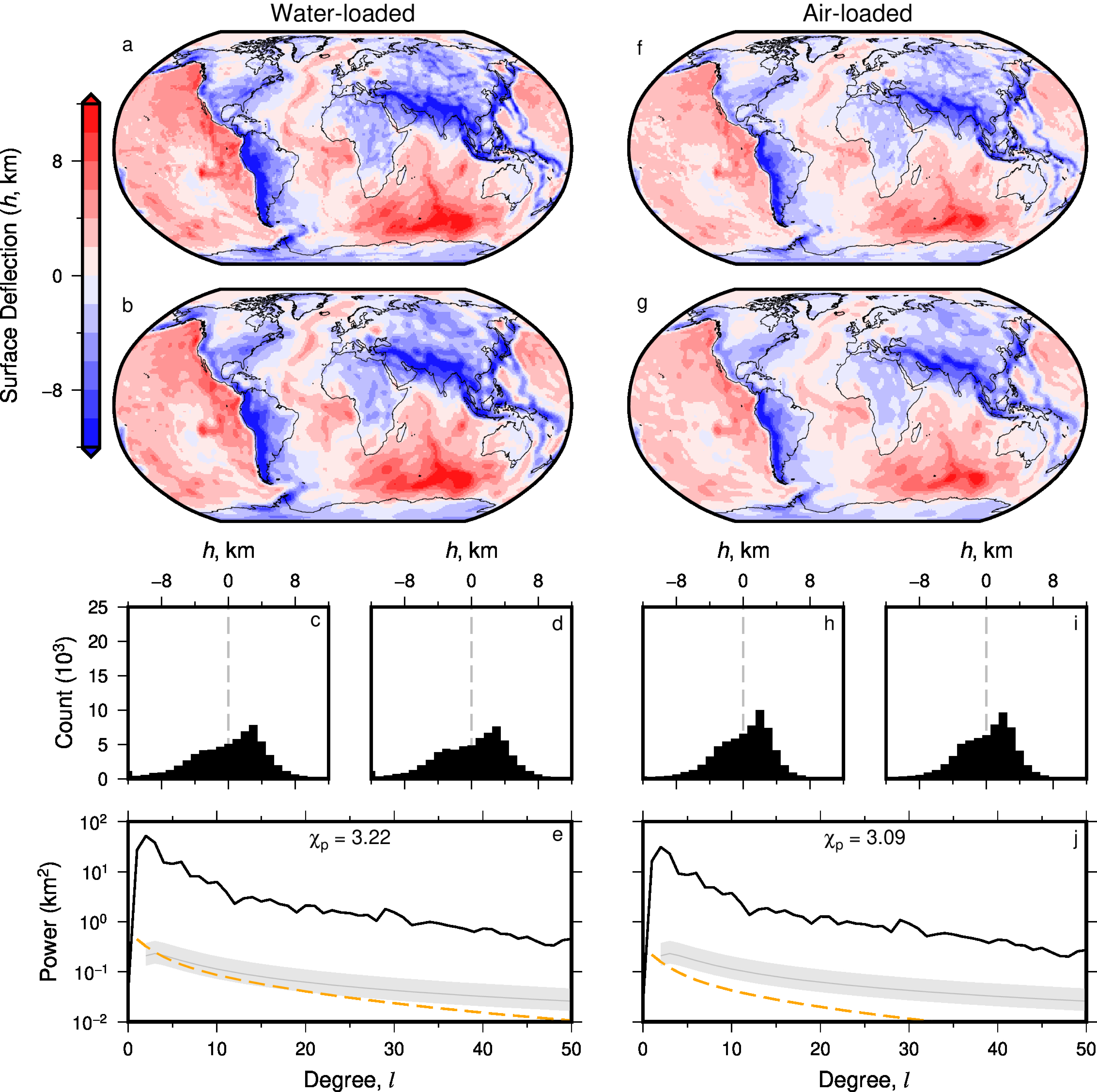

Water-loaded
Air-loaded
Surface Deflection (h, km)
8
0
−8
a
b
f
g
h, km
−8
0
8
Count (10^3)
25
20
15
10
5
0
c
d
h
i
Power (km^2)
10^2
10^1
10^0
10^{-1}
10^{-2}
χ_p = 3.22
χ_p = 3.09
e
j
0
10
20
30
40
50
Degree, l

Figure 5.

A_l, 10^{-4} kg.m^{-2}
–3 –2 –1 0
Surface Deflection (h, km)
–8 0 8
l
20 40
Depth, km
0 1000 2000
a
Water-loaded
b
h, km
–8 0 8
c
Count (10^3)
0 5 10 15 20 25
Degree, l
0 10 20 30 40 50
χ_p = 2.81
d
Power (km^2)
10^{-2} 10^{-1} 10^0 10^1 10^2
e
Air-loaded
f
g
χ_p = 2.68
h

Figure 6.

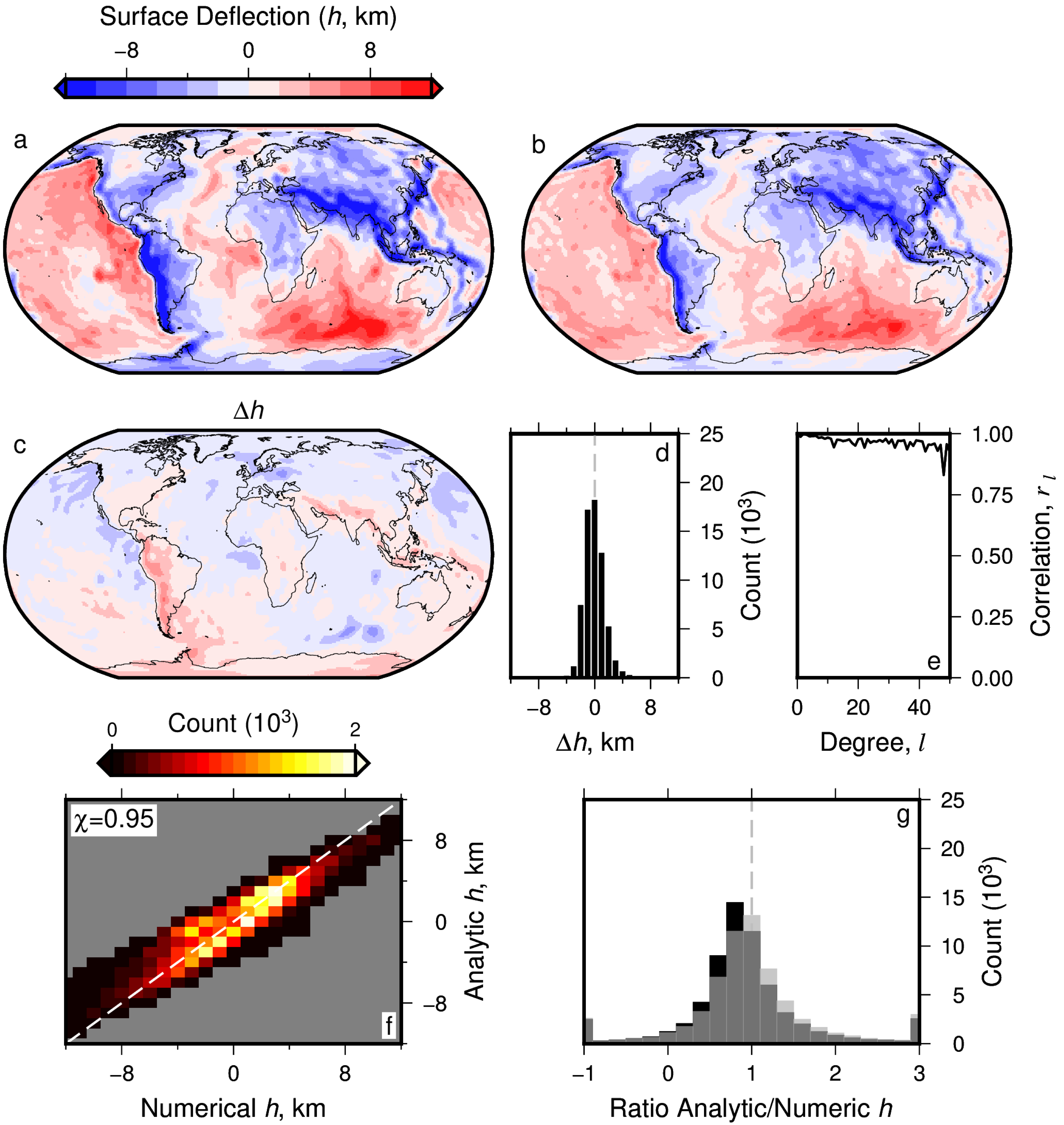

Surface Deflection (h, km)
−8
0
8
a
b
Δh
c
d
Δh, km
Count (10^3)
e
Degree, l
Correlation, r_l
Count (10^3)
0
2
χ=0.95
f
Numerical h, km
Analytic h, km
g
Ratio Analytic/Numeric h
Count (10^3)

Figure 7.

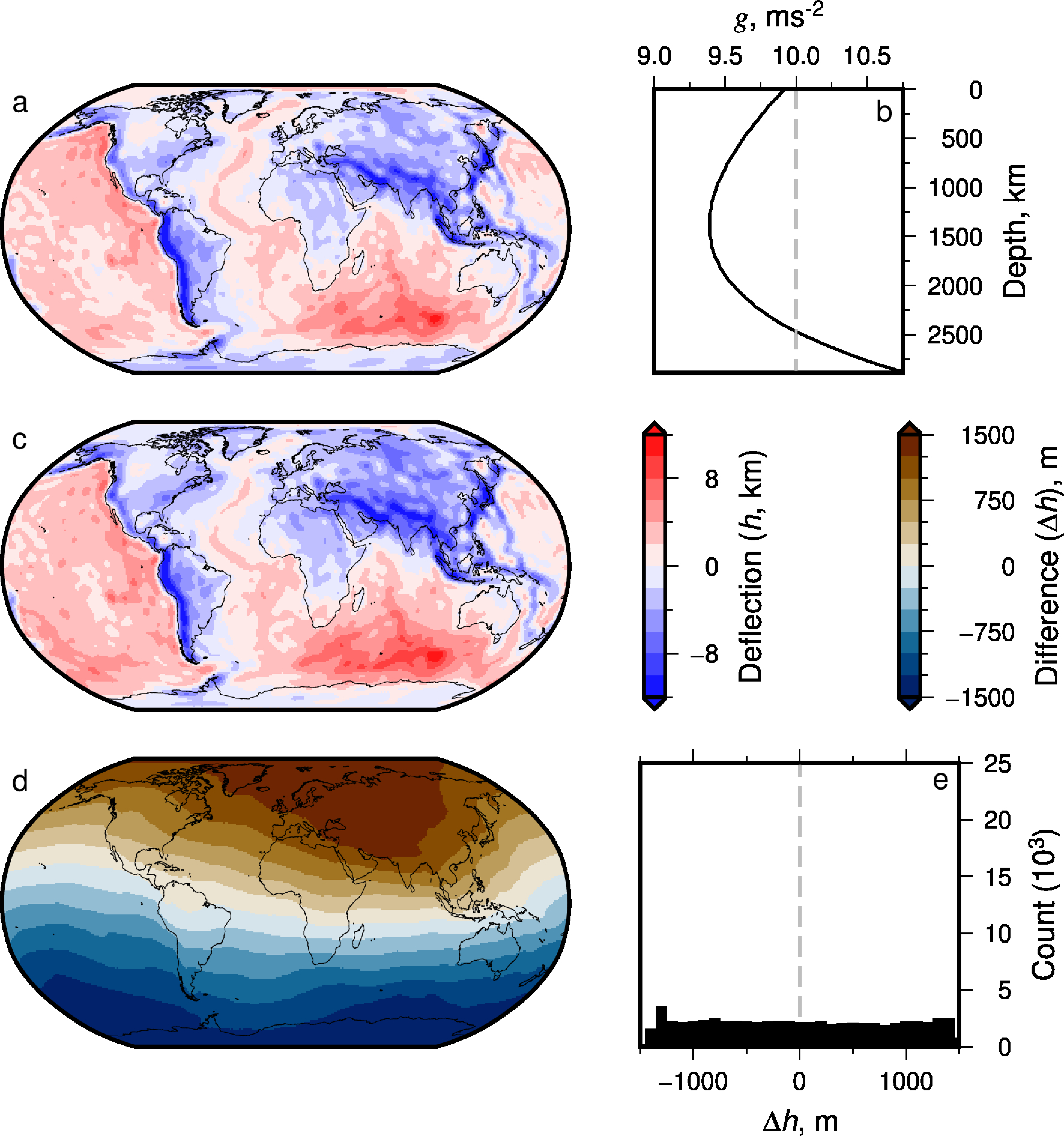

a
b
c
d
e
g, ms^{-2}
9.0
9.5
10.0
10.5
0
500
1000
1500
2000
2500
Depth, km
8
0
−8
Deflection (h, km)
1500
750
0
−750
−1500
Difference (Δh), m
25
20
15
10
5
0
Count (10^3)
−1000
0
1000
Δh, m

Figure 8.

Surface Deflection (h, km)
−8
0
8
Difference (Δh, m)
−1500
−750
0
750
1500
a
b
c
Δh, m
−1000
0
1000
d
25
20
15
10
5
0
Count (10^3)

Figure 9.

Surface Deflection (h, km)
−8
0
8
Degree, l
0
10
20
30
40
50
Δh
χ = 0.67
Degree, l
0
20
40
a
50 km cut-off
χ_p = 2.35
b
10^2
10^1
10^0
10^{-1}
10^{-2}
Power (km^2)
c
1.00
0.75
0.50
0.25
0.00
Correlation, r_l
d
e
100 km cut-off
χ_p = 1.89
f
χ = 1.03
g
h
i
200 km cut-off
χ_p = 1.11
j
χ = 1.57
k
l

Figure 10.

A_l, 10^{-4} kg.m^{-2}
–3 –2 –1 0
ΔA_l, 10^{-4} kg.m^{-2}
–2 0 2
Surface Deflection (h, km)
–8 0 8
l
20 40
Depth, km
0 1000 2000
Rigid-Free boundaries
Δh
χ = 1.26
Free-Rigid boundaries
χ = 1.09
Rigid-Rigid boundaries
χ = 1.00
a
b
c
d
e
f
g
h
i
j
k
l

Figure 11.

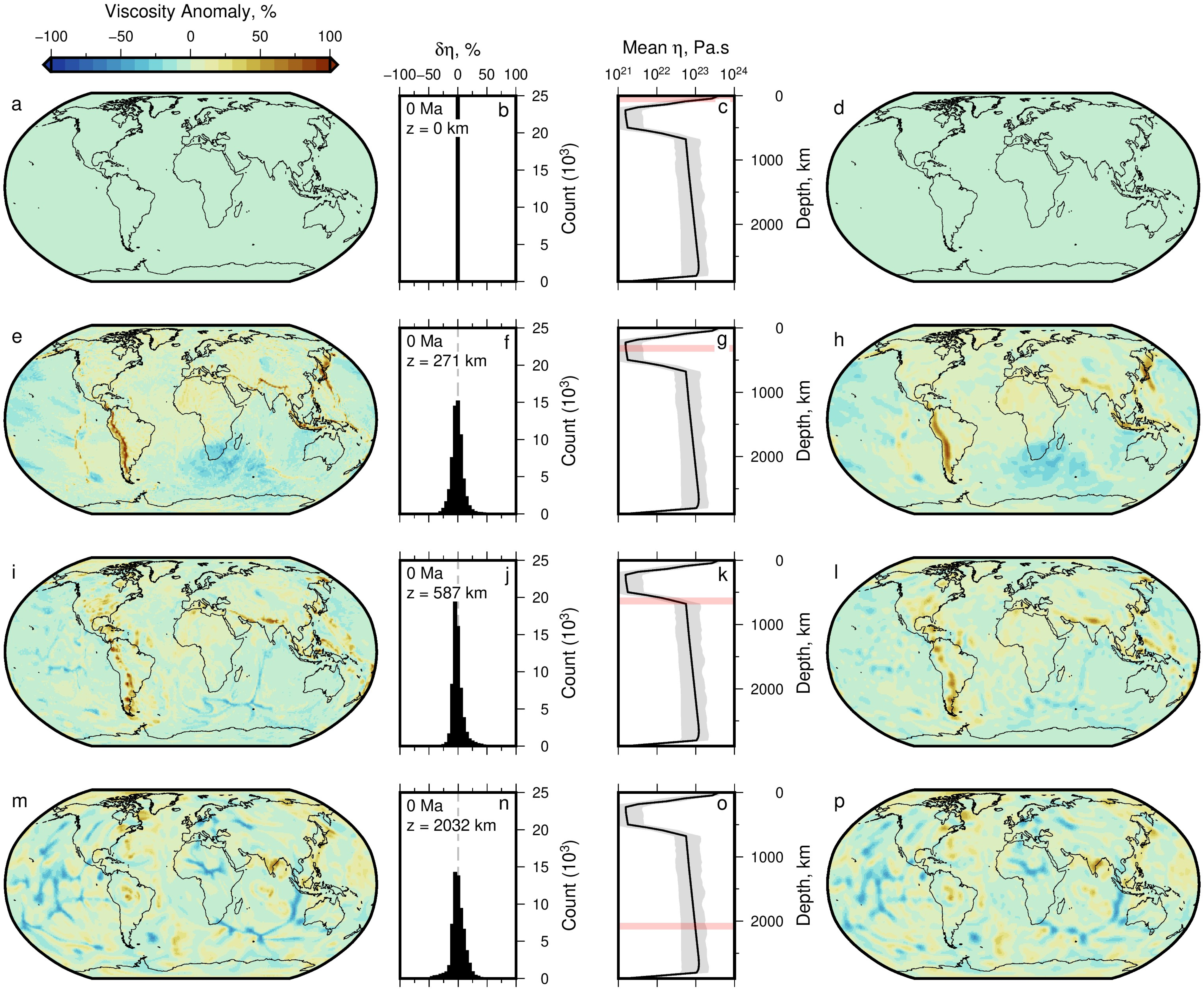

Viscosity Anomaly, %
−100
−50
0
50
100
δη, %
−100
−50
0
50
100
Mean η, Pa.s
10^{21}
10^{22}
10^{23}
10^{24}
a
b
0 Ma
z = 0 km
c
d
e
f
0 Ma
z = 271 km
g
h
i
j
0 Ma
z = 587 km
k
l
m
n
0 Ma
z = 2032 km
o
p
25
20
15
10
5
0
Count (10^3)
0
1000
2000
Depth, km

Figure 12.

ρ (kg.m-3)
4400
4500
4600
4700
ρ (kg/m3)
4400 4500 4600 4700
a
0 Ma
z = 0 km
b
Count (10³)
c
0 Ma
z = 270 km
d
e
10 Ma
z = 0 km
f
g
10 Ma
z = 270 km
h
i
100 Ma
z = 0 km
j
k
100 Ma
z = 270 km
l
0
5
10
15
20
25

Figure 13.

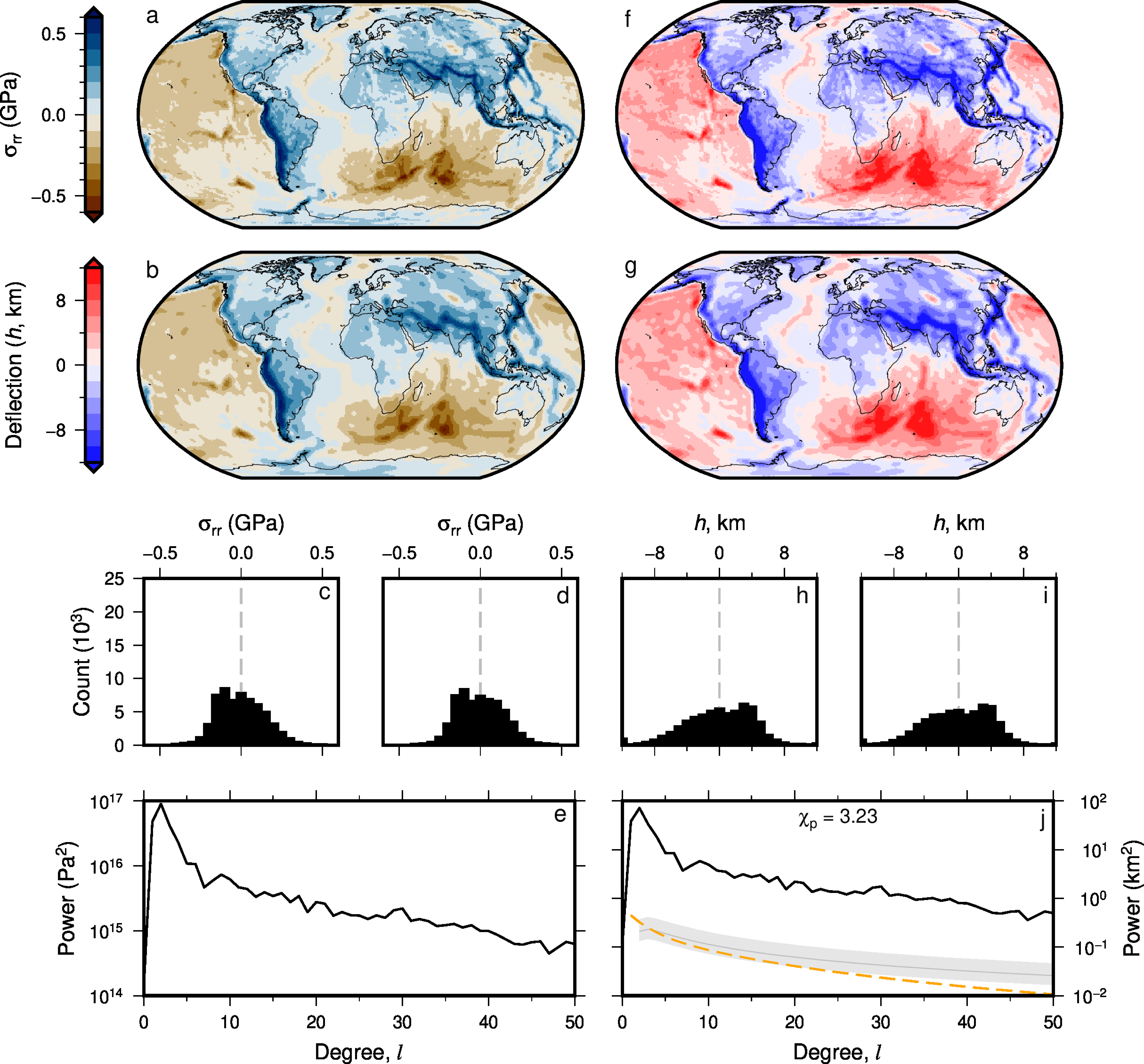

a
b
c
d
e
f
g
h
i
j
σ_{rr} (GPa)
Deflection (h, km)
0.5
0.0
−0.5
8
0
−8
σ_{rr} (GPa)
h, km
Count (10^3)
25
20
15
10
5
0
Power (Pa^2)
Power (km^2)
10^{17}
10^{16}
10^{15}
10^{14}
10^2
10^1
10^0
10^{-1}
10^{-2}
χ_p = 3.23
Degree, l
0
10
20
30
40
50

Figure 14.

A_l, 10^{-4} kg.m^{-2}
–3
–2
–1
0
Surface Deflection (h, km)
–8
0
8
l
20
40
Depth, km
0
1000
2000
a
Water-loaded
b
h, km
–8
0
8
c
Count (10^3)
25
20
15
10
5
0
Degree, l
0
10
20
30
40
50
χ_p = 2.65
d
Power (km^2)
10^2
10^1
10^0
10^{-1}
10^{-2}
e
Air-loaded
f
g
χ_p = 2.52
h

Figure 15.

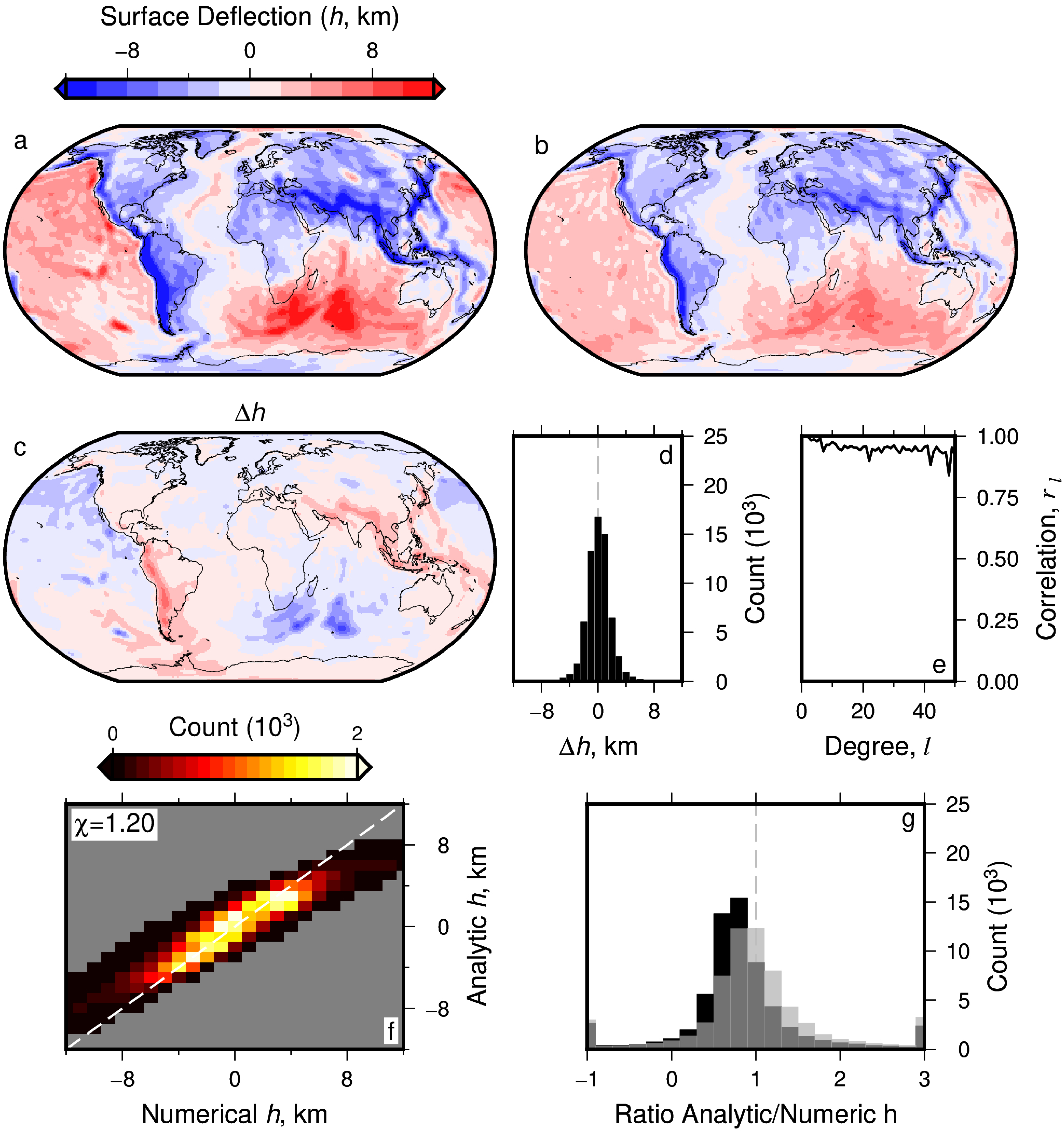

Surface Deflection (h, km)
−8
0
8
a
b
Δh
c
d
25
20
15
10
5
0
Count (10^3)
−8
0
8
Δh, km
e
1.00
0.75
0.50
0.25
0.00
Correlation, r_l
0
20
40
Degree, l
Count (10^3)
0
2
χ=1.20
f
8
0
−8
Analytic h, km
Numerical h, km
g
Count (10^3)
−1
0
1
2
3
Ratio Analytic/Numeric h

Figure 16.

Δh, km
−8
0
8
Model 1a vs. 11a
a
b
c
χ=1.51
Count (10³)
h, km
Count
2000
1000
0
Model 1b vs. 11b
d
e
f
g
χ=1.44
Correlation, r_l
Model 2 vs. 12
h
i
j
k
χ=0.92
Degree, l
0
20
40
0.00
0.25
0.50
0.75
1.00
25
20
15
10
5

Figure 17.

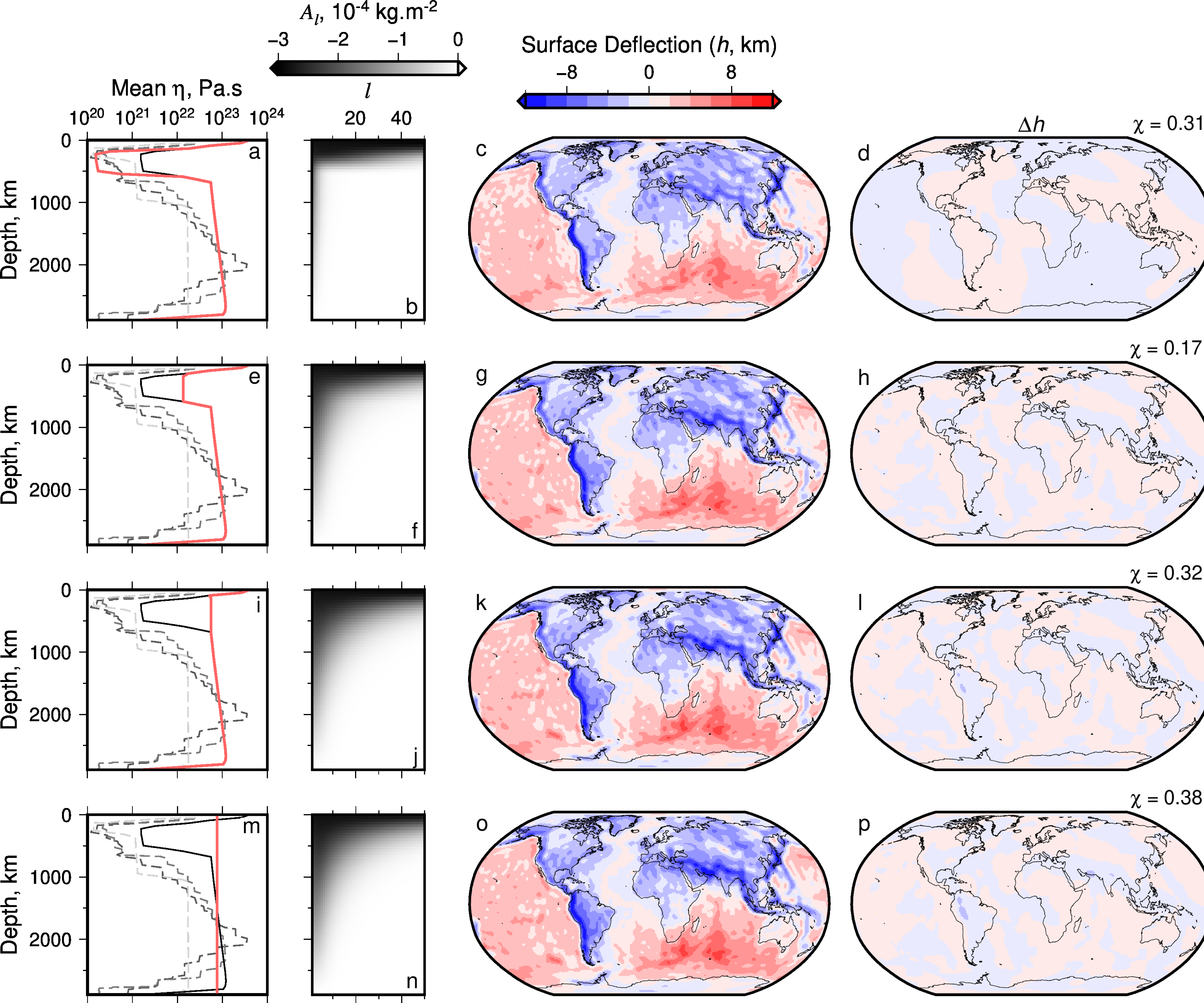

A_l, 10^{-4} kg.m^{-2}
−3 −2 −1 0
l
Surface Deflection (h, km)
−8 0 8
Mean η, Pa.s
10^{20} 10^{21} 10^{22} 10^{23} 10^{24}
20 40
Depth, km
0 1000 2000
a b c d e f g h i j k l m n o p
Δh
χ = 0.31
χ = 0.17
χ = 0.32
χ = 0.38

Figure 18.

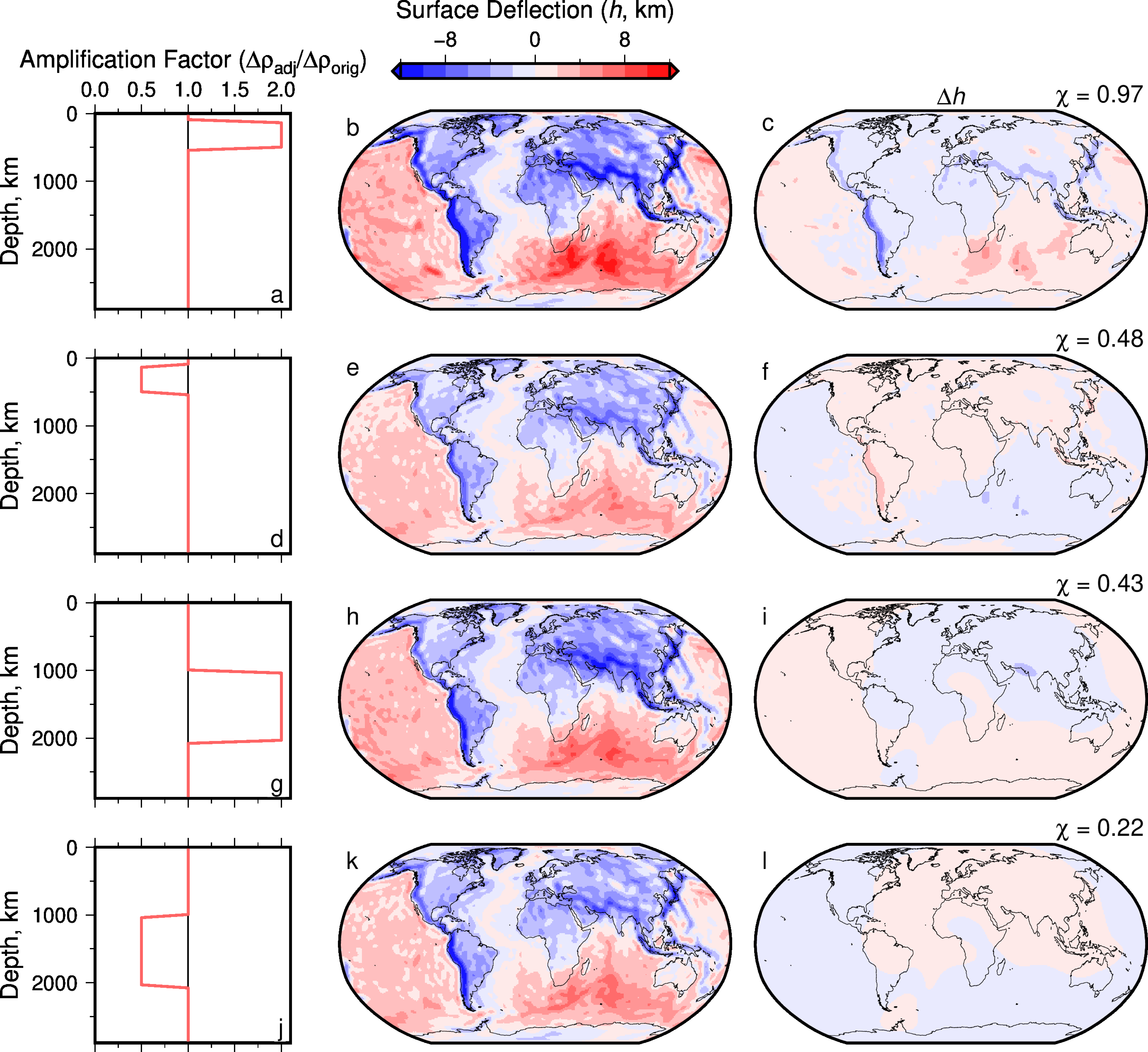

Surface Deflection (h, km)
−8
0
8
Amplification Factor ($\Delta\rho_{adj}/\Delta\rho_{orig}$)
0.0
0.5
1.0
1.5
2.0
Depth, km
0
1000
2000
a
b
c
Δh
χ = 0.97
d
e
f
χ = 0.48
g
h
i
χ = 0.43
j
k
l
χ = 0.22

Figure 19.

z = 45 km
a
z = 135 km
b
z = 360 km
c
z = 1445 km
d
e
Depth, km
2000
1000
0
−9
0
9
Deflection (h, km)
−2
0
2
Contribution to h, km
f
10
0
−10
h, km
g
0°
30°
60°
90°
120°
150°
180°
Angular Distance
|Δρ|, kg/m3
0
15
30
45
0
500
1000
1500
2000
2500
Depth, km
h
0
200
400
600
|Mean contribution to h|, m

Reconciling Surface Deflections From Simulations of Global Mantle Convection

Conor P. B. O'Malley[1], Gareth G. Roberts[1], James Panton[2], Fred D. Richards[1], J. Huw Davies[2], Victoria M. Fernandes[1,3], Sia Ghelichkhan[4]

[1]Department of Earth Science & Engineering, Imperial College London, Royal School of Mines, Prince Consort Road, London SW7 2BP, UK
[2]School of Earth & Environmental Sciences, University of Cardiff, Park Place, Cardiff CF10 3AT, UK
[3]now at Section 4.6 Geomorphology, GFZ Potsdam, Telegrafenberg, 14473 Potsdam, Germany
[4]Research School of Earth Sciences, Australian National University, 142 Mills Road, Acton, ACT 0200, Australia

Key Points:

- Numerical and analytic predictions of surface deflections from mantle convection simulations are compared.
- Impact of gravitation, excising shallow structure, boundary conditions, and different viscosity and density distributions are quantified.
- Calculated effective contributions to surface deflection emphasize dominance of upper mantle structure.

Corresponding author: Conor O'Malley; Gareth Roberts, `c_omalley1@msn.com`; `gareth.roberts@imperial.ac.uk`

Abstract

The modern state of the mantle and its evolution over geological timescales is of widespread importance for the Earth sciences. For instance, it is generally agreed that mantle flow is manifest in topographic and drainage network evolution, glacio-eustasy, volcanism, and in the distribution of sediments. An obvious way to test theoretical understanding of mantle convection is to compare model predictions with independent observations. We take a step towards doing so by exploring sensitivities of theoretical surface deflections generated from a systematic exploration of global mantle convection simulations. Sources of uncertainty, model parameters that are crucial for predicting deflections, and those that are less so, are identified. We start by quantifying similarities and discrepancies between deflections generated using numerical and analytical methods that are ostensibly parameterised to be as-similar-as-possible. Numerical approaches have the advantage of high spatial resolution, and can capture effects of lateral viscosity variations. However, treatment of gravity is often simplified due to computational limitations. Analytic solutions, which leverage propagator matrices, are computationally cheap, easy to replicate, and can employ radial gravitation. However, spherical harmonic expansions used to generate solutions can result in coarser resolution, and the methodology cannot account for lateral viscosity variations. We quantify the impact of these factors for predicting surface deflections. We also examine contributions from radial gravity variations, perturbed gravitational potential, excised upper mantle, and temperature-dependent viscosity, to predicted surface deflections. Finally, we quantify effective contributions from the mantle to surface deflections. The results emphasise the sensitivity of surface deflections to the upper mantle.

Plain Language Summary

Flow of rock within Earth's interior plays a crucial role in evolving the planet. It moves heat and chemicals from deep depths to the surface, for instance. It also moves the lithosphere—the Earth's outer rocky shell—which in turn impacts processes including mountain building, sea-level change, formation of volcanoes, river network evolution, and natural resource distribution. Consequently, we wish to understand the present state, and history, of flowing rock within Earth's interior. Observations exist to address this problem, and mathematics and computing tools can also be used to predict histories of flow and their impact on Earth's surface. We explore how assumptions incorporated into such models affect calculated deflections of Earth's surface. Predictions from different models are compared, with a view to identifying crucial modelling components. Surface sensitivity to deep flow is assessed, demonstrating how surface observations can enlighten flow histories.

1 Introduction

1.1 Background

Mantle convection plays a crucial role in Earth's evolution (e.g., Hager & Clayton, 1989; Parsons & Daly, 1983; Pekeris, 1935). It is well understood, for instance, that flow in the mantle is fundamental in the transfer of heat and chemicals from the deep Earth to the surface, in driving horizontal and vertical lithospheric motions (thus tectonic processes), and in magnetism via interactions with the core (e.g., Biggin et al., 2012; Davies et al., 2023; Foley & Fischer, 2017; Hoggard et al., 2016; Holdt et al., 2022; Pekeris, 1935). In turn, many processes operating at or close to Earth's surface are impacted, including glacio-eustasy, magmatism, climate, sediment routing, natural resource distribution, drainage network evolution, and development of biodiversity (e.g., Ball et al., 2021; Braun, 2010; Hazzard et al., 2022; O'Malley et al., 2021; Salles et al., 2017; Stanley et al., 2021). Clearly, understanding the physical and chemical evolution of the mantle has broad implications. Theoretical approaches to understanding mantle convection, including global simulations of mantle flow, can incorporate complex rheologies and geological histories (e.g., Forte, 2007; Hager & Clayton, 1989; D. P. McKenzie et al., 1974; Ribe, 2007; Ricard, 2007). Such models can include data assimilation, incorporating seismic tomographic (and other data) into flow solutions, iterating to optimize fits to observational constraints (e.g., Bunge et al., 2002, 2003; Glišović & Forte, 2016). A general goal is to identify theoretical models that are most Earth-like and, ultimately, to combine such approaches with observational inventories to provide accurate estimates of the actual history of mantle convection, and its role in governing Earth's surface evolution.

Properties of the convecting mantle, and its role in supporting topography at Earth's surface, have become significantly better known in the last decade or so, thanks principally to two suites of observations. First, there has been notable convergence in seismic tomographic imaging studies of Earth's interior, partly as a result of increased instrumentational coverage (e.g., EarthScope; Lekić & Fischer, 2014). Methodological advances, including full waveform inversion, have also improved understanding of mantle structure in many places (see, e.g., Fichtner et al., 2009, 2013; Fichtner & Villaseñor, 2015; French & Romanowicz, 2015). Mapping lithospheric thicknesses, which are crucial for disentangling origins of surface topography, has benefited from these improvements, as well as their own methodological advances (e.g., Priestley & McKenzie, 2013; F. D. Richards et al., 2021). Second, the inventory of residual oceanic age-depths—oceanic basement depths that cannot be explained by passive plate cooling with age, crustal or sedimentary processes—has become significantly more comprehensive (Davies et al., 2019; Hoggard et al., 2016; Holdt et al., 2022; Menard, 1973). Measured residual depths indicate that the convecting mantle supports oceanic bathymetry with amplitudes up to ~ 1 km, at horizontal scales ranging from those dictated by the elastic strength of the plate, i.e., $O(10^2)$ km, up to $O(10^4)$ km. The spectral power of these deflections approximately matches analytical estimates for mantle flow (e.g., Kaula's rule; Hoggard et al., 2016; Holdt et al., 2022; Kaula, 1963). In contrast, more complex continental rheologies and tectonic histories mean that quantifying modern topographic support of continental lithosphere from the mantle using observations is in its infancy (see, e.g., Davies et al., 2023; Hoggard et al., 2021). However, potential field data (e.g., free-air gravity anomalies and their relationship with topography, the geoid, etc.) and seismological information about plate structure provide useful information to constrain the current state of the convecting mantle beneath continents (and oceans; Audet, 2014; Hager & Clayton, 1989; Steinberger & O'Connell, 1997).

A growing inventory of geological and geomorphological observations from atop passive margins and within continental interiors provides increasingly coherent information about histories of mantle convection during the last ~ 100 Ma (see, e.g., Hoggard et al., 2021, for a recent summary). For instance, pressures and temperatures of melting obtained from the composition of Neogene and younger mafic rocks globally have recently been shown to be broadly consistent with estimates derived from shear wave tomography (Ball et al., 2022). Over-compacted stratigraphy and backstripped subsidence histories along African, American and Australian margins, combined with seismological and gravity data, provide evidence of vertical lithospheric motion due to flow in the mantle (e.g., Al-Hajri et al., 2009; Czarnota et al., 2013; Flament et al., 2015; Morris et al., 2020). Uplifted marine and coastal rock on all continents, especially in regions that have not recently experienced lithospheric shortening, provides information about sub-plate support of topography and mantle viscosity (e.g., Fernandes & Roberts, 2020; Gunnell & Burke, 2008; Lambeck et al., 1998). Lithospheric vertical motions from stratigraphic data (especially uplifted marine rock), from inverse modelling of drainage networks, and from denudation and sedimentary flux histories, provide indirect information about histories of sub-plate support beneath the continents (e.g., Galloway et al., 2011; Fernandes et al., 2019; O'Malley et al., 2021; Stanley et al., 2021). In summary, there now exists a global inventory of geophysical, geological and geomorphological observations, providing information about the current state of the mantle and clues about its spatio-temporal evolution, especially during the last few tens of millions of years.

Despite these advances, observations providing information about the history of mantle convection are sparse in places, especially within continental interiors. Sparsity increases globally back through time (see, e.g., Hoggard et al., 2021). Theoretical or modelling approaches can, in principle, be used to fill in spatio-temporal observational gaps, to quantify the history of mantle convection. A general goal is to combine theoretical insights into mantle convection, e.g., via numerical simulation or analytical advances, with the growing observational inventory. In our view, there are two crucial steps to doing so. First, a quantitative understanding of the implications of modelling choices (e.g., numerical vs. analytical solutions, boundary conditions, rheological assumptions) for predicting quantities that are measurable at Earth's surface (e.g., surface deflections, gravitational potential, heat flow) is required. There now exists a large body of models and theoretical approaches that can be compared. Second, quantification of the discriminatory power of observations at Earth's surface for identifying Earth-like simulations of mantle convection is needed. Our focus in this paper is on addressing the first topic. We then discuss the second topic, with a view to making use of independent observations in future work.

1.2 Approach

A large body of global mantle convection simulators and simulations exist, which can, in principle, be used to fill observational gaps and predict histories of mantle convection (e.g., Baumgardner, 1985; Bunge & Baumgardner, 1995; Davies et al., 2013; Flament et al., 2015; Ghelichkhan et al., 2021; Hager et al., 1985; Moucha & Forte, 2011; Steinberger & Antretter, 2006). This considerable body of existing work provides an opportunity to assess the role different features arising from the natural complexity of mantle convection play in generating surface observables. For instance, mantle convection simulations can incorporate radial and temperature-dependent viscosity, radial gravitation, deflection of gravitational potential fields and their subsequent impact on flow, mineralogical phase changes, compressibility, different surface and core-mantle boundary slip conditions (e.g., rigid/no-slip, free-slip), chemical and thermal buoyancy, and plate motions and/or tomographic constraints on mantle structure (e.g., Baumgardner, 1985; Corrieu et al., 1995; Crameri et al., 2012; Panasyuk et al., 1996; Tackley et al., 1993; Zhong et al., 2008). These assumptions can result in quite different predictions of surface deflections. An obvious question then, which we seek to address, is, can surface observations be used to discriminate between simulations, and, ultimately, to determine the history of mantle convection?

Aside from the fundamental choice of governing equations underpinning simulations, there exist different mathematical and computational approaches to predict the surface impact of mantle convection. These approaches sit within two broad families: numerical simulations (e.g., CitcomS, TERRA, ASPECT; Bangerth et al., 2023; Baumgardner, 1985; Zhong et al., 2000), and propagator matrix based, quasi-analytical techniques, that can be solved in two or three dimensions, and importantly for our purposes, spherically and spectrally (e.g., Parsons & Daly, 1983; Hager & O'Connell, 1979; Colli et al., 2016). Here, we investigate similarities and differences arising between surface deflections predicted by propagator matrix and numerical schemes (see Figure 1). We do so by comparing predictions generated using the numerical code TERRA, and a modified version of Ghelichkhan et al. (2021)'s analytical (propagator matrix) code. We develop a flexible scheme that could be used to compare predictions from other whole-Earth models of mantle convection.

This paper is arranged as follows. First, the conservation equations solved to predict mantle flow and subsequent surface deflections, solution methodologies, and model parameterizations are described. Second, numerical and analytical techniques for estimating surface deflection are summarized. Third, three metrics for comparing predicted surface deflections are described. Fourth, parameterizations and assumptions tested in this paper are described, and resultant modifications to surface deflection predictions are quantified. We start by comparing predictions that arise from as-similar-as-possible parameterizations of numerical and analytical approaches. These tests compare surface deflections calculated using the entirety of the modelling domains, i.e., from the core-mantle boundary (CMB) to the surface; no shallow structure is excised. These reference models are purposefully simple, e.g., incompressible, constant gravitational acceleration (no self-gravitation or radial variation in gravitation), radial viscosity independent of temperature. The convection simulations are driven by plate motions generated using geological observations, which are described below. For clarity, the simulations do not incorporate information about the mantle derived from tomographic models. We then systematically examine the impact of incorporating radial variations in gravitational acceleration, contribution to flow from deflection of the gravitational potential field, removal of shallow density/viscosity structure, choice of surface and CMB slip conditions, inclusion of temperature dependent viscosity, and amplification/reduction of viscosity and density anomalies in the upper and lower mantle. We explore a closed-loop modelling strategy in which predicted surface deflections from these relatively complex models are compared to results from reference models. Finally, a methodology for assessing effective contributions to surface topography from mantle anomalies is presented.

We stress that we purposefully avoid isolating passive or plate-driven surface deflection and sub-plate support from the simulations unless stated explicitly. The central focus of this work is merely on quantifying contrasting predictions of surface topography that arise simply from choices made when simulating mantle convection using numerical and analytical approaches. We compare results to estimates of sub-plate support from oceanic age-depth residuals with a view to quantifying corrections necessary to convert surface deflections predicted by mantle convection simulations into estimates of sub-plate support.

2 Equations Governing Predicted Mantle Convection

Theoretical predictions of surface displacements from mantle convection arise from the application of physical laws that take the form of conservation equations for mass, momentum and energy (see, e.g., Hager & O'Connell, 1981; Parsons & Daly, 1983). Here, we solve those equations across a 3D spherical domain using the finite element code TERRA (Baumgardner, 1985; Bunge & Baumgardner, 1995, etc.). Under this formulation, theoretical convection in an incompressible fluid can be expressed by the following three dimensionless equations (e.g., Baumgardner, 1985; Davies et al., 2013; D. P. McKenzie et al., 1974; Parsons & Daly, 1983). First, the continuity condition for conservation of mass,

$$\nabla \cdot \mathbf{u} = 0, \tag{1}$$

where $\mathbf{u}$ is the fluid velocity vector. Since the Prandtl number is likely to always be extremely large in this system—mantle viscosity is expected to be many orders of magnitude larger than the product of density and thermal diffusivity—inertial terms can be neglected (e.g., Parsons & Daly, 1983). Second, the equation of motion,

$$\nabla \sigma = -\rho' \mathbf{g}, \tag{2}$$

where

$$\rho' = -\alpha \rho_0 (T - T_{\mathrm{ref}}). \tag{3}$$

σ is the 3×3 stress tensor where the (radial) hydrostatic component balancing the reference density structure has been subtracted, ρ' is the density difference due to temperature, α is the coefficient of thermal expansion, T is temperature, T_{ref} is a radially varying reference temperature structure, which has a constant value in the mid-mantle and joins to a cold thermal boundary layer near the surface and a hot one at the CMB, reaching the actual surface, T_s, and core mantle boundary, T_{CMB} temperatures at the respective boundaries, and $\mathbf{g}$ is gravitational acceleration acting radially (see Table 1). This stress tensor σ_{ij} is decomposed into deviatoric and lithostatic components:

$$\sigma_{ij} = \tau_{ij} - p\delta_{ij}, \tag{4}$$

where τ_{ij} is the deviatoric stress tensor, p is dynamic pressure and δ_{ij} is the Kronecker delta function. The deviatoric stress tensor and the strain-rate tensor, $\dot{\epsilon}_{ij}$, are related by:

$$\tau_{ij} = 2\eta\dot{\epsilon}_{ij} = \eta\left(\frac{\partial \mathbf{u}_i}{\partial x_j} + \frac{\partial \mathbf{u}_j}{\partial x_i}\right), \tag{5}$$

where η is viscosity, and $\partial/\partial x_i$ is the spatial partial derivative. By combining equations 2, 4 and 5 we solve the equation of motion:

$$\frac{\partial(\eta\epsilon_{ij})}{\partial x_j} - \frac{\partial p}{\partial x_i} = -\rho' g\delta_{ir}, \tag{6}$$

where g is the scalar value of $\mathbf{g}$ and δ_{ir} is the Kronecker delta selecting the radial direction r.

We first examine predictions from models in which viscosity varies only with depth, i.e., $\eta = \eta_0 \times \eta_r$, where η_0 is reference viscosity (see Table 1), and η_r is a scaling factor dependent only on radius, plotted with model results as appropriate throughout this manuscript. We then include temperature dependence of viscosity, i.e., $\eta = \eta_0 \times \eta_r \times \eta_T$, where

$$\eta_T = \exp(z' - 2T'). \tag{7}$$

Dimensionless depth, $z' = z/d$, where $d = z_{\text{surface}} - z_{\text{CMB}} = 2890$ km, and dimensionless temperature $T' = (T - T_s)/(T_{\text{CMB}} - T_s)$, where $T_{\text{CMB}} - T_s = 2700$ K.

Finally, the heat transport equation is solved to ensure conservation of energy:

$$\frac{\partial T}{\partial t} + \mathbf{u}\cdot\nabla T = \kappa\nabla^2 T + \frac{H}{C_p}, \tag{8}$$

where κ is thermal diffusivity, H is internal heat generation and C_p is specific heat capacity. See Table 1 for parameter values and units. Heat generation within the mantle depends on the distribution of radiogenic isotopes (e.g., Ricard, 2015). Concentrations of such elements can be tracked in TERRA, using particles, varying as a consequence of flow and melting (see, e.g., Panton et al., 2023; van Heck et al., 2016, for full explanation). The bulk composition field, C, which varies between 0 and 1, is also tracked on particles and calculated for each of the finite elements in the model. The end-members represent completely depleted/harzburgitic material ($C = 0$), and fully enriched/basaltic material ($C = 1$). As a result, radiogenic heat production across the whole mantle volume varies, being ≈ 24 TW (5.8×10^{-12} W kg^{-1}) at 1.2 Ga, and ~ 18 TW (4.5×10^{-12}

W kg^{-1}) by 0 Ma. Simulations are initialised such that the average mantle composition is $C = 0.20$ (Panton et al., 2023), and composition obeys the conservation equation:

$$\frac{\partial C}{\partial t} = -\nabla \cdot (C\mathbf{u}). \tag{9}$$

2.1 Numerical Modelling Strategy

The Stokes equations described above are solved by the finite element method on a series of stacked spherical shells composed of nodes based on a subdivision of a regular icosahedron, with an identical geometry for each shell when projected onto the CMB (see, e.g., Figure 1 of Baumgardner, 1985). The radial spacing of consecutive shells is 45 km, which is the same as the mean horizontal spacing of the elements across the entire model domain. The stacking of identically partitioned shells leads to a finer mean horizontal resolution of ≈ 33 km at the CMB, and a coarser resolution of ≈ 60 km at the surface. The surfaces of the uppermost elements in the shallowest shell lie at zero depth. To enable estimates of stress from these models to be directly compared with analytical solutions obtained from Green functions across layer boundaries, the predicted values of deviatoric stress were calculated using the calculated velocities from the nearest shells using the interpolating linear shape functions of the underlying finite elements, while the dynamic pressure is calculated directly at the surface (Section 3.3).

Each numerical model presented in this paper has two computational stages: 'spin-up', which is used to initialize the model, and the geologically more realistic 'main' stage, from which we generate predictions of surface deflections. The spin-up stage includes 2.2 billion years of model run-time. It has the following conditions imposed to avoid sharp velocity and temperature gradients, and sudden reorganization of mantle flow when the main model starts. First, a free-slip condition is imposed at the surface. Second, an initial, random white noise temperature field generated with power across spherical harmonic degrees 1-19, is inserted. Mean mantle temperature is initially 2000 K. Mantle convection arises naturally over the first two billion years of model run-time. A fixed-slip surface velocity condition is then applied to the surface for 200 Ma. These velocities are set to be equal to those at 1 Ga extracted from the reconstructions of Merdith et al. (2021); the vertical component of slip is zero. The resultant mantle structure is used as the initial condition for the main model.

The main model routine predicts flow from 1 Ga to the present-day (0 Ma). It includes an isothermal condition imposed at the surface, $T_s = 300$ K. A fixed-slip condition is imposed such that the vertical component of $\mathbf{u}$ is zero. Horizontal slip is prescribed using the plate reconstructions of Merdith et al. (2021); these are applied in 1 Ma long stages. As such, stirring by plate drift and slab sinking play a role in driving mantle flow in these models. An isothermal condition is also imposed at the core-mantle boundary such that $T_{\mathrm{CMB}} = 3000$ K. A free-slip velocity boundary condition is imposed there, i.e., so the radial component of the mantle flow velocity $(\mathbf{u_r}) = 0$. While this radial velocity boundary condition is of the Dirichlet type, in a free-slip boundary condition no tangential restriction is imposed on the flow velocity but rather on the tangential deviatoric stresses acting on the boundary ($\tau_{r\theta}$, $\tau_{r\phi}$ where r, θ and ϕ are the radial and two tangential directions respectively), which are zero. Horizontal components of slip are allowed to naturally emerge and evolve subject to lowermost mantle flow. Plume behaviour is not artificially suppressed.

To ensure numerical stability and computational accuracy in these simulations, the reference viscosity, η_0, is set to 4×10^{21} Pa s. This value is probably an order of magnitude greater than the viscosity of the actual upper mantle (e.g., Forte, 2007; Ghelichkhan et al., 2021; Mitrovica & Forte, 2004, and references therein). Consequently, flow velocities in the simulations are likely to be significantly slower than in actuality. An obvi-

Table 1. Summary of Model Parameters.

Parameter	Symbol	Value	Units
Surface temperature	T_s	300	K
Core-mantle boundary temperature	T_{CMB}	3000	K
Internal heating rate	H	See text.	W kg^{-1}
Thermal expansivity	α	2.5×10^{-5}	K^{-1}
Thermal conductivity	K	4	W m^{-1}K^{-1}
Thermal diffusivity	κ	8.08×10^{-7}	m^{2}s^{-1}
Specific heat capacity	C_p	1100	J kg^{-1}K^{-1}
Reference viscosity	η_0	4×10^{21}	Pa s
Reference density	ρ_0	4500	kg m^{-3}
Overlying fluid density	ρ_w	1 or 1030	kg m^{-3}

ous cause for concern is that using actual (comparatively fast) plate velocities as surface boundary conditions atop a relatively slowly convecting 'mantle' is likely to induce unrealistic flow. To address this issue, imposed plate velocities are scaled such that the root-mean squared (RMS) values of the actual applied velocities (≈ 5 cm yr^{-1} unscaled) match RMS values of surface velocities (≈ 2.5 cm yr^{-1}) calculated during the spin-up phase (before plate velocities are imposed on the model) when the model mantle is convecting naturally and not being driven by surface velocities. The applied surface plate velocities are therefore scaled by a factor of 0.5 (i.e., 2.5/5) in the simulations examined in this study. To ensure that volumetric fluxes through ridges and subduction zones are realistic, simulation run times are increased by a factor of 2; i.e., the 1 Myr long plate stages are run for twice their elapsed time (2 Myr), but at half the speed. All times stated throughout the rest of this manuscript refer to times re-scaled for real-world comparison; i.e., the actual age of the respective plate stage.

For the reference case (Model 1), these conditions lead to the density distributions shown in Figure 2. Surface layer density anomalies occur only as a result of predicted compositional variation, since the surface temperature, T_s, is constant globally. This model represents the first of two reference numerical models examined in this contribution. It has the radial viscosity structure shown in Figure 3c. Later, we investigate a second numerical model incorporating temperature-dependent viscosity (Equation 7). In the following section, we describe two approaches that use output from these models to calculate instantaneous surface deflections.

3 Numerical and Analytical Calculations of Surface Deflection

We examine two widely used approaches for calculating radial stress, σ_{rr}, and deflections, h, at Earth's surface (Figure 1). First, we investigate numerical solutions obtained using the TERRA software. A methodology for representing this data in the spherical harmonic domain is then described. Secondly, we investigate analytical solutions obtained in the spherical harmonic domain using propagator matrix techniques.

3.1 Numerical Solution

Following Parsons and Daly (1983), surface deformation is estimated from numerical simulations of mantle convection by making use of the requirement that normal stress is continuous across the upper boundary of the solid Earth (see also D. McKenzie, 1977;

Ricard, 2015). In other words, radial stresses generated by the solid Earth are required to be balanced by stresses generated by the overlying (oceanic or atmospheric) fluid. There are three contributions to normal stress at this boundary from the mantle: hydrostatic stress that would exist even in the absence of convection, dynamic stress arising from convection, and viscous stress which opposes fluid motion (see Equations 2–6). To satisfy the continuity condition, these stresses must be balanced by those generated by the water (or air) column atop this boundary. If the pressure from the overlying column is hydrostatic, the resultant condition is

$$\rho_w g_R h = \rho_m g_R h + \sigma_{rr}, \tag{10}$$

where σ_{rr} (defined in Equation 2) incorporates deviatoric viscous stresses generated by mantle convection and dynamic pressure ($\sigma_{rr} = \tau_{rr} - p$), obtained by solving Equation 2. In practice, since values for this term are obtained by subtracting radial lithostatic stress from the total stress, values of σ_{rr} integrate to zero globally. g_R is gravitational acceleration at Earth's surface, ρ_m is the mean density for the surficial layer, and ρ_w is the density of the overlying fluid (see Table 1). Figure 3a-b shows normal stresses, σ_{rr}, calculated at the surface of Model 1, and associated statistics. This model was generated using the viscosity structure shown in Figure 3c. By convention, positive stresses imply compression and hence downward surface deflection, which could be manifest as lithospheric drawdown, i.e., subsidence. Prominent regions of positive stress anomalies in this model include locations atop imposed collision zones, where subduction naturally results, e.g., along the Pacific margin of South America. Negative stresses imply dilation and hence positive lithospheric support (i.e., surface uplift). Figure 3a shows dilatational stresses beneath Southern Africa, for example, and along mid-oceanic ridges in the Indian and Atlantic Oceans. Note that we do not impose additional oceanic plate cooling, e.g., due to hydrothermal circulation at ridges. Cooling and subsequent subsidence, as well as passive return flow at ridges, arise naturally from solution of the governing equations laid out in Section 2.

Surface deflection arising in response to predicted mantle convective flow, h, is approximated by rearranging Equation 10,

$$h \approx -\frac{\sigma_{rr}}{(\rho_m - \rho_w) g_s}, \tag{11}$$

where g_s is gravitational acceleration at the surface, here = 10 m s^{-2}. In this application of TERRA, surface deflections are estimated from radial stresses at times of interest (e.g., the present-day) by re-running one time-step of the model. During that time, a free-slip boundary condition, for which analytical approximations for surface deflection exist, is imposed instead of the plate-slip condition prescribed during the main model run routine (see Section 3.3; Ricard, 2015). We assess the accuracy of modifying boundary conditions in this way by converting calculated deflections into the spherical harmonic domain and comparing them to predictions generated from the analytical propagator matrix (Figure 3d–f). The consistent boundary flux (CBF) method provides an alternative means to accurately calculate normal stresses (Zhong et al., 1993). Previous benchmarking with TERRA has shown mean errors of a few percent or less for surface deflection predictions at low harmonic degrees, $l \leq 16$ (Davies et al., 2013).

3.2 Spherical Harmonic Representation of Surface Deflection

Transforming stress, or surface deflections, calculated using numerical approaches into the frequency domain provides a means of quantifying their spectral power, i.e., the magnitude of contribution to the total signal from different wavelengths. We do so using spherical harmonics, since the models that we investigate are global in scope. Any real, square-integrable function over the surface of the Earth can be described as a function of longitude θ and latitude ϕ by a linear combination of spherical harmonics of degree l and order m,

$$f(\theta,\phi) = \sum_{l=1}^{L} \sum_{m=-l}^{l} f_{lm} Y_{lm}(\theta,\phi). \tag{12}$$

The spherical harmonic functions Y_{lm} are the natural orthogonal set of basis functions on the sphere, and f_{lm} are the spherical harmonic coefficients. As an example, Figure 3d shows spherical harmonic expansion of the surface stress field predicted by Model 1 at 0 Ma (cf. Figure 3a). We call this result Model 1b, and the original, full-resolution numerical result Model 1a. The fidelity of the spherical harmonic expansion is demonstrated by the similarity of the maps and histograms shown in panels a–b and d–e.

$$P_l = \sum_{m=-l}^{l} f_{lm}^2 \tag{13}$$

gives the total power across all spherical harmonics of a given degree l. Average power for each mode m within degree l, $\hat{P}_l = P_l/(2l+1)$, since there are $2l+1$ modes (orders) per degree—we do not explore this definition of power in this contribution, and present only total power per degree (see, e.g., Hoggard et al., 2016; Holdt et al., 2022). Figure 3f shows power as a function of degree under that convention from the expansion shown in panel d. Using the total power per degree convention, Hoggard et al. (2016) (their Supporting Information) derived a rule-of-thumb for estimating the power spectrum of dynamic topography, P_l^{DT}, using Kaula (1963)'s approximation for the long-wavelength gravity field of Earth as a function of l:

$$P_l^{DT} \approx \left(\frac{GM}{ZR^2}\right)^2 \left(\frac{2}{l} - \frac{3}{l^2} + \frac{1}{l^4}\right), \tag{14}$$

where G is the gravitational constant, $M = 5.97 \times 10^{24}$ kg is the mass of the Earth, $R \approx 6370$ km is Earth's radius, and long-wavelength admittance between gravity and topography $Z = 12$ mGal km^{-1}, which we make use of in the remainder of the paper for reference. Although we acknowledge that the appropriate value of low-degree admittance varies as a function of Earth's viscosity profile, and the depth and wavelength of its internal density anomalies (Colli et al., 2016), previous studies have found that assuming an average value of 12 mGal km^{-1} provides a reasonable approximation of observed residual topographic trends (Hoggard et al., 2016).

Finally, it is useful to note that Jeans (1923) related spherical harmonic degree to wavelength λ on Earth's surface via,

$$\lambda \approx \frac{2\pi R}{\sqrt{l(l+1)}}. \tag{15}$$

3.3 Analytical Solutions

The second methodology used to calculate surface deflection in response to mantle convection is the analytical propagator matrix technique (e.g., Craig & McKenzie, 1987; Gantmacher, 1959; Ghelichkhan et al., 2021; Parsons & Daly, 1983; M. A. Richards & Hager, 1984). The approach we take stems from the work of Hager and O'Connell (1981). They used Green's functions to solve the equations of motion in the spherical harmonic domain. Those solutions are used to generate sensitivity kernels that straightforwardly relate, for example, density or temperature anomalies in the mantle to surface deflections.

The kernels are generated in the frequency domain, and constructed such that surface deflection sensitivity to mantle (e.g., density) anomalies is calculated as a function of depth (or radius) and wavenumber. A global spherical harmonic implementation introduced by Hager et al. (1985) has been extended to include compressibility, the effect of warping of the gravitational potential by subsurface density distributions, and radial gravity variations calculated using radial mean density values (Corrieu et al., 1995; Forte & Peltier, 1991; Hager & O'Connell, 1981; M. A. Richards & Hager, 1984; Thoraval et al., 1994).

In this study, following Ghelichkhan et al. (2021), surface deflection for each spherical harmonic coefficient, h_{lm}, is calculated in the spectral domain such that

$$h_{lm} = \frac{1}{(\rho_m - \rho_w)} \int_{R_{\mathrm{CMB}}}^{R} A_l \delta\rho_{lm}(r) \cdot \mathrm{d}r. \tag{16}$$

Products of the sensitivity kernel, A_l, and density anomalies, $\delta\rho_{lm}$, of spherical harmonic degree, l, and order, m, are integrated with respect to radius, r, between the core-mantle boundary and Earth's surface radii, R_{CMB} and R, respectively. The sensitivity kernel is given by

$$A_l = -\left(\frac{\eta_0}{R g_R}\right)\left(u_1 + \frac{\rho_w}{\rho_0} u_3\right), \tag{17}$$

where $u_n(r)$ represents a set of poloidal variables, which are posed for solution of the set of simultaneous equations by matrix manipulation, such that

$$u(r) = \begin{bmatrix} y_1\eta_0 & y_2\eta_0\Lambda & (y_3 + \bar{\rho}(r)y_5)r & y_4 r\Lambda & y_5 r\rho_0\Lambda & y_6 r^2\rho_0 \end{bmatrix}^T, \tag{18}$$

where $\Lambda = \sqrt{l(l+1)}$, and y_1 to y_6 represent the spherical harmonic coefficients of radial velocity v_r, lateral velocity $v_{\theta,\phi}$, radial stress σ_{rr}, lateral stress $\sigma_{r\theta,\phi}$, gravitational potential V, and gravitational potential gradient $\partial V/\partial r$, respectively (Hager & Clayton, 1989; Panasyuk et al., 1996). $\bar{\rho}$ is the layer mean ($l = 0$) density. The kernel A_l comprises both u_1 and u_3, since those are the two terms in the matrix solution to the governing equations which affect surface topography, by directly exerting stress on the surface boundary (u_1), and by changing the gravitational potential at the surface (u_3).

The functional forms of calculated sensitivity kernels depend on chosen radial viscosity profiles and boundary conditions (e.g., free-slip or rigid; Parsons & Daly, 1983). Figure 5a and e show examples of sensitivity kernels generated for water- ($\rho_w = 1030$ kg /m^3), and air-loaded ($\rho_w = 1$ kg /m^3) topography, with free-slip conditions imposed on both surface and lower boundaries. We investigate alternative slip boundary conditions for each surface later in the text. The kernels were generated using the radial viscosity profile shown in Figure 3c. Values of the other parameters used to generate these kernels are stated in Table 1. We limit our investigation to $l \leq 50$, which corresponds to a horizontal wavelength λ of $\approx$ 792 km at Earth's surface. Calculated present-day water- and air-loaded surface deflections, and their statistical properties, are shown in Figure 5b–d and f–h. A comparison of calculated power spectra, expected surface deflection from Kaula's rule (Equation 14), and spectra generated from observed residual ocean age-depth measurements is also included (Kaula, 1963; Hoggard et al., 2016; Holdt et al., 2022). In later sections we explore consequences of choosing different radial viscosity profiles for calculated kernels and thence surface deflections. We call this water-loaded analytical solution for surface deflection 'Model 2' (see Table 2). It represents the closest possible analytical solution for surface deflection predicted numerically by Model 1 explored in this work.

4 Spatial and Spectral Comparison of Model Predictions

We wish to quantify impacts of modelling assumptions and approaches, used to solve the equations of motion, on predicted surface deflections. Thus we compare calculated surface deflections (both numeric and analytical) using the following three metrics.

4.1 Euclidean Comparisons of Amplitudes

First, we calculate root-mean-squared difference, χ, between predicted surface deflections in the spatial domain,

$$\chi = \sqrt{\frac{1}{N}\sum_{n=1}^{N} w_\phi \left(h_n^a - h_n^b\right)^2}, \tag{19}$$

where h_n^a and h_n^b are predicted surface deflections from the two models being compared. N = number of points in the $1{\times}1^\circ$ gridded maps being compared (e.g., Figure 5b; N = 65341). The prefactor w_ϕ is proportional to $\cos\phi$, where ϕ is latitude, and is included to correct biases in cell size with latitude; mean $w_\phi = 1$. This metric is closely associated with the mean vertical distance (L^2-norm distance) between predicted and reference surfaces, i.e., $\Delta\bar{h} = 1/N \sum_{n=1}^{N} w_\phi |h_n^a - h_n^b|$. These metrics are sensitive to differences in amplitudes and locations of surface deflections.

4.2 Spectral Correlation Coefficients

Second, we use pyshtools v4.10 to compute correlation coefficients, r_l, between predicted surface deflections in the spectral domain (Wieczorek & Meschede, 2018). Correlation coefficients as a function of degree l, adapted from Forte (2007), are calculated such that

$$r_l = \frac{\sum f_1^* f_2}{\sqrt{\sum f_1^* f_1}\sqrt{\sum f_2^* f_2}}, \quad \text{where} \quad \sum = \sum_{m=-l}^{+l}, \tag{20}$$

f_1 and f_2 are the spherical harmonic coefficients of the two fields (i.e., surface deflections) being compared, which vary as a function of m and l; $f = f_l^m$. * indicates complex conjugation (see also Becker & Boschi, 2002; O'Connell, 1971). This metric is a function of degree l, i.e. $r_l = r(l)$, and is sensitive to the difference between predicted and reference surface deflection signals in the frequency domain, but not to their amplitudes. To summarize spectral similarity between models concisely, we later refer to the mean value of r_l over every degree (0–50), as $\bar{r}_l$. We refer to the standard deviation of r_l across degrees as s_r.

4.3 Comparing Calculated Power Spectra

Lastly, to estimate closeness of fit between power spectra of surface deflections predicted in this study and independent estimates, we calculate

$$\chi_p = \sqrt{\frac{1}{L}\sum_{l=1}^{L}\left(\log_{10}P_l - \log_{10}P_l^K\right)^2} + \sqrt{\frac{1}{L}\sum_{l=1}^{L}\left(\log_{10}P_l - \log_{10}P_l^H\right)^2}, \tag{21}$$

where L = number of spherical harmonic degrees being compared ($L = 50$). P_l = power of predicted surface deflections generated in this study at degrees $1 \leq l \leq L$ (Equation 13). P_l^K = power of surface deflections estimated using Kaula's law (assuming Z =

12 mGal km^{-1}; Equation 14). P_l^H = power of residual oceanic age-depth measurements from Holdt et al. (2022).

5 Model Parameterizations and Comparison of Predictions

The models examined in this paper are summarised in Table 2. In terms of assumptions tested there are two families of models, those with viscosity independent of temperature (Models 1–10), and those with temperature-dependent viscosity (Models 11–20). The two approaches used to solve the equations of motion are annotated 'Numerical' and 'Analytical' in Table 2, which refers to solutions from the TERRA and propagator matrix code, respectively. Viscosities and densities calculated using TERRA were used as input for the propagator matrix code and thus used to generate analytical estimates of surface deflection. Since analytical solutions are obtained by spherical harmonic expansion, surface deflections from TERRA were fit using spherical harmonics before predicted deflections were compared (annotated 'Mixed' in Table 2; Section 3.2). We compare predicted deflections that arise from flow across entire model domains, i.e., from the CMB to the surface. We make no lithospheric corrections, unless explicitly stated. Thus, amplitudes of calculated surface deflections are not likely to represent actual residual topography. However, it simplifies like-for-like comparison of models, and comparisons to increasingly complex models. Comparisons of surface deflections predicted by these models are discussed in the following sections, with summary statistics given in Table 3.

5.1 Models 1–10: Viscosity Independent of Temperature

Models 1–10 show results generated when viscosity is independent of temperature. We first compare solutions generated from (reference) numerical and analytical models designed to be as similar as possible (Models 1 and 2). We then generate increasingly complex models—incorporating radial gravitation, gravitational potential energy, removal of shallow structure, and variable surface and CMB slip conditions—and compare predicted surface deflections to the reference models.

Reference Models 1–2

Models 1 and 2 are the simplest models explored in this paper. They were designed to be as similar as possible, with a view to quantifying differences and similarities arising solely from the choice of methodology (numerical or analytical) used to solve equations of motion and to calculate surface deflections. Viscosity is independent of temperature in these models.

Figure 2 shows calculated densities that arise from the numerical solutions (Model 1). This figure shows the plate motion history from Merdith et al. (2021) used to produce this (and subsequent) TERRA output (See Section 2.1). The maps and histograms show evolution (100 to 0 Ma) of calculated densities at the model's surface and within its 'asthenosphere' in response to flow. This model was parameterized with the radial viscosity shown in Figure 3c; radial viscosity used in other geodynamic studies are shown alongside for comparison (Ghelichkhan et al., 2021; Mitrovica & Forte, 2004; Steinberger & Calderwood, 2006). The impact of varying viscosity on numerical solutions is explored later in the paper. Figure 3a shows resultant surface radial stress predicted by this model at full (numerical) resolution. Figure 3d–e show the results from fitting radial stresses generated by Model 1a with a global spherical harmonic interpolation up to maximum degree $l = 50$, i.e., minimum wavelength of ≈ 800 km (Section 3.2). The resultant power spectrum in terms of total power at each degree is shown in Figure 3f. It is approximately

Table 2. Summary of mantle convection simulations. Column labeled 'Method' indicates surface deflections calculated using either '*Numerical*' (i.e., from surface normal stresses calculated using TERRA) or '*Analytical*' (i.e., propagator matrix) approaches; '*Mixed*' indicates spherical harmonic fitting of surface stresses calculated using numerical code, enabling comparison with solutions to propagator matrix code. $\eta(r)$ indicates models with radial viscosity, independent of temperature (Models 1–10). $\eta(r, T)$ indicates models with temperature-dependent (therefore laterally-varying) viscosity (Models 11–20); note that analytical Models 12–20 incorporate radial viscosity calculated using mean radial viscosity from Model 11a. †indicates with respect to Model 12. See Table 2, Section 5 and figures referred to in column 5 for details.

Model	Method	Viscosity	Parameterizations	Figures
1a	Numerical	$\eta(r)$	Full resolution numerical model	2–4
1b	Mixed	$\eta(r)$	Spherical harmonic fit to 1a	2–4, 6
2	Analytical	$\eta(r)$	Propagator matrix solutions	5–6
3	Analytical	$\eta(r)$	Radial gravitation, $g(r)$	7
4	Analytical	$\eta(r)$	Gravitational potential terms	8
5	Analytical	$\eta(r)$	Removing upper 50 km of mantle	9a-d
6	Analytical	$\eta(r)$	Removing upper 100 km of mantle	9e-h
7	Analytical	$\eta(r)$	Removing upper 200 km of mantle	9i-l
8	Analytical	$\eta(r)$	Rigid surface, free CMB	10a-d
9	Analytical	$\eta(r)$	Free surface, rigid CMB	10e-h
10	Analytical	$\eta(r)$	Rigid surface, rigid CMB	10i-l
11a	Numerical	$\eta(r, T)$	Full resolution numerical model	11–13, 16a-c
11b	Mixed	$\eta(r, T)$	Spherical harmonic fit to 11a	11–13, 15, 16d-g
12	Analytical	$\eta(r)$	Mean radial $\eta(r, T)$ from Model 11a	14–16h-k
13	Analytical	$\eta(r)$	Decrease† radial upper mantle η	17a-d
14	Analytical	$\eta(r)$	Increase† radial upper mantle η	17e-h
15	Analytical	$\eta(r)$	Increase† radial upper mantle η	17i-l
16	Analytical	$\eta(r)$	Constant radial η	17m-p
17	Analytical	$\eta(r)$	Upper mantle densities $\times 2^\dagger$	18a-c
18	Analytical	$\eta(r)$	Upper mantle densities $\times 1/2^\dagger$	18d-f
19	Analytical	$\eta(r)$	Lower mantle densities $\times 2^\dagger$	18g-i
20	Analytical	$\eta(r)$	Lower mantle densities $\times 1/2^\dagger$	18j-l

characterized by red noise, where (aside from the lack of structure at degree 0), amplitudes of stress variations decrease steadily with increasing spherical harmonic degree (i.e., decreasing wavelength).

Surface deflections calculated by converting stress into dynamic topography using Equation 11, assuming water-loading, are shown in Figure 4a (Model 1a: full numerical resolution). Spherical harmonic interpolation up to $l = 50$ (Model 1b) is shown in panel b, the histograms in panels c and d summarise results. Resultant spectral power is compared to spectra generated using Kaula's rule (Equations 13 and 14) and residuals from ocean age-depth anomalies are shown in panel e (see Section 4; Equation 21). Surface deflections calculated assuming air-loading are shown in Figures 4f-j.

Figure 5a–d shows analytical solutions (Model 2) to the equations of motion generated using the propagator matrix approach parameterised to be as similar as possible to (the numerical) Model 1. The sensitivity kernel generated using the radial viscosity shown in Figure 3c and free-slip surface and CMB boundary conditions is shown in panel a. Similar to many previous studies, the kernel indicates that surface deflections will be especially sensitive (across all degrees incorporated, $l \leq 50$) to density anomalies in the upper mantle (Parsons & Daly, 1983; Hager & Clayton, 1989; Ghelichkhan et al., 2021). Modifications to sensitivity kernels and resultant surface deflections as a consequence of choosing alternative boundary conditions and viscosity profiles are explored later in the manuscript. From this point forward we only present water-loaded surface deflections, since they scale linearly with air-loaded results.

Comparisons of surface deflections predicted by Models 1b and 2 are shown in Figure 6. Predicted deflections are visually similar (cf. panels a and b). Absolute differences in amplitudes are greatest close to subduction zones (e.g., in South America and Asia; panel c). Differences are broadly normally distributed and centred on 0 (panel d). Note the comparisons shown in panel d are weighted by the cosine of latitude to avoid latitudinal biases, as described in Section 4.1. Figure 6e shows that the spherical harmonic correlation between numerical (strictly '*Mixed*', i.e., spherical harmonic fit to numerical solution) and analytical solutions is high (close to 1 for all degrees; cf. Forte, 2007). Panel f shows ratios between predictions, which indicates that analytical solutions tend to be damped compared to numerical solutions. This result is emphasised by the histogram shown in panel g, which summarises the ratios between predictions. Adjusting surface deflections from the propagator matrix solutions by a factor of 1.1 brings them in-line with the numerical solutions. In other words, the propagator matrix approach dampens solutions by $\approx 10\%$. We note that power spectral slopes between Model 1b and 2 are similar, however (cf. Figures 4e and 5d). This smoothness of analytic solutions, and subsequent damping of topographic amplitudes, is perhaps surprising, given the fact that they are being compared with numerical models expanded into the spherical harmonic domain to the same maximum degree, $l = 50$. However, the surface stresses used to generate Model 1a have full horizontal resolution (≈ 45 km) across depths, and *only* the surface layer is smoothed by spherical harmonic fitting, to generate Model 1b. Therefore, Model 1b inherently contains some contribution from degrees ≥ 50, in the sense that finer-resolution density structure at depth could affect longer-wavelength flow nearer the surface. In contrast, to generate the analytic solution (Model 2), the density structure of each layer of the model is smoothed by expansion to maximum $l = 50$, *before* integration of their contributions to surface deflection. The analytical solution would provide a better match to stress estimates from numerical models if such estimates were calculated using density structure smoothed to the same maximum l across all depths.

We now have reference models with which we can quantify the consequences of incorporating alternative assumptions for calculated surface deflections. We start by incorporating more complex parameterization of gravitation.

Model 3: Radial Gravitation

Figure 7a shows solutions for the analytical Model 3, which was parameterized in the same way as Model 2 with the addition of radial gravitation (following Hager & Clayton, 1989; Panasyuk et al., 1996, see Equation 17). The solid curve in panel b shows the radial gravity function used to calculate surface deflections. It was generated using the density distribution produced by (the numerical) Model 1a (see Figure 2), using

$$g(r) = \frac{4\pi G}{r^2}\left[\int_{R_{\mathrm{CMB}}}^{r} \bar{\rho}(r')\, r'^2\, \mathrm{d}r'\right] + F_{core} \tag{22}$$

where $\bar{\rho}(r)$ is layer mean density and F is a factor chosen to account for core mass, and such that $g = 9.8$ m s^{-2} at the surface. This formulation is derived from Gauss's law assuming spherically symmetric density, combined with Newton's law of universal gravitation (Turcotte & Schubert, 2002).

The differences between Model 2 (Figure 7c), which assumes constant $g = 10$ m s^{-2} across all radii, and this model (Model 3) are shown in Figure 7d–e. We interpret the broadly hemispherical, uniformly distributed, differences in calculated deflections as a consequence of deviations in g between the two models being greatest in the mid-mantle ($\sim 500 - 2000$ km depth; see panel b). Note that the sensitivity kernel calculated for the viscosity structure used in these models indicates that changing g in this way is likely to impact surface deflections at low degrees $l \lesssim 10$ most, i.e., where the amplitudes of the sensitivity kernel in the mid-mantle are highest (see Figures 3c & 5a). Note that the amplitudes of deviations in predicted surface topography due to radial variations in g are relatively low, at most of the order $\sim 10\%$ of maximum surface deflection amplitudes, for the instantaneous analytical solution (see Table 3). Differences in predicted surface deflection are likely to be larger between Model 2 and a numerical model which was run using $g(r)$ calculated at each time-step, since in that case radially-varying gravitation would affect the mantle flow field across the entire model run time and differences would compound. Without additional numerical tests it is somewhat unclear whether the differences between that model and Model 2 would match the results for Model 3 (as a function of degree). However, the results are consistent with the rule of thumb outlined in Section 7.02.2.5.2 of Ricard (2015), whereby magnitudes of differences incurred by inclusion of full self-gravitation, i.e., $g(\theta, \phi, r)$, decay as a function of spherical harmonic degree, proportionately to $3/(2l + 1)$.

Model 4: Gravitational Potential Field Deflection

Figure 8 compares analytical solutions for the reference Model 2, and a model that incorporates stress perturbations induced by deflections of the gravitational potential field, Model 4. Both of these models assume $g = 10$ m s^{-2} everywhere, even within the deflected surface layer, as was the case for Models 1–2. Following Hager and Clayton (1989) and Panasyuk et al. (1996), when solving for surface deflection using propagator matrices, the effect on flow of perturbation of gravitational potential is included via the u_3 term in Equation 18 (see also Ribe, 2007; Ricard, 2015). TERRA simulations do not include this component in flow calculations (see Section 2–2.1). As expected, differences in surface displacement predictions are much lower than when radial gravitation is incorporated (cf. Figures 7d and 8c); they are of the same order of magnitude as the geoid height anomalies predicted by these models. The mean Euclidean distance between the two predicted surfaces is only $\sim$110 m, and the spherical harmonic correlation is very high across all degrees (see Table 3). Similar to the result for Model 3, the differences are concentrated at low spherical harmonic degree l. Again, this test investigates the effect of the u_3 term on instantaneous solution for surface deflection. It cannot be ruled out from this test that inclusion of the effect of gravitational potential field perturbation would result in greater differences across the entire model run time, although that is unlikely (Zhong et al., 2008).

Models 5–7: Removal of Shallow Structure

Disentangling contributions to Earth's surface topography from asthenospheric convection and the lithosphere is not trivial (see, e.g., Fernandes & Roberts, 2020; Hoggard et al., 2021; Steinberger, 2016; Stephenson et al., 2021). Previous studies that simulate mantle convection have addressed this issue by discarding density anomalies in radial shells shallower than specified depths, before calculating surface stresses (e.g., Spasojevic & Gurnis, 2012; Flament et al., 2013; Molnar et al., 2015). Similarly, analytical approaches have isolated contributions from the convecting mantle by only incorporating information from deep shells (e.g., Colli et al., 2018). This method has the advantage of effectively removing the effect of lithospheric cooling through time from surface deflection estimates. It also avoids the need to incorporate, say, realistic crustal or depleted lithospheric layers within the viscous flow parameterization. However, uncertain oceanic and continental lithospheric thicknesses mean that choosing appropriate cut-off depths is not trivial. Moreover, doing so creates two obvious challenges.

First, if the chosen depth is shallower than the lithosphere-asthenosphere boundary in places, plate and sub-plate contributions to topography will be entangled. Second, discarding deeper layers to ensure that all plate contribution is definitely avoided means that some contributions from asthenospheric flow will be missed. Calculated sensitivity kernels indicate that shallow asthenospheric density anomalies make significant contributions to surface topography (Figure 5). Thus, such a step is unlikely to be desirable if mantle flow models are to be used to understand, say, lithospheric vertical motions, or vice versa (see e.g., Figure 5a, e; Davies et al., 2019; Hoggard et al., 2016). Given the calculated sensitivity kernels, excising layers in the upper few 100 km is likely to result in predictions of surface deflections that are especially fraught at short wavelengths, i.e., high spherical harmonic degree. An alternative approach, which avoids some of these issues, is removal of structure based on appropriately calibrated plate models, or globally-averaged age-dependent density trends (e.g., F. D. Richards et al., 2020, 2023).

To quantify the impact of discarding shallow structure, we examine differences in calculated surface deflection in the spatial and spherical harmonic domains. We present three tests, resulting in Models 5, 6 and 7, where progressively deeper structure is removed from Model 2. Figure 9 shows the results of removing contributions to surface deflection from density anomalies at depths shallower than 50, 100 and 200 km. As expected from examination of surface topographic sensitivity kernels (e.g., Figure 5a, e), removal of these layers results in significantly reduced surface topographic amplitudes. Doing so results in power spectra that more closely align with independent estimates (Figure 9b, f, j). The reduction in differences between amplitudes of calculated and observed spectral power is largely due to the fact that the reference model (i.e., Model 2) overestimates dynamic topographic power across all degrees. We note that power spectral slopes for predicted surface deflection from Model 2 are close to those generated from Kaula's rule, and observed oceanic residual depths (Figure 4 and 5). However, removing shallow structure steepens spectral slopes (i.e., reduces power at high degrees) beyond those expected from theoretical considerations (i.e., Kaula's rule) or observed (i.e., from oceanic residual depths), akin to results from other work that excised shallow structure (e.g., Flament et al., 2013; Moucha et al., 2008; Steinberger, 2007). This result is emphasized by the slope of calculated spectral coherence, r_l, between deflections with and without shallow structure removed (Figure 9d, h, l). While degree 1 and 2 structure remains coherent, coherence across degrees $\gtrsim$ 20 decreases from $\sim$ 0.9 to as low as 0.5, which are the largest discrepancies between any models examined in this study.

Models 8–10: Adjusted Slip Boundary Conditions

Up to now, we have only considered instantaneous analytical and numerical solutions for surface deflection where both the surface and CMB have free-slip conditions imposed (i.e., vertical component of flow velocity $\mathbf{u_r} = 0$, horizontal components are allowed to freely vary). No gradient/Neumann constraint (e.g., on $\partial\mathbf{u}/\partial z$) is imposed. This condition is generally deemed appropriate for the surface of the convecting mantle, and CMB, since at both boundaries, cohesion within convecting mantle is thought to be much stronger than adhesion to the boundary. Analytical solutions for sensitivity kernels for propagator matrices also exist for rigid boundaries, i.e., no-slip Dirichlet conditions, where horizontal components of $\mathbf{u} = 0$, which may be more appropriate when the Earth's lithosphere is implicitly included in mantle convection models, as is the case here (Parsons & Daly, 1983; Thoraval & Richards, 1997). Therefore, we test the effect on predicted surface deflections of changing the surface boundary condition to no-slip. Although there is little reason to believe the adhesion of the CMB would be strong, we also test a rigid CMB for completeness. The numerical models themselves are driven by a quasi-rigid condition, whereby flow is driven by estimates of real plate velocities from (Merdith et al., 2021), and so the surface layers behave as a series of rigid, laterally mobile plates rather than a single rigid shell. This approach may be appropriate for driving near-surface (lithospheric) flow throughout the main model run time, but it less clear whether no- or free-slip boundary conditions are most appropriate for calculating instantaneous dynamic topography (see, e.g., Forte & Peltier, 1994; Thoraval & Richards, 1997).

Figure 10a, e and i show predicted sensitivity kernels as a function of depth and degree (l), for no-slip/free-slip, free-slip/no-slip and no-slip/no-slip boundaries respectively, where the first condition is the surface slip condition, and the second the CMB slip condition. Differences to the original sensitivity kernel for Model 2 (Figure 5a) are shown in panels c, g and k. Those panels demonstrate that when the surface boundary condition is rigid, there is decreased sensitivity to short wavelength shallow structure, and increased sensitivity to long-wavelength (low degree) structure across all depths. Figure 10d, h and l reveal that induced misfit in the spatial domain is impacted to a greater degree than in tests of gravitation (Models 3 & 4), but not necessarily more severely than for removal of, say the upper 200 km of density structure from surface deflection calculations. Spectral correlation is most severely impacted when both surface and CMB boundaries are rigid (Model 7; see Table 3).

5.2 Reference Models 11–12: Temperature-Dependent Viscosity

In this section, we investigate the impact of including the temperature dependence of viscosity, $\eta(r, T)$, on predicted global mantle flow in numerical models, and on subsequent estimates of surface deflection. We do so by first presenting results for the numerical Model 11, which is identical to Model 1 in terms of all boundary conditions, initialization, and physical parameters, except for the fact that viscosity depends on temperature in the manner described by Equation 7. The analytical propagator matrix approaches used in this study require that viscosity varies only as a function of radius. In other words, they cannot incorporate temperature-dependent viscosity directly. So, instead we insert layer mean viscosity from the present-day 3D temperature-dependent viscosity structure predicted by numerical models (Figure 11), and use it to generate the analytical Model 12. The role of upper and lower mantle viscosity and density anomalies in determining surface deflections are then examined. For tests resulting in Models 3–10, analytical instantaneous solutions for surface deflection with adjusted parameters and boundary conditions were simply compared with Model 2, and no new numerical models were generated using TERRA. In contrast, this section corresponds to a new model generated using TERRA, where temperature dependence of viscosity affected global mantle flow across the entire run time (Model 11).

Figure 11 shows maps of calculated viscosity in the upper and lower mantle for Model 11. Results, at full horizontal resolution, from the numerical Model 11a are shown in panels a, e, i, m. A slice through this three-dimensional viscosity structure is shown in Figure 1c. Spherical harmonic interpolation of these results, up to maximum degree l = 50, are shown in panels d, h, l and p (Model 11b). Viscosity variation shown in these maps is expressed as percentage deviation from layer mean. Histograms summarising the distribution of viscosity in Model 11a are also shown, alongside radial mean values and extrema. Figure 12 shows the spatio-temporal (100 to 0 Ma) evolution of calculated densities in Model 11a at the surface of the model and within its 'asthenosphere', alongside summary statistics. Density anomalies are more localised ('sharper') than in Model 1, which is unsurprising since temperature-dependent viscosity provides stronger mechanical constrasts between cooler subducting regions and surrounding asthenosphere, when compared to models that do not include temperature-dependent viscosity (cf. Figure 2 Zhong et al., 2000).

Figure 13a-b shows calculated radial normal stresses from Model 11a and their spherical harmonic representation (Model 11b). Summary statistics and calculated power spectra are shown in panels c-d. Panels f-g show calculated water-loaded surface deflections for the full resolution numerical model and for the 'Mixed' spherical harmonic representation (Equation 11). Panels h-j show summary statistics and power spectra as a function of degree, alongside Kaula's rule and an independent estimate of sub-plate support from residual oceanic age-depth measurements (see Section 4). Figure 14 shows surface deflections calculated analytically (Model 12) using layer-mean (radial) viscosity shown in Figure 11c, which was extracted from the numerical Model 11a. Panels a-d show the resultant sensitivity kernel, water-loaded deflections and summary statistics (cf. Figure 5a-d). Air-loaded predictions are shown for Model 12 for reference, in Figure 14e–h, but not included in any summary statistics or future figures, for consistency with previous sections.

Figure 15 compares predictions from the numerical (Model 11b) and analytical (Model 12) schemes incorporating temperature-dependent viscosity, as discussed in the preceding sections. Similar to the results obtained for models without temperature-dependent viscosity (Figure 6), surface deflections calculated using the analytical approach are damped relative to numerical solutions (in their spherical harmonic form; see Figure 15f). The best fit amplification factor to align propagator matrix and numerical solutions is 1.24 (24%), larger than the adjustment required to align reference Models 1b and 2 (1.1; 10%). Similar to our interpretation of those previous results, we attribute this discrepancy to smoothing inherent to the propagator matrix methodology. The effect is amplified compared with comparison between Models 1b and 2 because of increased short wavelength structure in Model 11 (as discussed above, see Section 5.1; Zhong et al., 2000). Nonetheless, spherical harmonic correlation, r_l, is > 0.75 for all degrees examined ($l \leq 50$), and > 0.85 for most degrees. Cell-to-cell differences in surface deflections are broadly normally distributed and centred on zero (Figure 15d).

Figure 16 shows comparisons between surface deflections predicted by models with and without temperature-dependent viscosity. Panels a-c compare the full resolution numerical solutions (Models 1a and 11a), including summary statistics. Panels d-g compare spherical harmonic interpolations of the numerical solutions (Models 1b and 11b). Finally, panels h-k compare propagator matrix solutions for Models 2 and 12, where Model 12 incorporates radial (layer-mean) viscosity extracted from solutions to the numerical Model 11a (incorporating temperature-dependent viscosity; Figure 11c). Unsurprisingly, discrepancy is greatest between the full resolution models. However, discrepancies in cell-to-cell deflections are again, broadly normally distributed and centred on zero, clustering along the 1:1 relationship with $\chi = 1.51$ (panels b-c; see Table 3). Similar results are obtained for both comparisons of spherical harmonically fitted results, and analytical results, albeit with less discrepancy, which is emphasised by tighter normal distributions and lower χ values. Correlation coefficients are > 0.75 for nearly all degrees for both comparisons.

5.3 Upper and Lower Mantle Viscosity and Density Anomalies

Models 13–16: Adjusted Sub-Plate Viscosity

The radial distribution of viscosity, but not its absolute value, plays a crucial role in determining sensitivity of instantaneous solutions for surface deflections to density (and thermal) anomalies in the mantle (e.g., Parsons & Daly, 1983; Hager, 1984). Consequently, we performed a suite of analytical tests in which distributions of upper and lower mantle (radial) temperature-dependent viscosity was varied within propagator matrix solutions. The resulting impact on calculated surface deflections was quantified by comparison with results generated using reference Model 12 (Figure 14). The radial component of viscosity, $\eta(r)$, in each test was modified from that used to generate Model 12 (see solid black curve in Figure 17). Figure 17a-d show results generated by decreasing upper mantle viscosity by an order of magnitude. Panels e–n show the results of decreasing upper mantle viscosity by an order of magnitude. Panels j–p show the impact of using increasingly simple radial viscosity. Calculated sensitivity kernels for the adjusted viscosity profiles demonstrate that decreasing upper mantle viscosity (relative to the reference case) further reduces sensitivity of surface deflections to long-wavelength density structure, especially in the lower mantle (Figure 17b, f, j, n). However, in general, results are similar to the reference model even when $\eta(r)$ is drastically varied, with average χ misfit incurred of only 0.17–0.38 km, and $r_l > 0.97$ across all degrees for all tests. This result emphasizes the fact that viscosity only exerts a relatively minor control on sensitivity of surface deflection to mantle density structure, in terms of instantaneous flow (Table 3, see, e.g., Ghosh et al., 2010; Moucha et al., 2007; Lu et al., 2020).

Models 17–20: Adjusted Density Anomalies

Figure 18 shows results from tests in which the amplitudes of density anomalies in the upper and lower mantle were systematically increased or decreased. Similar to the tests shown in Figure 17, densities are amplified relative to Model 12. Radial viscosity is constant for each of these tests (black curve in Figure 18a; i.e., same as that used to generate Model 12). The reference sensitivity kernel for Model 12 is shown in Figure 14a. Figure 18a-d and g-i show results generated by amplifying respective upper and lower mantle densities by a factor of 2. Panels d-f and j-l show results when amplitudes of density anomalies are decreased by 1/2. Table 3 summarizes the differences incurred to Model 12; although spherical harmonic correlation between models is approximately as good as for the radial viscosity tests (Models 13–16), that is to be expected since we do not vary locations of density anomalies here, only their amplitudes, and r_l is insensitive to amplitudes of the two results being compared. Significant is the fact that mean vertical differences between Models 17–20 and 12 (i.e., χ and $\Delta\bar{h}$) are higher than those calculated for Models 13–16. These results emphasize the relative sensitivity of surface deflections to upper mantle density anomalies, and that even quite large uncertainties in lower mantle density anomalies have relatively little impact on surface deflections. Our conclusion is that accurately constraining and accounting for upper-mantle density structure is of primary concern when estimating surface deflection, and dynamic topography, from mantle convection simulations.

Table 3. Inter-model comparison of predicted surface deflections. Models being compared are summarised in Table 2. Metrics: root-mean-squared difference (χ, km), mean Euclidean (L^2-norm) difference in predicted deflection ($\Delta\bar{h}$, km), and mean spherical harmonic correlation between models ($\bar{r}_l$). Standard deviation of r_l distribution across degrees (s_r) is also stated: note that $r_l \leq 1$. All spherical harmonic representations of output from numerical code and generated by the propagator matrix code are expanded up to maximum degree, $l = 50$. See body text, figures referred to in column 6, and Table 2 for details.

Models	χ	$\Delta\bar{h}$	$\bar{r}_l$	s_r	Figures
1b & 2	0.95	0.69	0.97	0.02	5–6
2 & 3	0.57	0.47	0.99	4×10^{-4}	7
2 & 4	0.13	0.11	0.99	2×10^{-5}	8
2 & 5	0.67	0.48	0.93	0.04	9a-d
2 & 6	1.03	0.74	0.87	0.06	9e-h
2 & 7	1.57	1.12	0.63	0.15	9i-l
2 & 8	1.26	1.04	0.99	1×10^{-3}	10a-d
2 & 9	1.09	0.97	0.99	0.04	10e-h
2 & 10	1.00	0.74	0.96	0.28	10i-l
1a & 11a	1.51	1.04	—	—	11–13, 16a-c
1b & 11b	1.44	0.98	0.79	0.26	11–13, 16d-g
11b & 12	1.20	0.80	0.95	0.02	15
2 & 12	0.92	0.64	0.85	0.27	14, 16h-k
12 & 13	0.31	0.20	0.99	9×10^{-3}	17a-d
12 & 14	0.17	0.10	0.99	3×10^{-3}	17e-h
12 & 15	0.32	0.20	0.98	0.01	17i-l
12 & 16	0.38	0.23	0.98	0.01	17m-p
12 & 17	0.97	0.64	0.98	7×10^{-3}	18a-c
12 & 18	0.48	0.32	0.98	6×10^{-3}	18d-f
12 & 19	0.43	0.29	0.99	3×10^{-3}	18g-i
12 & 20	0.22	0.14	0.99	1×10^{-3}	18j-l

6 Discussion

An important goal is to understand how geological and geomorphological observations at (or close to) Earth's surface can be used to determine the history of mantle convection during, say, the last 100 million years. Various observations now exist that can be used to constrain mantle convection (e.g., Hoggard et al., 2021; Holdt et al., 2022; Davies et al., 2023, see Section 1.1). An obvious approach is to use them to test existing simulations of mantle convection. We start by comparing numerical and analytical predictions of instantaneous surface deflections generated by mantle convection simulations.

Numerical approaches to solving the equations of motion are very flexible, and can incorporate a variety of assumptions and parameterizations that are not amenable to analytical attack (e.g., temperature-dependent viscosity; Section 2.1). However, ensuring accuracy and stability means that the computational burden is often considerable and hence systematic exploration of parameter space remains challenging. In contrast, analytical approaches can yield calculated surface deflections that are (mathematically) accurate for relatively little computational cost, and may include features such as radial gravitation with much less computational cost (Section 3.3). Consequently, it is straightforward to explore parameter space, examine benchmarks, reproduce results, and investigate sensitivity of solutions to different parameterizations. There are, however, important limitations to consider. First, analytical solutions are only known to exist in the spherical domain for fluid bodies with radial viscosity (i.e., no lateral variability in viscosity). Second, generating solutions in the spherical harmonic domain places practical limits on spatial resolution of solutions. Consider that the number of spherical harmonic coefficients per degree $= 2l + 1$, where l is degree, so for a given maximum degree L, there are $(L+1)^2$ coefficients derived in total. For our results, where $L = 50$, there are therefore $2,601$ coefficients altogether, for each model. Consider also that spatial resolution increases approximately with the reciprocal of l (see Section 3.2). Incorporating full resolution (60 km at the surface) output from the numerical models used in this study would therefore require $L \approx 880$, with $776,161$ coefficients. Clearly, computational constraints limit our investigation to $l \lesssim 50$. Furthermore, observational constraints on mantle-related surface deflection are unlikely to be finer than the flexural wavelength of the overlying lithosphere, $l \approx 50$ (e.g., Holdt et al., 2022). With these limitations in mind, we compared surface deflections predicted using different approaches at the same resolution (up to $l = 50$; Sections 2.1 and 3.3). We then quantified the impact of incorporating increasingly complex physics into models used to predict surface deflections (Section 5; Tables 2–3).

First, we simply compared predictions from numerical and analytical approaches parameterised to be as similar as possible. In this test, the models were purposefully simple: viscosity is radial, models are incompressible, and do not include self-gravitation, or radial variation in g. Numerical solutions were transformed into the frequency (spherical harmonic) domain so that they could be compared with analytical solutions, and so that power spectra could be directly compared at appropriate scales. The results show that, for as-similar-as-possible parameterizations, amplitudes of analytical solutions are $\approx 10\%$ lower than numerical solutions (Figure 6). If the numerical model incorporates temperature-dependent viscosity, this discrepancy increases to 25% (Figure 15). We interpret these results in two ways. First, once armed with viscosity and density fields, numerical and analytical approaches broadly yield similar estimates of surface deflections. Second, the relatively damped analytical solutions are a consequence of smoothing steps in the propagator matrix approach.

The similarity of results indicates that the relatively low-cost propagator matrix approach can be used to explore consequences of including additional model complexity. A systematic sweep of parameters, including radial gravitation (Figure 7) and gravitational potential field effects (Figure 8) indicates that their effects on surface deflection are relatively modest. A useful rule of thumb is that self-gravitation perturbs instantaneous surface deflections by $O(1\text{–}10)\%$ when compared to models with constant gravitational acceleration, and even less difference is observed at high degree (e.g., Ricard, 2015, their Section 7.02.2.5.2). Full 3-D self-gravitation may affect the flow field over time, but modelling such effects numerically is currently challenging. Incorporating the effect of deflections of gravitational potential field on flow has a modest impact on amplitudes of surface deflections at degrees 1–2, but overall it contributes even less than radial variation in g to surface deflections across the scales of interest (Figure 7). In contrast, removing shallow structure has a very large impact on predictions. It modifies amplitudes of surface deflections, locations of uplift and subsidence, and degrees over which they are resolved, and hence it modifies power spectral scalings (Table 3, Figure 9). In contrast, viscosity variations do not have much impact on surface deflections compared to other effects, even if they are decreased or increased by an order of magnitude (Figure 17). The distribution of density anomalies, especially in the upper mantle, does however play a very significant role in deflecting the surface (Figure 18). Calculated summary statistics suggest that systematically increasing or decreasing mantle densities significantly impacts amplitudes of surface deflections. Conversely, spherical harmonic correlation coefficients between models with and without density anomalies were largely unaffected, as locations of anomalies were not varied.

These results emphasise the importance of considering sensitivities of surface deflections to the location and scale of flow in the mantle. Taking inspiration from Hager and O'Connell (1981) and Parsons and Daly (1983), we calculate the net contributions from density anomaly structure to surface deflections, as a function of radius, latitude and longitude across all spherical harmonic degrees considered (i.e., $l = 1$ to 50). Contributions to surface deflections from densities at particular radii r, across all spherical harmonic degrees and orders, for each latitude and longitude, $h_e(\theta, \phi)$, are calculated such that

$$h_e(\theta, \phi, r) = \sum_{l=1}^{L} \sum_{m=-l}^{m=l} \left[Y_{lm}(\theta, \phi) \cdot \delta\rho_{lm}(r) \cdot A_l(r) \cdot \Delta r \right], \tag{23}$$

where Δr is the layer spacing $\approx$ 45 km, Y_{lm}, $\delta\rho_{lm}$ and A_l are spherical harmonic coefficients, density anomalies and sensitivities as defined in Section 3.3. Contributions from specific locations and depths to surface deflections as a function of latitude and longitude are shown in Figure 19 for Model 12, for all degrees $1 \leq l \leq 50$. Results for lower maximum l are shown in Supporting Information. Panels a-d show slices through effective density in the upper (at 45, 135, 360 km) and lower mantle (1445 km). A 180° cross-section showing effective densities from the core-mantle-boundary to the surface beneath the Pacific to the Indian Ocean encompassing South America and southern Africa (the same transect as shown in Figure 1) is shown in panel e. Calculated total net surface deflections along the transect from Model 12, which incorporates temperature-dependent viscosity, and Model 2, which does not, are both shown in panel f. A Cartesian version of the cross-section with the same horizontal scale is shown in panel g. The adjacent panel h shows mean density anomaly amplitudes as a function of radius for Model 12 (dashed grey curve), alongside mean effective densities for the two models, and for the case where Model 12 was only expanded to maximum $l = 10$. These panels again emphasize the contribution of density anomalies in the upper mantle to surface displacements, and the risks associated with discarding shallow structure when predicting dynamic topography. In other words, instantaneous surface deflections are most sensitive to the distribution of density anomalies in the upper mantle.

Encouragingly, surface deflections are sensitive to simulated mantle convection patterns and resulting density distributions, and appear to be relatively insensitive to the methodologies used to calculate deflections when parameterizations (assumptions) are consistent. The next step is to make use of independent geological observations to identify optimal simulations and associated parameterizations. In this study, we compared power spectra (strictly, spherical harmonic coefficients) from calculated surface deflections and oceanic age-depth residuals (e.g., Figure 4; Holdt et al., 2022). The simulations examined have spectral slopes consistent with observations if the entire modelling domain (core-mantle boundary to surface) is incorporated, however amplitudes are overpredicted by 1–2 orders of magnitude. The uppermost 100–450 km of the mantle is often excised in geodynamic studies prior to estimating surface deflections. We demonstrate that removing the upper 200 km can generate surface deflections with amplitudes that more closely match observations, especially at spherical harmonic degrees > 10. However, the spectral slopes of predicted deflections are redder than for the oceanic residuals, which implies that a different approach to removing the contribution of upper mantle/lithospheric structure is required. An obvious avenue for future work is to incorporate information about lithospheric structure into these predictions.

The body of geologic and geomorphologic observations that could be used to test the predicted history of surface deflections from mantle convection simulations has grown substantially in the last decade (e.g., uplift and subsidence histories; Section 1.1; see, e.g., Hoggard et al., 2021). A suite of other geological and geophysical observables are also predicted by, or can be derived from, such simulations (e.g., mantle temperatures, heat flux, geoid, seismic velocities, true polar wander). Using them alongside histories of surface deflections to identify optimal simulations is an obvious avenue for future work (e.g., Ball et al., 2021; Lau et al., 2017; Panton et al., 2023; F. D. Richards et al., 2023). Using such data and the methodologies explored in this paper may be a fruitful way of identifying optimal simulations from the considerable inventory that already exists.

7 Conclusions

This study is concerned with quantifying sensitivities and uncertainties of Earth's surface deflections that arise in simulations of mantle convection. Calculated sensitivities of instantaneous deflection of Earth's surface to mantle density structure emphasise the importance of accurate mapping of the upper mantle. Surface deflections are somewhat sensitive to the distribution of viscosity throughout the mantle, but especially to the locations and scales of density anomalies in the upper mantle. The largest discrepancies between predicted deflections seen in this study are generated when upper mantle structure is excised or altered. Doing so changes both the amplitude and distribution of calculated deflections, modifying their power spectral slopes. These results emphasise the importance of incorporating accurate models of lithospheric structure into calculation of sub-plate support of topography, and also the need to accurately determine plate contributions to topography. In contrast, the choice of methodology to estimate surface deflections—analytical or numerical—or boundary conditions are relatively small sources of uncertainty. Similarly, assumed gravitational profiles and temperature dependence of viscosity are relatively minor contributors to uncertainty given reasonable, Earth-like, parameterizations. Nonetheless, these parameterizations may impact surface deflections through their role in determining how upper mantle flow evolves through geologic time. A fruitful next step could be to use the approaches developed in this paper, in combination with careful isolation of plate cooling signatures from surface deflection predictions, to test mantle convection simulations using the existing and growing body of geologic, geomorphologic and geophysical observations.

Open Research Section

TERRA models are archived [here]. The propagator matrix code is archived [here]. Parameterization files are archived [here]. [TO ED: this section will be completed upon final submission, when confirmation of the precise models published is obtained after review.]

Acknowledgments

We thank A. Biggin, H. Brown, C. Davies, A. Ferreira, M. Holdt, P. Japsen, P. Koelemeijer, F. McNab, R. Myhill and J. Ward for helpful discussion. C.O., J.P. and V.M.F. were supported by NERC Grant NE/T01684/1.

References

Al-Hajri, Y., White, N., & Fishwick, S. (2009). Scales of transient convective support beneath Africa. *Geology*, *37*(10), 883–886. doi: 10.1130/G25703A.1

Audet, P. (2014). Toward mapping the effective elastic thickness of planetary lithospheres from a spherical wavelet analysis of gravity and topography. *Physics of the Earth and Planetary Interiors*, *226*, 48–82. Retrieved from `http://dx.doi.org/10.1016/j.pepi.2013.09.011` doi: 10.1016/j.pepi.2013.09.011

Ball, P. W., Duvernay, T., & Davies, D. R. (2022). A coupled geochemical-geodynamic approach for predicting mantle melting in space and time. *Geochemistry, Geophysics, Geosystems*, *23*, 1–31. doi: 10.1029/2022gc010421

Ball, P. W., White, N. J., Maclennan, J., & Stephenson, S. N. (2021). Global Influence of Mantle Temperature and Plate Thickness on Intraplate Volcanism. *Nature Communications*, *12*(2045), 1–13. Retrieved from `http://dx.doi.org/10.1038/s41467-021-22323-9` doi: 10.1038/s41467-021-22323-9

Bangerth, W., Dannberg, J., Fraters, M., Gassmoeller, R., Glerum, A., Heister, T., … Naliboff, J. (2023). ASPECT v2.5.0 [Computer software manual]. Retrieved 2023-08-04, from `https://zenodo.org/record/3924604` doi: 10.5281/zenodo.8200213

Baumgardner, J. R. (1985). Three-dimensional treatment of convective flow in the earth's mantle. *Journal of Statistical Physics*, *39*(5-6), 501–511. doi: 10.1007/BF01008348

Becker, T. W., & Boschi, L. (2002). A comparison of tomographic and geodynamic mantle models. *Geochemistry, Geophysics, Geosystems*, *3*(1), 1–48. doi: 10.1029/2001GC000168

Biggin, A. J., Steinberger, B., Aubert, J., Suttie, N., Holme, R., Torsvik, T. H., … Van Hinsbergen, D. J. (2012). Possible links between long-term geomagnetic variations and whole-mantle convection processes. *Nature Geoscience*, *5*(8), 526–533. doi: 10.1038/ngeo1521

Braun, J. (2010). The many surface expressions of mantle dynamics. *Nature Geoscience*, *3*(12), 825–833. doi: 10.1038/ngeo1020

Bunge, H.-P., & Baumgardner, J. R. (1995). Mantle convection modeling on parallel virtual machines. *Computers in Physics*, *9*(2), 207–215. doi: 10.1063/1.168525

Bunge, H.-P., Hagelberg, C. R., & Travis, B. J. (2003). Mantle circulation models with variational data assimilation: inferring past mantle flow and structure from plate motion histories and seismic tomography. *Geophysical Journal International*, *152*, 280–301. doi: 10.1046/j.1365-246X.2003.01823

Bunge, H.-P., Richards, M. A., & Baumgardner, J. R. (2002). Mantle-circulation models with sequential data assimilation: Inferring present-day mantle structure from plate-motion histories. *Philosophical Transactions of the Royal Society A: Mathematical, Physical and Engineering Sciences*, *360*(1800), 2545–2567. doi: 10.1098/rsta.2002.1080

Colli, L., Ghelichkhan, S., & Bunge, H.-P. (2016). On the ratio of dynamic topography and gravity anomalies in a dynamic Earth. *Geophysical Research Letters*, *43*, 2510–2516. doi: 10.1002/2016GL067929

Colli, L., Ghelichkhan, S., Bunge, H.-P., & Oeser, J. (2018). Retrodictions of Mid Paleogene mantle flow and dynamic topography in the Atlantic region from compressible high resolution adjoint mantle convection models: Sensitivity to deep mantle viscosity and tomographic input model. *Gondwana Research*, *53*, 252–272. doi: 10.1016/j.gr.2017.04.027

Corrieu, V., Thoraval, C., & Ricard, Y. (1995). Mantle dynamics and geoid Green functions. *Geophysical Journal International*, *120*(2), 516–523. doi: 10.1111/j.1365-246X.1995.tb01835.x

Craig, C. H., & McKenzie, D. (1987). Surface deformation, gravity and the geoid from a three-dimensional convection model at low Rayleigh numbers. *Earth and Planetary Science Letters*, *83*, 123–136. doi: 10.1016/0012-821X(87)90056-2

Crameri, F., Schmeling, H., Golabek, G. J., Duretz, T., Orendt, R., Buiter, S. J., ... Tackley, P. J. (2012). A comparison of numerical surface topography calculations in geodynamic modelling: An evaluation of the 'sticky air' method. *Geophysical Journal International*, *189*(1), 38–54. doi: 10.1111/j.1365-246X.2012.05388.x

Czarnota, K., Hoggard, M. J., White, N., & Winterbourne, J. (2013). Spatial and temporal patterns of Cenozoic dynamic topography around Australia. *Geochemistry, Geophysics, Geosystems*, *14*(3), 634–658. doi: 10.1029/2012GC004392

Davies, D. R., Davies, J. H., Bollada, P. C., Hassan, O., Morgan, K., & Nithiarasu, P. (2013). A hierarchical mesh refinement technique for global 3-D spherical mantle convection modelling. *Geoscientific Model Development*, *6*(4), 1095–1107. doi: 10.5194/gmd-6-1095-2013

Davies, D. R., Ghelichkhan, S., Hoggard, M. J., Valentine, A. P., & Richards, F. D. (2023). Observations and Models of Dynamic Topography: Current Status and Future Directions. In J. Duarte (Ed.), *Dynamics of plate tectonics and mantle convection* (pp. 223–269). Elsevier. doi: 10.1016/B978-0-323-85733-8.00017-2

Davies, D. R., Valentine, A. P., Kramer, S. C., Rawlinson, N., Hoggard, M. J., Eakin, C. M., & Wilson, C. R. (2019). Earth's multi-scale topographic response to global mantle flow. *Nature Geoscience*, *12*, 845–850. Retrieved from `http://dx.doi.org/10.1038/s41561-019-0441-4` doi: 10.1038/s41561-019-0441-4

Fernandes, V. M., & Roberts, G. G. (2020). Cretaceous to Recent net continental uplift from paleobiological data: Insights into sub-plate support. *GSA Bulletin*, *133*, 1–20. doi: 10.1130/b35739.1

Fernandes, V. M., Roberts, G. G., White, N., & Whittaker, A. C. (2019). Continental-Scale Landscape Evolution: A History of North American Topography. *Journal of Geophysical Research: Earth Surface*, *124*, 1–34. doi: 10.1029/2018jf004979

Fichtner, A., Kennett, B. L. N., Igel, H., & Bunge, H.-P. (2009). Full seismic waveform tomography for upper-mantle structure in the Australasian region using adjoint methods. *Geophysical Journal International*, *179*(3), 1703–1725. doi: 10.1111/j.1365-246X.2009.04368.x

Fichtner, A., Trampert, J., Cupillard, P., Saygin, E., Taymaz, T., Capdeville, Y., & Villaseñor, A. (2013). Multiscale full waveform inversion. *Geophysical Journal International*, *194*, 534–556. doi: 10.1093/gji/ggt118

Fichtner, A., & Villaseñor, A. (2015). Crust and upper mantle of the western Mediterranean - Constraints from full-waveform inversion. *Earth and Planetary Science Letters*, *428*, 52–62. Retrieved from `http://dx.doi.org/10.1016/j.epsl.2015.07.038` doi: 10.1016/j.epsl.2015.07.038

Flament, N., Gurnis, M., & Muller, R. D. (2013). A review of observations and models of dynamic topography. *Lithosphere*, *5*(2), 189–210. Retrieved from `https://pubs.geoscienceworld.org/lithosphere/article/5/2/189-210/`

145653 doi: 10.1130/L245.1

Flament, N., Gurnis, M., Müller, R. D., Bower, D. J., & Husson, L. (2015). Influence of subduction history on South American topography. *Earth and Planetary Science Letters*, *430*, 9–18. doi: 10.1016/j.epsl.2015.08.006

Foley, S. F., & Fischer, T. P. (2017). An essential role for continental rifts and lithosphere in the deep carbon cycle. *Nature Geoscience*, *10*(12), 897–902. Retrieved from http://dx.doi.org/10.1038/s41561-017-0002-7 doi: 10.1038/s41561-017-0002-7

Forte, A. M. (2007). Constraints on Seismic Models from Other Disciplines - Implications for Mantle Dynamics and Composition. In B. Romanowicz & A. Dziewonski (Eds.), *Seismology and the structure of the earth* (pp. 805–858). Elsevier B.V. doi: 10.1016/B978-044452748-6.00027-4

Forte, A. M., & Peltier, R. (1991). Viscous Flow Models of Global Geophysical Observables 1. Forward Problems. *Journal of Geophysical Research*, *96*(B12), 20131–20159. doi: 10.1029/91JB01709

Forte, A. M., & Peltier, W. R. (1994). The Kinematics and Dynamics of Poloidal-Toroidal Coupling in Mantle Flow: The Importance of Surface Plates and Lateral Viscosity Variations. *Advances in Geophysics*, *36*, 1–119. doi: 10.1016/S0065-2687(08)60537-3

French, S. W., & Romanowicz, B. (2015). Broad plumes rooted at the base of the Earth's mantle beneath major hotspots. *Nature*, *525*(7567), 95–99. doi: 10.1038/nature14876

Galloway, W. E., Whiteaker, T. L., & Ganey-Curry, P. (2011, jul). History of Cenozoic North American drainage basin evolution, sediment yield, and accumulation in the Gulf of Mexico basin. *Geosphere*, *7*(4), 938–973. Retrieved from http://geosphere.gsapubs.org/cgi/doi/10.1130/GES00647.1 doi: 10.1130/GES00647.1

Gantmacher, F. R. (1959). *The Theory of Matrices.* New York: Chelsea Publishing Company.

Ghelichkhan, S., Bunge, H.-P., & Oeser, J. (2021). Global mantle flow retrodictions for the early Cenozoic using an adjoint method: Evolving dynamic topographies, deep mantle structures, flow trajectories and sublithospheric stresses. *Geophysical Journal International*, *226*(2), 1432–1460. doi: 10.1093/gji/ggab108

Ghosh, A., Becker, T. W., & Zhong, S. J. (2010). Effects of lateral viscosity variations on the geoid. *Geophysical Research Letters*, *37*(1), 2–7. doi: 10.1029/2009GL040426

Glišović, P., & Forte, A. M. (2016). A new back-and-forth iterative method for time-reversed convection modeling: Implications for the Cenozoic evolution of 3-D structure and dynamics of the mantle. *Journal of Geophysical Research: Solid Earth*, *121*(6), 4067–4084. doi: 10.1002/2016JB012841

Gunnell, Y., & Burke, K. (2008). The African Erosion Surface: A Continental-Scale Synthesis of Geomorphology, Tectonics, and Environmental Change over the Past 180 Million Years. *Memoir of the Geological Society of America*, *201*, 1–66. doi: 10.1130/2008.1201

Hager, B. H. (1984). Subducted Slabs and the Geoid: Constraints on Mantle Rheology and Flow. *Journal of Geophysical Research*, *89*(B7), 6003–6015.

Hager, B. H., & Clayton, R. W. (1989). Constraints on the Structure of Mantle Convection Using Seismic Observations, Flow Models, and the Geoid. In W. R. Peltier (Ed.), *Mantle convection: Plate tectonics and global dynamics* (pp. 657–763). New York: Gordon and Breach Science Publishers.

Hager, B. H., Clayton, R. W., Richards, M. A., Comer, R. P., & Dziewonski, A. M. (1985). Lower mantle heterogeneity, dynamic topography and the geoid. *Nature*, *313*, 541–545. doi: 10.1038/314752a0

Hager, B. H., & O'Connell, R. J. (1979). Kinematic Models of Large-Scale Flow in the Earth's Mantle. *Journal of Geophysical Research*, *84*(B3), 1031–1048.

Hager, B. H., & O'Connell, R. J. (1981). A Simple Global Model of Plate Dynamics and Mantle Convection. *Journal of Geophysical Research*, *86*(B6), 4843–4867. doi: 10.1029/JB086iB06p04843

Hazzard, J. A. N., Richards, F. D., Goes, S. D. B., & Roberts, G. G. (2022). Probabilistic Assessment of Antarctic Thermomechanical Structure: Impacts on Ice Sheet Stability. *EarthArXiv*. doi: 10.31223/X5C35R

Hoggard, M. J., Austermann, J., Randel, C., & Stephenson, S. (2021). Observational Estimates of Dynamic Topography Through Space and Time. In *Mantle convection and surface expressions* (pp. 371–411). AGU. doi: 10.1002/9781119528609.ch15

Hoggard, M. J., White, N., & Al-Attar, D. (2016). Global dynamic topography observations reveal limited influence of large-scale mantle flow. *Nature Geoscience*, *9*(May), 1–8. doi: 10.1038/ngeo2709

Holdt, M. C., White, N. J., Stephenson, S. N., & Conway-Jones, B. W. (2022). Densely Sampled Global Dynamic Topographic Observations and Their Significance. *Journal of Geophysical Research: Solid Earth*, *127*, 1–32.

Jeans, J. H. (1923). The Propagation of Earthquake Waves. *Proceedings of the Royal Society of London A*, *102*(718), 554–574.

Kaula, W. M. (1963). Determination of the Earth's Gravitational Field. *Reviews of Geophysics*, *1*(4), 507–551.

Lambeck, K., Smither, C., & Johnston, P. (1998). Sea-level change, glacial rebound and mantle viscosity for northern Europe. *Geophysical Journal International*, *134*, 102–144. doi: 10.1046/j.1365-246X.1998.00541.x

Lau, H. C. P., Mitrovica, J. X., Davis, J. L., Tromp, J., Yang, H.-Y., & Al-Attar, D. (2017). Tidal tomography constrains Earth's deep-mantle buoyancy. *Nature*, *551*(7680), 321–326. doi: 10.1038/nature24452

Lekić, V., & Fischer, K. M. (2014). Contrasting lithospheric signatures across the western United States revealed by Sp receiver functions. *Earth and Planetary Science Letters*, *402*, 90–98. doi: 10.1016/j.epsl.2013.11.026

Lu, C., Forte, A. M., Simmons, N. A., Grand, S. P., Kajan, M. N., Lai, H., & Garnero, E. J. (2020). The Sensitivity of Joint Inversions of Seismic and Geodynamic Data to Mantle Viscosity. *Geochemistry, Geophysics, Geosystems*, *21*(4), 1–29. doi: 10.1029/2019gc008648

McKenzie, D. (1977). Surface deformation, gravity anomalies and convection. *Geophysical Journal of the Royal Astronomical Society*, *48*, 211–238. doi: 10.1111/j.1365-246X.1977.tb01297.x

McKenzie, D. P., Roberts, J. M., & Weiss, N. O. (1974). Convection in the earth's mantle: Towards a numerical simulation. *Journal of Fluid Mechanics*, *62*(3), 465–538. doi: 10.1017/S0022112074000784

Menard, H. W. (1973). Depth anomalies and the bobbing motion of drifting islands. *Journal of Geophysical Research*, *78*(23), 5128–5137. doi: 10.1029/jb078i023p05128

Merdith, A. S., Williams, S. E., Collins, A. S., Tetley, M. G., Mulder, J. A., Blades, M. L., … Müller, R. D. (2021). Extending full-plate tectonic models into deep time: Linking the Neoproterozoic and the Phanerozoic. *Earth-Science Reviews*, *214*(103477), 1–44. doi: 10.1016/j.earscirev.2020.103477

Mitrovica, J. X., & Forte, A. M. (2004). A new inference of mantle viscosity based upon joint inversion of convection and glacial isostatic adjustment data. *Earth and Planetary Science Letters*, *225*(1-2), 177–189. doi: 10.1016/j.epsl.2004.06.005

Molnar, P., England, P. C., & Jones, C. H. (2015, mar). Mantle dynamics, isostasy, and the support of high terrain. *Journal of Geophysical Research: Solid Earth*, *120*(3), 1932–1957. Retrieved from `http://doi.wiley.com/10.1002/2014JB011724` doi: 10.1002/2014JB011724

Morris, M., Fernandes, V. M., & Roberts, G. G. (2020). Extricating dynamic topography from subsidence patterns: Examples from Eastern North America's passive margin. *Earth and Planetary Science Letters*, *530*(115840), 1–13. Retrieved from `https://doi.org/10.1016/j.epsl.2019.115840` doi: 10.1016/j.epsl.2019.115840

Moucha, R., & Forte, A. M. (2011). Changes in African topography driven by mantle convection: supplementary information. *Nature Geoscience*, *4*(10), 707–712. doi: 10.1038/ngeo1235

Moucha, R., Forte, A. M., Mitrovica, J. X., & Daradich, A. (2007). Lateral variations in mantle rheology: Implications for convection related surface observables and inferred viscosity models. *Geophysical Journal International*, *169*(1), 113–135. doi: 10.1111/j.1365-246X.2006.03225.x

Moucha, R., Forte, A. M., Mitrovica, J. X., Rowley, D. B., Quéré, S., Simmons, N. A., & Grand, S. P. (2008). Dynamic topography and long-term sea-level variations: There is no such thing as a stable continental platform. *Earth and Planetary Science Letters*, *271*(1-4), 101–108. doi: 10.1016/j.epsl.2008.03.056

O'Connell, R. J. (1971). Pleistocene Glaciation and the Viscosity of the Lower Mantle. *Geophysical Journal of the Royal Astronomical Society*, *23*(3), 299–327. doi: 10.1111/j.1365-246X.1971.tb01823.x

O'Malley, C. P. B., White, N. J., Stephenson, S. N., & Roberts, G. G. (2021). Large-Scale Tectonic Forcing of the African Landscape. *Journal of Geophysical Research: Earth Surface*, *126*, 1–37. doi: 10.1029/2021jf006345

Panasyuk, S. V., Hager, B. H., & Forte, A. M. (1996). Understanding the effects of mantle compressibility on geoid kernels. *Geophysical Journal International*, *124*(1), 121–133. doi: 10.1111/j.1365-246X.1996.tb06357.x

Panton, J., Davies, J. H., & Myhill, R. (2023). The Stability of Dense Oceanic Crust Near the Core-Mantle Boundary. *Journal of Geophysical Research: Solid Earth*, *128*, 1–21. doi: 10.1029/2022JB025610

Parsons, B., & Daly, S. (1983). The relationship between surface topography, gravity anomalies and temperature structure of convection. *Journal of Geophysical Research*, *88*(B2), 1129–1144. doi: 10.1029/JB088iB02p01129

Pekeris, C. L. (1935). Thermal Convection in the Interior of the Earth. *Geophysical Supplements to the Monthly Notices of the Royal Astronomical Society*, *3*(8), 343–367.

Priestley, K., & McKenzie, D. (2013). The relationship between shear wave velocity, temperature, attenuation and viscosity in the shallow part of the mantle. *Earth and Planetary Science Letters*, *381*, 78–91. Retrieved from `http://dx.doi.org/10.1016/j.epsl.2013.08.022` doi: 10.1016/j.epsl.2013.08.022

Ribe, N. M. (2007). Analytical Approaches to Mantle Dynamics. *Treatise on Geophysics*, *7*, 167–226. doi: 10.1016/B978-044452748-6.00117-6

Ricard, Y. (2007). Physics of Mantle Convection. *Treatise on Geophysics*, *7*, 31–88.

Ricard, Y. (2015). Physics of Mantle Convection. In G. Schubert (Ed.), *Treatise on geophysics* (pp. 23–71). doi: 10.1016/B978-044452748-6.00115-2

Richards, F. D., Hoggard, M. J., Ghelichkhan, S., Koelemeijer, P., & Lau, H. C. P. (2021). Geodynamic, geodetic, and seismic constraints favour deflated and dense-cored LLVPs. *EarthArXiv*, 1–20. doi: 10.31223/X55601

Richards, F. D., Hoggard, M. J., Ghelichkhan, S., Koelemeijer, P., & Lau, H. C. P. (2023). Geodynamic, geodetic, and seismic constraints favour deflated and dense-cored LLVPs. *Earth and Planetary Science Letters*, *602*(117964), 1–13. Retrieved from `https://doi.org/10.1016/j.epsl.2022.117964` doi: 10.1016/j.epsl.2022.117964

Richards, F. D., Hoggard, M. J., White, N., & Ghelichkhan, S. (2020). Quantifying the relationship between short-wavelength dynamic topography and thermomechanical structure of the upper mantle using calibrated parameterization of anelasticity. *Journal of Geophysical Research: Solid Earth*, *125*, 1–36. doi:

10.1029/2019JB019062

Richards, M. A., & Hager, B. H. (1984). Geoid Anomalies in a Dynamic Earth. *Journal of Geophysical Research*, *89*(B7), 5987–6002. doi: 10.1029/JB089iB07p05987

Salles, T., Flament, N., & Müller, D. (2017, jan). Influence of mantle flow on the drainage of eastern Australia since the Jurassic Period. *Geochemistry, Geophysics, Geosystems*, *18*(1), 280–305. doi: 10.1002/2016GC006617

Spasojevic, S., & Gurnis, M. (2012). Sea level and vertical motion of continents from dynamic earth models since the Late Cretaceous. *AAPG Bulletin*, *96*(11), 2037–2064. doi: 10.1306/03261211121

Stanley, J. R., Braun, J., Baby, G., Guillocheau, F., Robin, C., Flowers, R. M., ... Beucher, R. (2021). Constraining Plateau Uplift in Southern Africa by Combining Thermochronology, Sediment Flux, Topography, and Landscape Evolution Modeling. *Journal of Geophysical Research: Solid Earth*, *126*, 1–34. doi: 10.1029/2020JB021243

Steinberger, B. (2007). Effects of latent heat release at phase boundaries on flow in the Earth's mantle, phase boundary topography and dynamic topography at the Earth's surface. *Physics of the Earth and Planetary Interiors*, *164*(1-2), 2–20. doi: 10.1016/j.pepi.2007.04.021

Steinberger, B. (2016). Topography caused by mantle density variations: Observation-based estimates and models derived from tomography and lithosphere thickness. *Geophysical Journal International*, *205*(1), 604–621. doi: 10.1093/gji/ggw040

Steinberger, B., & Antretter, M. (2006). Conduit diameter and buoyant rising speed of mantle plumes: Implications for the motion of hot spots and shape of plume conduits. *Geochemistry, Geophysics, Geosystems*, *7*(11), 1–25. doi: 10.1029/2006GC001409

Steinberger, B., & Calderwood, A. R. (2006). Models of large-scale viscous flow in the Earth's mantle with constraints from mineral physics and surface observations. *Geophysical Journal International*, *167*(3), 1461–1481. doi: 10.1111/j.1365-246X.2006.03131.x

Steinberger, B., & O'Connell, R. J. (1997). Changes of the Earth's rotation axis owing to advection of mantle density heterogeneities. *Nature*, *387*, 169–173. doi: 10.1038/387169a0

Stephenson, S. N., White, N. J., Carter, A., Seward, D., Ball, P. W., & Klöcking, M. (2021). Cenozoic Dynamic Topography of Madagascar. *Geochemistry, Geophysics, Geosystems*, *22*, 1–38. doi: 10.1029/2020gc009624

Tackley, P. J., Stevenson, D. J., Glatzmaier, G. A., & Schubert, G. (1993). Effects of an endothermic phase transition at 670 km depth on spherical mantle convection. *Nature*, *361*, 699–704. doi: 10.1038/361699a0

Thoraval, C., Machete, P., & Cazenave, A. (1994). Influence of mantle compressibility and ocean warping on dynamical models of the geoid. *Geophysical Journal International*, *117*, 566–573. doi: 10.1111/j.1365-246X.1994.tb03954.x

Thoraval, C., & Richards, M. A. (1997). The geoid constraint in global geodynamics: Viscosity structure, mantle heterogeneity models and boundary conditions. *Geophysical Journal International*, *131*, 1–8. doi: 10.1111/j.1365-246X.1997.tb00591.x

Turcotte, D. L., & Schubert, G. (2002). *Geodynamics* (Second Edi ed.). Cambridge University Press.

van Heck, H. J., Davies, J. H., Elliott, T., & Porcelli, D. (2016). Global-scale modelling of melting and isotopic evolution of Earth's mantle: Melting modules for TERRA. *Geoscientific Model Development*, *9*, 1399–1411. doi: 10.5194/gmd-9-1399-2016

Wieczorek, M. A., & Meschede, M. (2018). SHTools: Tools for Working with Spherical Harmonics. *Geochemistry, Geophysics, Geosystems*, *19*, 1–19.

Retrieved from http://doi.wiley.com/10.1029/2018GC007529 doi: 10.1029/2018GC007529

Zhong, S., Gurnis, M., & Hulbert, G. (1993). Accurate determination of surface normal stress in viscous flow from a consistent boundary flux method. *Physics of the Earth and Planetary Interiors*, *78*, 1–8. doi: 10.1016/0031-9201(93)90078-N

Zhong, S., McNamara, A., Tan, E., Moresi, L., & Gurnis, M. (2008). A benchmark study on mantle convection in a 3-D spherical shell using CitcomS. *Geochemistry, Geophysics, Geosystems*, *9*(10), 1–32. doi: 10.1029/2008GC002048

Zhong, S., Zuber, M. T., Moresi, L., & Gurnis, M. (2000). Role of temperature-dependent viscosity and surface plates in spherical shell models of mantle convection. *Journal of Geophysical Research*, *105*(B5), 11063–11082.

Figure 1. Examples of mantle densities and viscosity used to calculate stresses and dynamic topography numerically and analytically. (a) Great-circle slice (180°) through full-resolution, present-day, density ρ, predicted by TERRA model with temperature dependent viscosity (Model 11a; see Table 2 and body text); see globe to left for location. White circles = 20° intervals; filled black circle indicates orientation of cross section; dashed line = 660 km depth contour; dotted line = 1038 km depth contour, at which depth ρ is plotted on globe; white-black curve = numerical prediction of surface normal stress σ_{rr} from Model 11a. (b) As (a) but slice is through spherical harmonic expansion of density structure, to maximum degree $l = 50$ ($\lambda \approx 792$ km; Model 11b); black-white curve = surface deflection h, calculated using (analytic) propagator matrix approach (Model 12). (c) As (a) but for slice through full-resolution viscosity structure of numerical model. (d) As (c) but for mean (radial) viscosity structure, used along with the density structure shown in (b) to generate analytical solution for surface deflection shown by black-white curve atop (b). (e–f) As (c–d) but viscosity is expressed as a percentage anomaly with respect to the layer (radial) mean.

Figure 2. Model 1: Densities predicted from numerical simulation of mantle convection. (a) Predicted present-day density ρ, at surface (z=0), from TERRA model with viscosity independent of temperature (Table 2: Model 1a), plotted at grid resolution of 1 degree. (b) Histogram of values shown in (a), weighted by latitude to correct to equal-area. (c–d) As (a–b) but for densities at a depth of 270 km. (e–h) As (a–d) but for time slice at 10 Ma; paleo-coastlines generated from Phanerozoic plate rotation history of Merdith et al. (2021). (i–l) As (a–d) but for time slice at 100 Ma.

Figure 3. Model 1: Surface stresses from numerical simulation of mantle convection and spherical harmonic expansion up to degree 50. (a) Predicted present-day surface radial stress, σ_{rr} from numerical TERRA model (Model 1a), plotted at grid resolution of 1 degree. (b) Histogram of values shown in (a), weighted by latitude to correct to equal-area. (c) Black line = radial viscosity structure used to drive Model 1a and thus produce grid shown in panel (a). Gray dashed lines = alternative viscosity profiles of (from darkest to lightest), Mitrovica and Forte (2004), Steinberger and Calderwood (2006), and μ_1, μ_2 from Ghelichkhan et al. (2021). (d) Model 1b: Global interpolation of spherical harmonic expansion of Model 1a (panel a), up to maximum degree $l = 50$ (i.e., minimum wavelength $\lambda \approx 792$ km; Model 1b), calculated using inversion approach of Hoggard et al. (2016). (e) Histogram of values shown in (d), weighted by latitude to correct to equal-area. (f) Power spectrum, in terms of total power per degree, of stress field shown in (d), as a function of spherical harmonic degree l.

Figure 4. Model 1: Predicted water- and air-loaded dynamic topography. (a) Water-loaded, present day, surface deflection predicted by Model 1a. Figure 3a shows normal stress, σ, used with Equation 11 to calculate dynamic topography, h; $\rho_w = 1030$ kg m^{-3}. (b) Spherical harmonic fit (Model 1b) up to degree $l = 50$ of grid shown in (a), calculated using the approach of Hoggard et al. (2016). (c–d) Histogram of values shown in (a) and (b) respectively, weighted by latitude to correct to equal-area. (e) Black line = power spectrum in terms of total power per degree, from spherical harmonic expansion shown in (b); gray line and band = expected dynamic topography from Kaula's rule using admittance $Z = 12 \pm 3$ mGal km^{-1} (Kaula, 1963). Orange dashed line = expected power spectrum for water-loaded residual topography from Holdt et al. (2022), via analytical solution of special case of Equation 16. χ_p = total root-mean-squared difference between distribution of modeled and theoretical surface deflection power (see Equation 21. (f–j) As (a–e) but for air-loaded surface deflection; $\rho_w = 1$ kg m^{-3}.

Figure 5. Model 2: Propagator matrix solution for surface deflection with associated sensitivity kernels. (a) Surface deflection sensitivity kernel A_l, as a function of spherical harmonic degree, l, and depth, calculated for the radial viscosity structure (and other parameters) which were used to generate Model 1; see Equation 17. (b) Present-day predicted water-loaded surface deflection, calculated using propagator matrix method, from spherical harmonic expansion (to maximum degree $l = 50$) of density structure (e.g., Figure 2a, c) and radial viscosity structure (e.g., Figure 3c; Corrieu et al., 1995; Hager et al., 1985; Parsons & Daly, 1983). Note that for comparison with numeric calculations shown in Figure 4, no terms related to flow-related perturbation of gravitational potential terms are included (see Equations 17 and 18), and gravitational acceleration $g = 10$ m s^{-2} everywhere. (c) Histogram of values shown in (b), weighted by latitude to correct to equal-area. (d) Black line = power spectrum in terms of total power per degree, from surface deflection prediction shown in (a); gray line and band = expected dynamic topography from Kaula's rule using admittance $Z = 12 \pm 3$ mGal km^{-1} (Kaula, 1963). Orange dashed line = power spectrum of water-loaded residual topography from Holdt et al. (2022), via analytical solution of special case of Equation 16. χ_p = total root-mean-squared difference between distribution of modeled and theoretical surface deflection power (see Equation 21. (e–h) As (a–d) but for air-loaded surface deflection; $\rho_w = 1$ kg m^{-3}.

Figure 6. Comparison of numeric and analytic estimation of dynamic topography (Models 1b & 2). (a) Model 1b: Spherical harmonic expansion of predicted present-day water-loaded surface deflection converted from stress output from TERRA (Model 1a), to maximum degree $l = 50$, as in Figure 4f. (b) Model 2: As (a) but for prediction made using propagator matrix method, as in Figure 5b. (c) Difference, Δh, between Models 1b and 2 (panels a and b). (d) Histogram of difference values shown in (c), weighted by latitude to correct to equal-area. (e) Spectral correlation coefficient, r_l, between predictions shown in (a) and (b); Equation 20. (f) Numeric (Model 1b) versus analytic (Model 2) predictions of surface deflection; χ = root-mean-squared difference between predictions, Equation 19; gray dashed line = 1:1 ratio. (g) Black bars = histogram of ratios between analytic:numeric solutions for surface deflection as in (f), weighted by latitude. Gray dashed line = 1 (i.e., identical values). Gray bars = as black bars, but for propagator matrix solution amplitudes scaled up by optimal factor to fit numerical solution (10%).

Figure 7. Model 3: Predicted surface deflection from mantle convection in presence of radial gravitation. (a) Predicted present-day water-loaded surface deflection calculated using propagator matrix method, incorporating radial gravitation i.e., $g(r)$, black curve in (b). (b) Black curve = profile of gravitational acceleration as a function of radius, given density distribution predicted by Model 1a; gray dashed line = constant value of $g = 10$ m s^{-2} used within TERRA model runs and in previous figures. (c) As (a) but calculated using $g = 10$ m s^{-2} everywhere, i.e., same as Figure 5a (dashed line in panel b). (d) Difference between surface deflections predicted by Models 3 and 2 (panels a and c). (e) Histogram of values in (d), weighted by latitude to correct to equal-area.

Figure 8. Model 4: Comparing predicted surface deflections with and without stress perturbations induced by gravitational potential of deflected surface. (a) Predicted present-day water-loaded surface deflection calculated using propagator matrix method, with $g = 10$ m s^{-2} everywhere, including terms describing stress perturbation due to change in gravitational potential (i.e., u_3 term in Equation 17). (b) As (a) but calculated excluding u_3 term, i.e., same as Figure 5a. (c) Difference between Models 4 and 2 (panels a and b). Note same colour scales are used as in Figure 7. (d) Histogram of values in (d), weighted by latitude to correct to equal-area.

Figure 9. Models 5–7: Effect of removing shallow structure from analytic surface deflection calculations. (a) Model 5: Predicted water-loaded surface deflection from propagator matrix solution for Model 2, i.e., as Figure 5b, but with effect of upper 50 km of density anomaly structure ignored in calculation. (b) Black line = power spectrum of surface deflection shown in (a); gray line and band = expected dynamic topography from Kaula's rule using admittance $Z = 12 \pm 3$ mGal km^{-1} (Kaula, 1963). Orange dashed line = expected power spectrum for water-loaded residual topography from Holdt et al. (2022), via analytical solution of special case of Equation 16. χ_p = total root-mean-squared difference between distribution of modeled and theoretical surface deflection power (see Equation 21). (c) Difference between Models 5 and 2, i.e., between panel (a) and original propagator matrix solution, Model 2, shown in Figure 5b. (d) Spectral correlation coefficient, r_l, between Model 5 and 2; Equation 20. (e–h) and (i–l) as (a–d) but for depth cut-offs of 100 (Model 6) and 200 km (Model 7), respectively.

Figure 10. Models 8–10: Testing free-slip vs. no-slip ("rigid") surface and CMB boundary conditions. (a) Water-loaded surface deflection sensitivity kernel A_l, for Model 8, which has a no-slip surface boundary condition, but otherwise is parameterised the same as Model 2. (b) Sensitivity kernel of Model 8 minus sensitivity kernel of Model 2 (see Figure 5a). Note, positive difference implies reduced sensitivity compared to Model 2, and vice versa, since A_l is negative. (c) Predicted water-loaded surface deflection for Model 8. (d) Difference between surface deflection predictions for Model 8 and Model 2 (see Figure 5b). (e–h) as (a–d) but for Model 9: free-slip surface boundary, no-slip CMB. (i–l) as (a–d) but for Model 10: no-slip surface and CMB boundaries.

Figure 11. Model 11: Numerical simulation of mantle convection with temperature dependent viscosity, η, and spherical harmonic representation. (a) Present-day viscosity at surface from Model 11a, expressed as percentage deviation from layer mean, $\delta\eta$, plotted at grid resolution of 1 degree. (b) Histogram of values shown in (a), weighted by latitude to correct to equal-area. (c) Black line and gray band = global mean and extreme viscosity values as a function of depth; pink band = depth slice shown in (a). (d) Model 11b: Spherical harmonic fit up to degree $l = 50$ of grid shown in (a), using inverse approach of Hoggard et al. (2016). (e–h) As (a–d) but for depth slice at 271 km below surface. (i–l) and (m–p) 587 km and 2032 km depth slices.

Figure 12. Model 11: Densities predicted by numerical simulation with temperature-dependent viscosity. (a) Predicted present-day density ρ, at surface (z=0), from TERRA model. (b) Histogram of values shown in (a), weighted by latitude. (c–d) As panels (a–b) but for densities at 270 km depth. (e–h) and (i–l) As panels (a–d) for time slices at 10 and 100 Ma (see caption of Figure 2 for expanded description; Figure 11 for viscosity structure; Equation 7).

Figure 13. Model 11: Predictions of surface stresses and deflections from simulations with temperature dependent viscosity. (a) Predicted present-day surface radial stress, σ_{rr} from numerical TERRA model (Model 11a), plotted at grid resolution of 1 degree. (b) Model 11b: Spherical harmonic representation of Model 11a up to degree $l = 50$. (c) Histogram of values shown in (a), weighted by latitude to correct to equal-area. (d) Histogram of values shown in panel (b). (e) Power spectrum of surface stresses. (f–i) Calculated water-loaded surface deflections and associated histograms for full resolution numerical solutions (f, h) and spherical harmonic representation (g, i). (j) Power spectrum (black) of water-loaded surface deflection (panel g), Kaula's rule (grey curve and band), and water-loaded residual topography (orange); see Figure 4 for expanded description.

Figure 14. Model 12: Analytical (propagator matrix) predictions of surface deflections from simulations with temperature dependent viscosity. Radial viscosity is calculated using mean (radial) values from numerical model with temperature-dependent viscosity (i.e., Model 11a; Figure 13). (a–d) Present-day, water-loaded, surface deflection calculated analytically using propagator matrix solution; see Figure 5 for expanded description of panels. (e–h) Air-loaded deflection and associated metrics.

Figure 15. Models 11b & 12: Comparison of surface deflections calculated numerically and analytically using results from simulation with temperature dependent viscosity. (a) Model 11b: Spherical harmonic expansion of predicted present-day water-loaded surface deflection converted from stress output from TERRA (Model 11a), to maximum degree $l = 50$. (b) Model 12: As (a) but for prediction made using propagator matrix method. (c) Difference, Δh, between Models 11b and 12 (panels a and b). (d) Histogram of difference values shown in (c), weighted by latitude to correct to equal-area. (e) Spectral correlation coefficient, r_l, between predictions shown in (a) and (b); Equation 20. (f) Numeric (Model 11b) versus analytic (Model 12) predictions of surface deflection; χ = root-mean-squared difference between predictions, Equation 19; gray dashed line = 1:1 ratio. (g) Histogram of ratios between analytic:numeric solutions for surface deflection as in (f), weighted by latitude. Gray dashed line = 1 (i.e., identical values). Gray bars = as black bars, but for propagator matrix solution amplitudes scaled up by optimal factor to fit numerical solution (24%).

Figure 16. Comparing surface deflections calculated using normal stresses from numeric simulations (Models 1 and 11) and analytic estimates (Models 2 and 12) with and without temperature dependent viscosity. (a) Difference in predicted surface deflection, Δh, between numerical simulations with (Model 11a) and without (Model 1a) temperature-dependent viscosity. Full-resolution surface radial stresses are converted into surface deflections, h, using Equation 11. (b) Histogram of values shown in (a). (c) Pixel-wise comparison of predicted surface deflection between the two models; χ = root-mean-squared difference between predictions, see Equation 19; gray dashed line = 1:1 ratio. (d–f) as (a–c) but for surface deflection calculated using spherical harmonic expansion of surface radial stresses (Model 1b vs. 11b). (g) Spectral correlation coefficient, r_l, between model predictions (with and without temperature dependent viscosity; see Equation 20). (h–k) as (d–g) but for surface deflections calculated for each model using the propagator matrix approach (Model 2 vs. 12).

Figure 17. Models 13–16: Sensitivity of calculated analytic surface deflection to adjusted radial viscosity. (a) Model 13: Black curve = prediction of present-day radial mean viscosity from Model 11; red line = adjusted radial profile with viscosity decreased by a factor of 10 between depths of $\sim$ 300–500 km; gray dashed lines = viscosity profiles used in other studies (see Figure 3). (b) Sensitivity kernel generated using adjusted viscosity shown in (a). (c) Surface deflection calculated using propagator matrix approach parameterised using adjusted viscosity profile (red curve in panel a), and resulting sensitivity kernel shown in panel (b). (d) Difference between propagator matrix solutions generated using adjusted and un-adjusted viscosity profiles, i.e., panel (c) minus Figure 15b (Model 13 vs. 12). Value of root-mean-squared difference, χ, (between calculated surface deflections for un-adjusted and adjusted viscosity) is stated (see Equation 19). (e–h) Model 14: As (a–d) but applying an increase in viscosity of a factor of 10 between $\sim$ 300–500 km. (i–l) Model 15: As (a–d) but applying an increase in viscosity of a factor of 100 between $\sim$ 300–500 km. (m–p) Model 16: As (a–d) but applying an constant viscosity of $\approx 7.5 \times 10^{22}$ Pa s (i.e., the mean value of the reference profile) across all depths.

Figure 18. Models 17–20: Sensitivity of calculated analytic surface deflection to adjusted density anomalies. Annotation is as for Figure 17 but for adjusted density anomalies (red lines in left panels), by directly scaling spherical harmonic coefficients ($l > 0$) up or down by a factor of 2 (Models 17 & 19, panels a–c & g–i, respectively) or $\frac{1}{2}$ (Models 18 & 20: d–f & j–l). Viscosity structure applied in each case is same as that used to generate Figure 15b. Sensitivity kernels for surface deflection are not shown since they are invariant with respect to density anomalies, $\Delta\rho$, depending only on viscosity structure.

Figure 19. Effective density. Contributions from density anomalies to surface deflection. (a–d) Maps of net contribution to present-day water-loaded surface deflection calculated using propagator matrix approach (Model 12; see body text for details). Depth slices at 45, 135, 360 and 1445 km depth incorporating all spherical harmonic degrees l and orders m, up to $l = 50$. (e) Great-circle slice (180°) showing contributions to surface deflection; globe to right shows transect location and calculated surface deflection (same as Figure 14b). White circles = 20° intervals; note filled black circle for orientation; dashed line = 660 km depth contour. (f) White-black curve = total surface deflection along transect shown atop globe in panel (e); abscissa aligned with panel g; orange dashed line = same but for maximum l = 10 (see Supporting Information Figure S4); red dashed curve = surface deflection from Model 2. (g) Cartesian version of panel (e); ordinate aligned with panel (h). (h) Grey dashed curve = mean absolute value of density anomalies in Model 12—see top axis for values. Black curve = global mean amplitude (modulus) of contribution from density structure in Model 12 to total surface deflection h, across all l and m; orange line = same but for maximum $l = 10$; red dashed line = results for Model 2.

Supporting Information for "Reconciling Surface Deflections From Simulations of Global Mantle Convection"

Conor P. B. O'Malley[1], Gareth G. Roberts[1], James Panton[2], Fred D. Richards[1], J. Huw Davies[2], Victoria Milanez Fernandes[1,3], Siavash Ghelichkhan[4]

[1]Department of Earth Science & Engineering, Imperial College London, Royal School of Mines, Prince Consort Road, London SW7 2BP, UK

[2]School of Earth & Environmental Sciences, University of Cardiff, Park Place, Cardiff CF10 3AT, UK

[3]now at Section 4.6 Geomorphology, GFZ Potsdam, Telegrafenberg, 14473 Potsdam, Germany

[4]Research School of Earth Sciences, Australian National University, 142 Mills Road, Acton, ACT 0200, Australia

Contents of this file

1. Figures S1 to S5

Introduction

This Supporting Information document includes five figures in the same format as Figure 19 of the main text. They show calculated net contributions from density anomalies in the mantle to surface deflections. In the main text, we show spherical harmonic solutions up

---

Corresponding authors: C. P. O'Malley or G. G. Roberts, Department of Earth Science & Engineering, Imperial College London, Royal School of Mines, Prince Consort Road, London SW7 2BP, UK. (c_omalley1@msn.com or gareth.roberts@imperial.ac.uk)

to a maximum spherical harmonic degree $l = 50$. Here, results are presented for maximum degrees 40, 30, 20, 10 and 5. The results demonstrate the importance of contributions from short wavelength (high degree) density structure to surface deflections, especially at shallow depths.

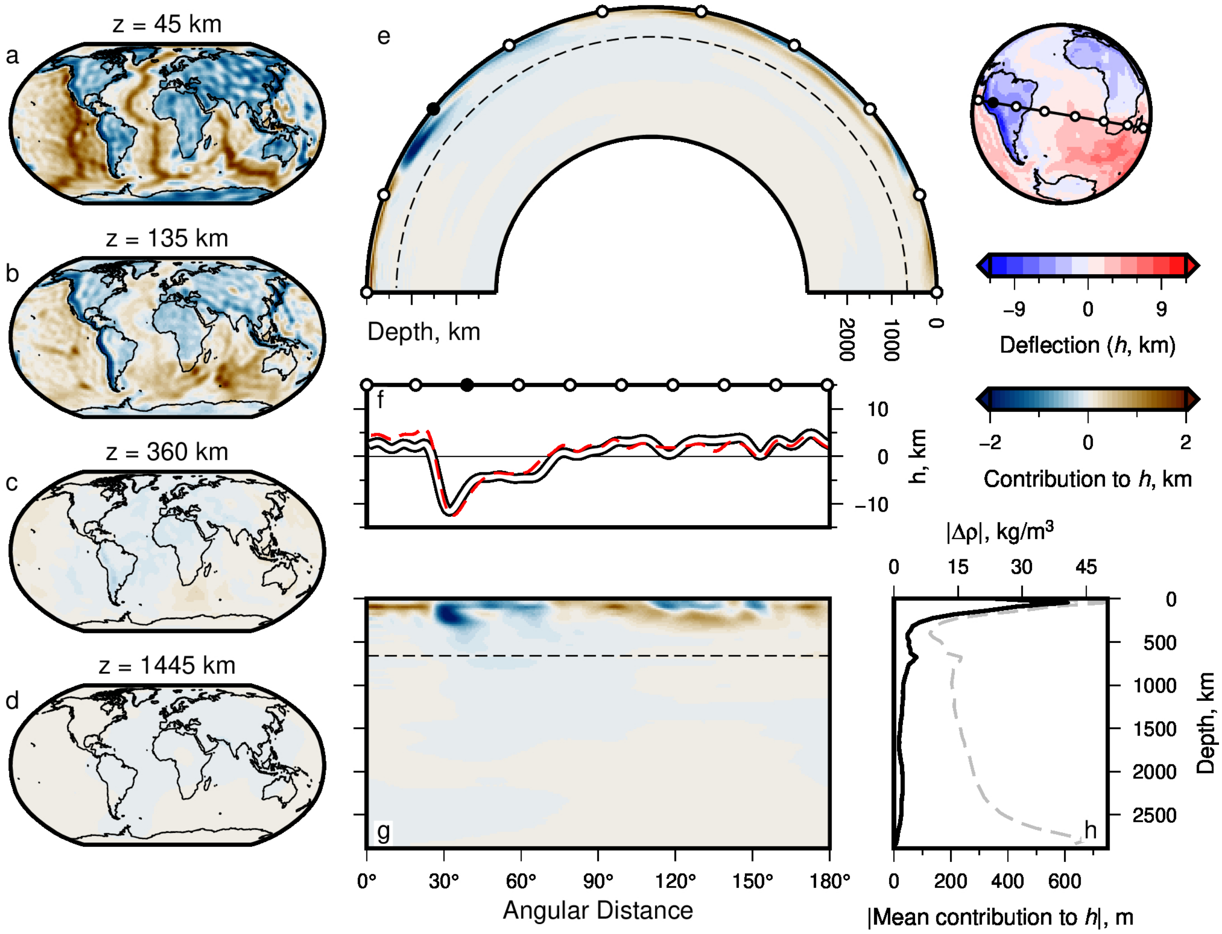

Figure S1. Surface deflections and effective densities up to maximum degree 40. (a–d) Net contribution to present-day water-loaded surface deflection calculated using analytical approach with maximum $l = 40$. Depth slices at 45, 135, 360 and 1445 km depth. (e) Great-circle slice (180°) showing contributions to surface deflection; globe to right shows transect location and calculated surface deflection, up to maximum $l = 40$. White circles = 20° intervals; filled black circle is for orientation; dashed line = 660 km depth contour. (f) White-black curve = surface deflection along transect shown atop globe in panel (e); red dashed curve = surface deflection from Model 2. (g) Cartesian version of panel (e). (h) Grey dashed curve = mean absolute value of density anomalies in Model 12—see top axis for values. Black curve = global mean amplitude (modulus) of contribution from density structure up to maximum $l = 40$ to total surface deflection h.

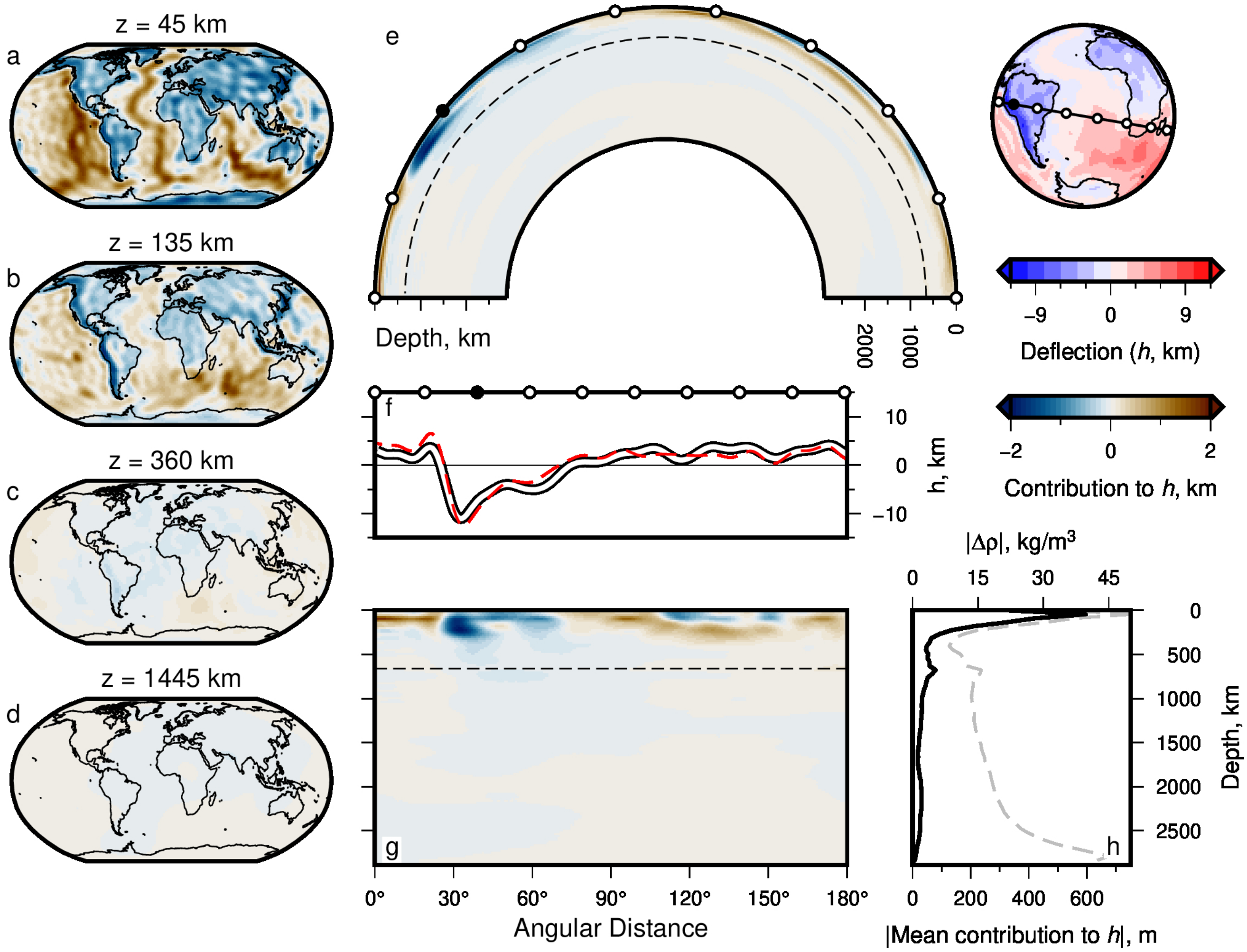

Figure S2. Surface deflections and effective densities up to maximum degree 30. As Figure S1, but for maximum spherical harmonic degree $l = 30$.

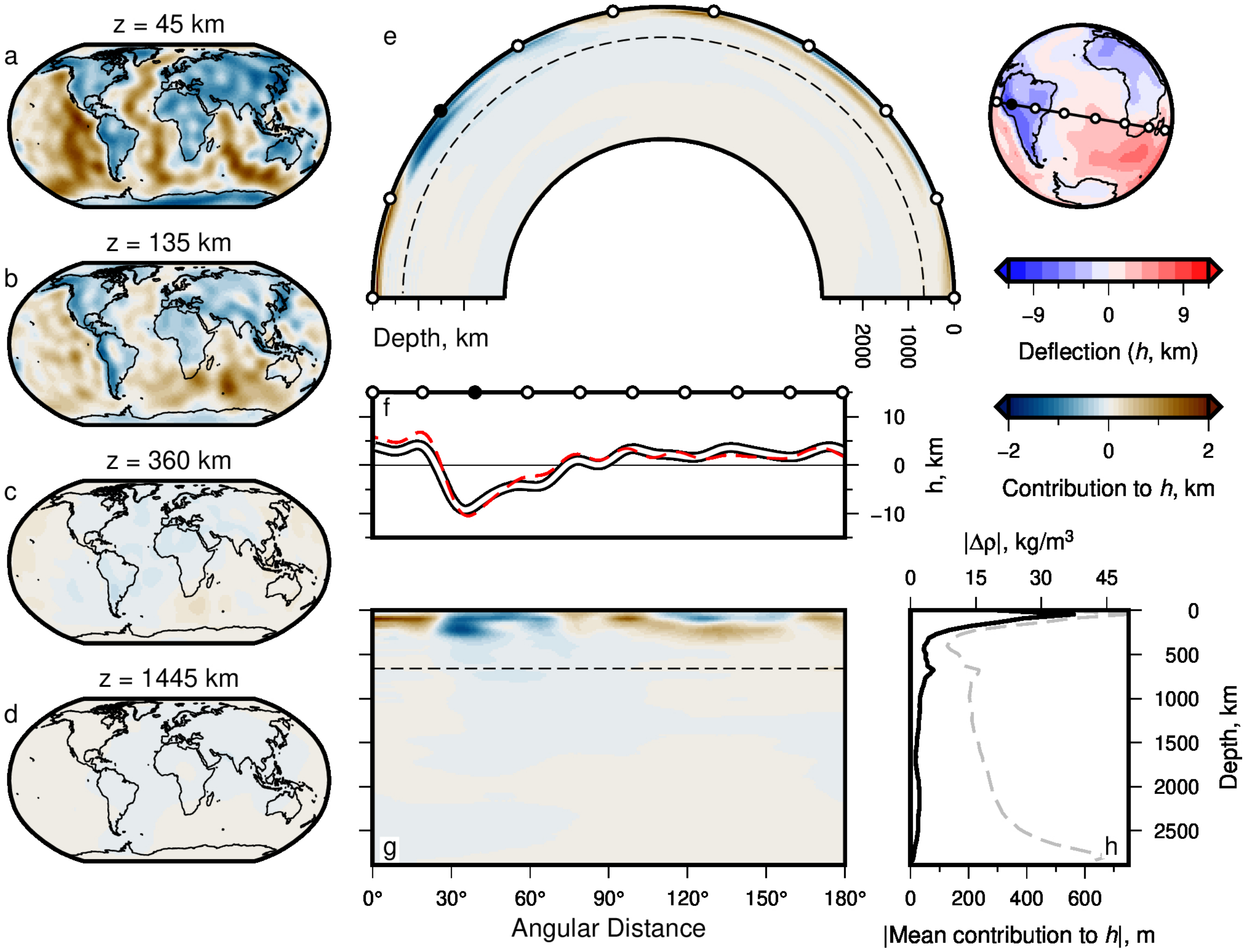

Figure S3. Surface deflections and effective densities up to maximum degree 20. As Figure S1, but for maximum spherical harmonic degree $l = 20$.

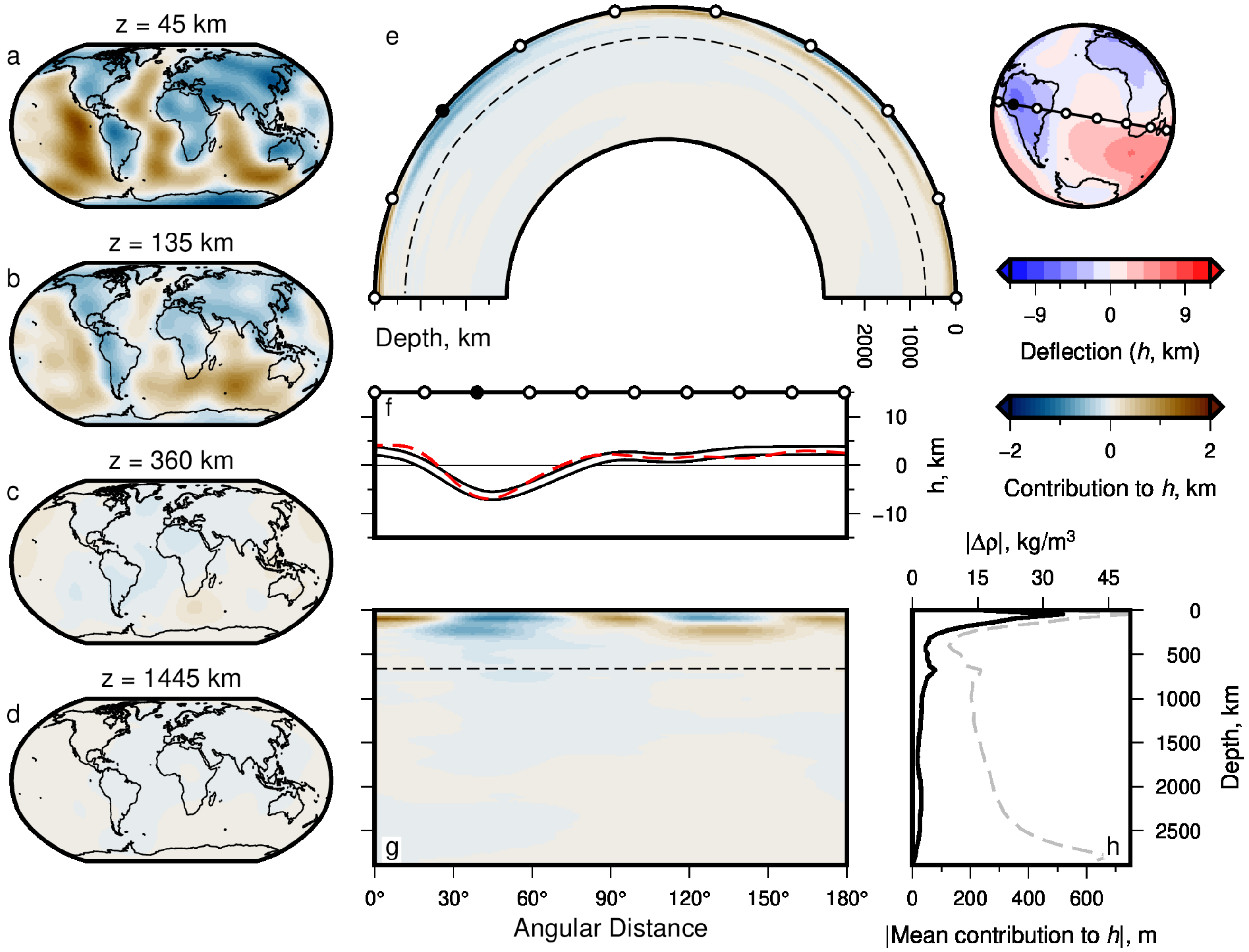

Figure S4. Surface deflections and effective densities up to maximum degree 10. As Figure S1, but for maximum spherical harmonic degree $l = 10$.

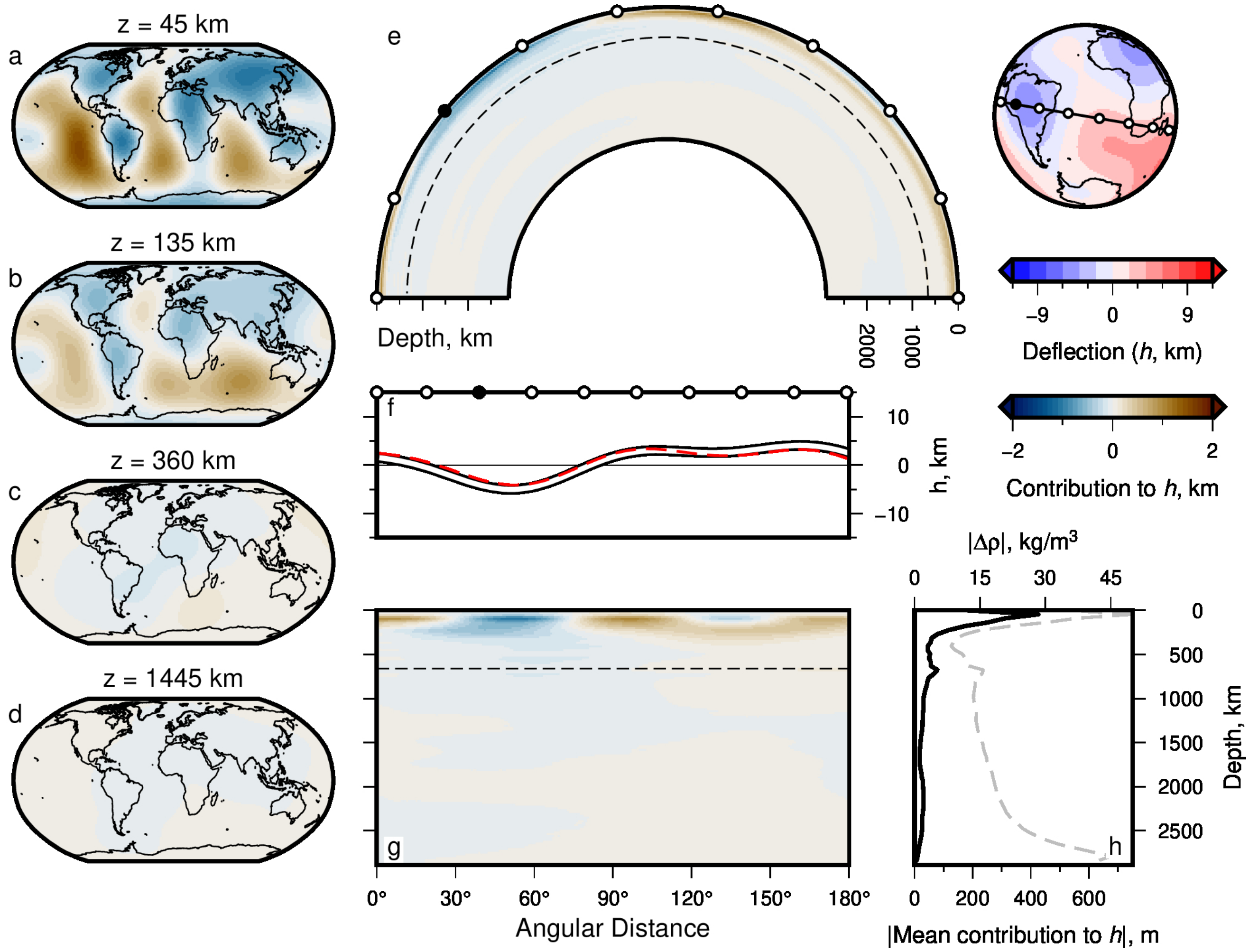

Figure S5. Surface deflections and effective densities up to maximum degree 5. As Figure S1, but for maximum spherical harmonic degree $l = 5$.